Università degli Studi di Padova

DIPARTIMENTO DI INGEGNERIA DELL'INFORMAZIONE

Corso di Laurea Magistrale in Ingegneria Elettronica

Impact of growth substrate on the reliability of InAs Quantum Dot Lasers for Silicon Photonics

Candidato:
Lorenzo Rovere
Matricola 1154503

Relatore:
Matteo Meneghini

Anno Accademico 2018-2019

8 Luglio 2019

Abstract

This thesis reports the results of the analysis of the reliability of InAs quantum dot (QD) lasers epitaxially grown on silicon and gallium arsenide. The analysis has been carried out in close cooperation with the manufacturer of the devices, the University of California, Santa Barbara (UCSB). The main objective of this work was to identify the physical degradation mechanisms that affect this new kind of semiconductor laser diodes, besides the investigation of the impact of extended defects dislocations in order to observe the different aging dynamics with different substrate material. For this purposes, the devices have been submitted to several accelerated degradation experiments. By means of electrical and optical measurements we were able to identify the degradation mechanisms and to study the role of extended defects, proving high dependency from the dislocation density. Moreover, the different epitaxial structure between the GaAs-substrate and the Si-substrate devices have highlighted different effects on the degradation dynamics of the lasers.

Table of contents

Abstract i

Introduction 1

1 Basic concepts of Laser Diode 5

1.1 Formation of bands in semiconductors . . . 5
1.2 Recombination processes . . . 6
1.3 Population inversion . . . 8
1.4 Photon generation and loss . . . 9
1.5 Carrier and optical confinement . . . 13
1.6 Electrical properties . . . 14
1.6.1 Current-Voltage characteristics . . . 14
1.6.2 Capacitance-Voltage characteristics . . . 16
1.7 Optical properties . . . 18
1.8 Temperature dependence . . . 19

2 Quantum dot structures 21

2.1 Classification of quantum structures . . . 21
2.1.1 Quantum Wells . . . 23
2.1.2 Quantum Wires . . . 24
2.1.3 Two-States lasing . . . 26
2.1.4 Ground State quenching . . . 26
2.2 Self assembled quantum dots . . . 28

3 Defects in semiconductors 31

3.0.1 Lattice deformations . . . 32
3.1 Point defects . . . 33
3.2 Dislocations . . . 33
3.3 Stacking faults . . . 34
3.4 Degradation modes . . . 34
3.4.1 Rapid degradation . . . 36
3.4.2 Gradual degradation . . . 38
3.4.3 Catastrophic degradation . . . 38

4 Experimental details **41**
4.1 Structure of the devices under test 41
4.2 Stress and characterization at room temperature 44
4.2.1 Source meter 47
4.2.2 Temperature controller 47
4.2.3 Optical spectrum analyzer 48
4.3 Characterization at cryogenic temperatures 49
4.4 Preliminary device characterizations 54

5 Results **63**
5.1 Silicon-substrate "Bar4" current step-stress 64
5.2 Current-step stress: GaAs-substrate and Si-substrate comparison 77
5.3 Constant-current stress comparison 91
5.4 Characterization at cryogenic temperatures 103
5.5 DLTS results 105

6 Conclusions **109**

References **113**

Introduction

Silicon photonics is the study and application of photonic systems which uses silicon as an optical medium. This is one of the most attractive discipline within the field of integrated optics: its origin can be traced back to the works of Soref, Schmidtchen and Petermann in 1980s and 1990s [1, 2, 3]. This technology has led to increased level of investments that are rapidly growing over the years, as shown in Fig. 1.

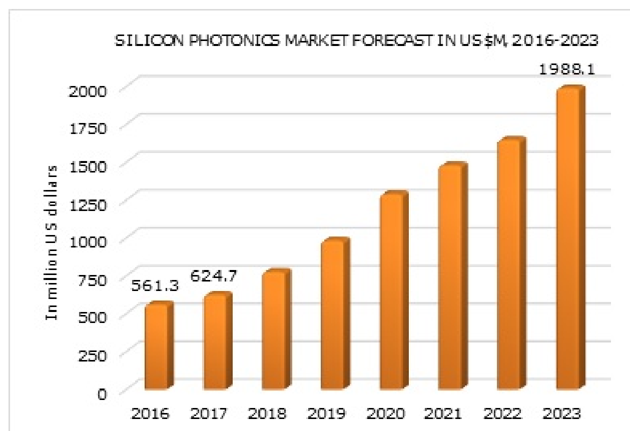

Figura 1: Silicon photonics market over the years (source: https://www.iebrain.com)

A point in favor of silicon photonics is its compatibility with the silicon integrated circuit (IC) manufacturing. Silicon wafers have low cost and high crystal quality, compared with other semiconductor materials. Silicon photonics devices can be made using existing semiconductor fabrication techniques and, because silicon is already used as the substrate for most integrated circuits, it is possible to create devices in which the optical and electronics compoents are integrated onto a single microchip. Another motivation for silicon photonics researches is the availability of high-quality silicon-on-insulator (SOI) wafers, that supports the scaling of photonics devices to the hundreds of nanometer level.
One of the most challenging aspect in silicon photonics is the creation of si-

licon optical amplifiers and lasers. Semiconductor lasers are on the verge of becoming the backbone of modern information technology: they play a major role in optical data communication networks [4, 5, 6] or as mode-locked devices [7], all no longer based on electrical transmission through copper lines. Some of the limitations of electrical circuits and interconnections include the limited transfer speed, i.e. the bit-rate, and the generated heat due to the resistive impedance of the connections. One of the most promising approaches to overcome these limitations is the use of optical links for data transfer both between and within microchips. High-throughput, high-speed and low-energy optical links such optical interconnect are especially demanded in data-centers, since data traffics are expansively increasing. The expected evolution of future low-power, high-performance server system is shown in Fig. 2: in such systems optical interconnects may improve the operation speed and simplify the interconnect system, and silicon photonics may prove particularly useful, once integrated on the standard silicon chip.

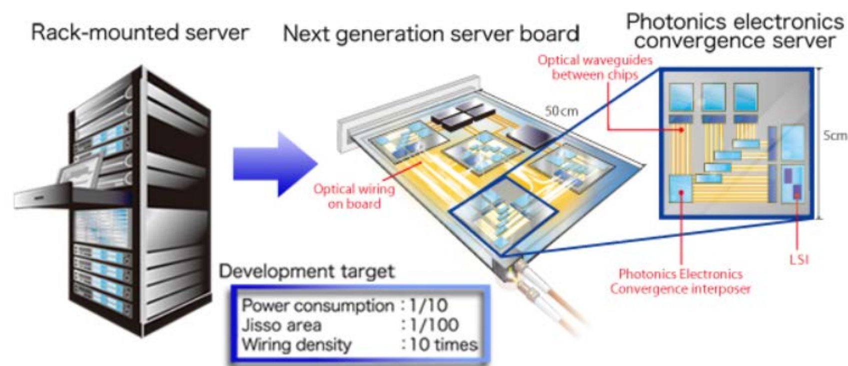

Figura 2: Expected evolution of future server system with photonics-electronics convergence systems (from http://www.petra-jp.org/pj_pecjs/en/index.html) [8]

In semiconductors, the recombination of carriers (electrons and holes) via radiative transitions leads to luminescence, i.e. emission of photons, while the energy emitted via non-radiative recombination transitions involves phonons, i.e lattice vibrations, and will be ultimately dissipated as heat. Radiative recombination with silicon-related material is difficult. As a matter of fact, silicon is an indirect bandgap material: this means that the minimum of the conduction band (CB) is not directly above the maximum of the valence band (VB) in the energy vs momentum (E-k) diagram (Fig. 3(b)). Thus, in order to have photon emission, the carrier transitions must involve the emission or absorption of phonons to satisfy energy and momentum conservation requirement, as shown in Fig. 3(c). Furthermore, indirect transitions

have a lower probability to occur than direct transitions. Consequently, the photon emission rate is not high in an indirect bandgap material, as well as not being energy-efficient. Hence, direct bandgap semiconductors, such as Gallium Arsenide (GaAs) and other III-V compound alloys, are the most attractive and developed materials in the optoelectronics field: in direct-gap semiconductors, the electron momentum does not change for transitions from the minimum of the conduction band to the maximum of the valence band (Fig. 3(a)).

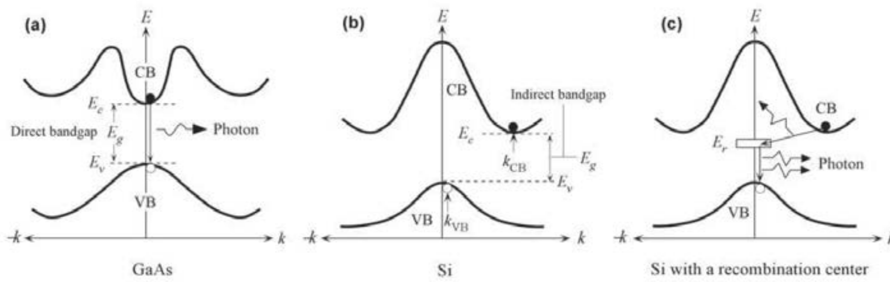

Figura 3: E-k diagram of (a) direct bandgap material: the electron recombines and generates a photon without any change in its momentum value, (b) and (c) indirect bandgap material: recombination of an electron and a hole involves the emission of a phonon, for the momentum conservation.

Lasers based on Quantum Dots (QD) possess a variety of advantages over other semiconductor systems and make them especially suited for these kind of applications [9]. Quantum dots represent zero-dimensional, particle-in-a-box-like quantum confined structures that can be formed through a self-assembly process. III-V compound quantum dots can be used for producing III-V laser diodes directly placed on silicon, with the advantages of lower threshold current density and less sensitivity to defects relative to conventional quantum wells.
A way to incorporate III-V materials with the silicon photonics platform could be the *hybrid* integration that refers to co-packaged III-V and Si devices on native substrates: this technique requires precise alignment of the III-V and Si chips that complicates packaging and limits scalability. A simpler approach is called *heterogeneous* integration, that provides for the bonding of III-V materials to a SOI substrate: in this case, the alignment procedure is transferred to secondary and less complicated semiconductor processing stages. For heterogeneous integration, III-V devices are grown on native substrate, then the device is bonded to Si and the III-V substrate removed. This clearly constitutes a cost that can be avoided through epitaxial growth on Si followed by wafer bonding. However, the challenges associated with mismatched epitaxy must be overcome: non-nitride III-V materials have lar-

ger lattice constants and higher coefficients of thermal expansion respect to silicon, which can result in high densities of crystalline defects. Nevertheless, the defect density can be reduced near native substrate level performances through careful optimization of growth conditions [10] and dislocation filter layers (DFLs), that has been proved it is able to remove up to 90% of threading dislocations [11].
Room temperature lasing near the telecommunications wavelength of 1.3 μm have been demonstrated with low threshold current densities for InAs/GaAs quantum-dot lasers grown on Si, Ge and Ge-on-Si substrates [12, 13, 14]. The 1.3 μm - 1.5 μm emission wavelengths constitute the usual transmission windows of the optical fiber due to the absorption characteristics of the glass material used in it. An additional, but not less important factor is the maximum data transmission rate that can be achieved, in the order of tens of Tbit/s [15].
The aim of this thesis work has been the study of the degradation processes that affect state-of-the-art QD lasers epitaxially grown on silicon and gallium arsenide substrates so as to highlight the differences that can arise in the devices through the same stress conditions.
For this purpose, the lasers have been characterized and submitted to current step-stress and constant bias stress experiments, at a temperature of 35°C, in order to extrapolate electrical and optical variation trends during time, thus hypothesizing the physical degradation processes in place. Deep Level Transient Spectroscopy (DLTS) measurements have been performed on a bonded sample to investigate the presence of deep active defects in the depletion region of the device.
The structure of this thesis is organized as follows:

- Chapter 1: working principles of laser diodes, electrical and optical properties.
- Chapter 2: quantum confinement concepts and quantum dot growth techniques
- Chapter 3: semiconductor defects and degradation processes
- Chapter 4: devices structure, experimental setups and preliminary characterization
- Chapter 5: experimental results and comparison of the two different substrate material composition
- Chapter 6: conclusions and future works

Chapter 1

Basic concepts of Laser Diode

In this chapter the principles of laser diodes are discussed. In particular, the formation of bands in semiconductor, the mechanisms that rules different types of recombination processes, electrical and optical characteristics. Further material and explanations can be found in [24, 25, 18].

1.1 Formation of bands in semiconductors

Electrons in an isolated atom can only have discrete energy levels, according to the Bohr model of an atom, that can be evaluated by solving Schrodinger's equation using the appropriate electronic potentials. However, when atoms are brought together as in crystalline solids, these degenerate energy levels will split into many separated levels due to the atomic interaction. Because the levels are so closely separated, they may be treated as a continuous band of allowed energy states (Fig. 1.1). The two highest energy bands are the

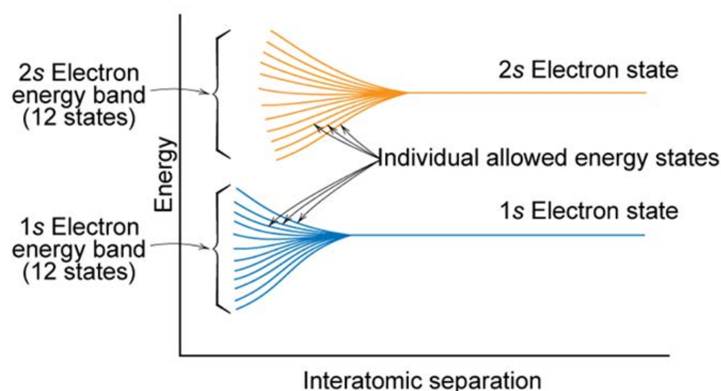

Figure 1.1: Energy bands formation in crystalline solids.

valence band, E_V, and the *conduction band*, E_C. These bands are separated

by a region which designates energy states not allowed (to electrons). This region is called the forbidden gap, or *bandgap* E_g. This is the energy difference between the maximum valence band energy and the minimum conduction band energy.
Unlike insulators, in which the valence electrons form strong bonds between neighboring atoms, bonds in a semiconductor are moderately strong; therefore energy (at least E_g) can break these bonds. Thus, an electron can be promoted to the conduction band while leaving a positive net chartge, a *hole*, in the valence band. This process is called generation of and electron-hole pair [19]. The opposite process, the recombination of and electron-hole pair, occurs when electrons are transferred from conduction to valence band. This implies the transfer of the electron excess energy to other particles (electrons, phonons, photons).

1.2 Recombination processes

Recombination processes can be radiative, with the emission of a photon, or nonradiative, without the photon emission. The emission process of a photon can be:

- spontaneous, when a photon is emitted during the electron transition from the upper energy state (E_2) to the lower energy state (E_1).
- stimulated, when an incident photon of matching energy $\hbar\omega = E_2 - E_1$ perturbs an electron in the upper state and stimulates the decay into the lower state. A second photon is then emitted with the same direction, phase and frequency of the incoming photon, resulting in an amplification of the incident radiation. This is the mechanism that is necessary for lasers to operate.

For sake of clarity, stimulated absorption is another processes that involves a striking photon. In this case the photon promotes an electron from a lower energy state to a higher energy state. The energy of the incoming photon must be at least E_2-E_1. Figure 1.2 shows the processes described above. Regarding semiconductors, there are two main non-radiative transitions that can involve carriers:

- Shockley-Read-Hall (SRH) recombination involves semiconductor defects mostly ascribed to the crystalline impurities, surface defects and interfaces, whose interaction with the crystal lattice permits the formation of allowed energy levels inside the forbidden energy gap of the material (Fig. 1.3). Such levels act as recombination centers: carriers do not contribute to the photon emission and, conversely, release their energy by phonons (lattice vibration), that increase the heat inside the material.

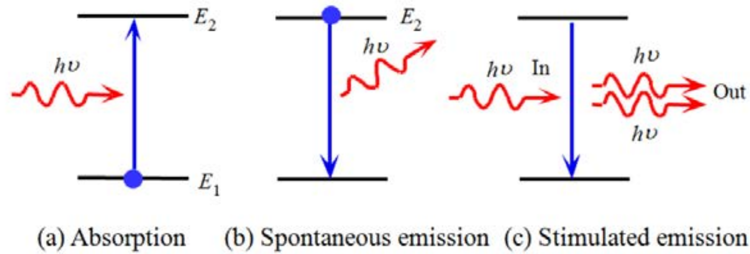

Figure 1.2: Absorption and emission processes.

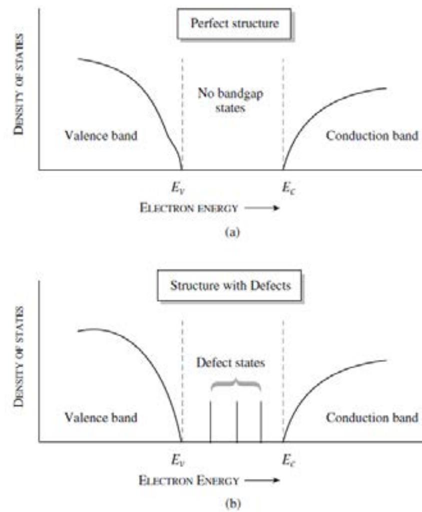

Figure 1.3: Schematic of density of states (a) in a perfectly periodic solid and (b) in a material with defects. The presence of bangap states reduces the radiative recombination rate in the material.

- Auger recombination, that involves the interaction of three carriers. Two electrons collide which causes one to decay and recombine with a hole in the valence band. Meanwhile, the energy released by the recombination will cause the other electron to be promoted to a higher state in the conduction band. It eventually transfers its energy to the lattice, contributing to the general heat up of the material. The same interaction can happen with two holes and one electron.

Figure 1.4 sketches the processes described above.

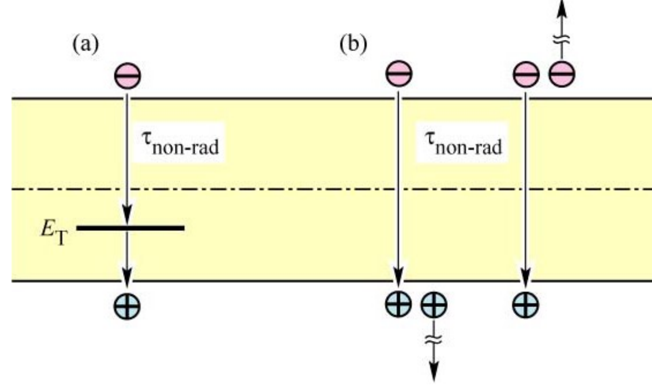

Figure 1.4: Non-radiative recombination: (a) SRH, (b) Auger.

1.3 Population inversion

As mentioned in the previous section, a net amplification of incoming light can be achieved by stimulated emission. This only can happen with a high concentration of photons and if more electrons are available for stimulated emission than for absorption (when an electron is lifted into the upper state, while the incident photon is consumed). This means that the population of the upper energy state E_2 is higher than of the lower energy state E_1. This phenomenon is called *population inversion* and is never reached in thermal equilibrium. The system can reach population inversion through a process called "pumping": this can be driven optically, electrically or even chemically [19].
The analytic relations useful to explain the population inversion process has been studied by Einstein. In a system with N_1 and N_2 number of atoms per unit volume at E_1 and E_2, respectively, the rate of stimulated emission R_{21}^{stim}, stimulated absorption R_{12}^{stim} and spontaneous emission R_{21}^{spon} can be defined using the Einstein's coefficients:

$$R_{21}^{stim} = B_{21}\rho(h\nu)N_2 \tag{1.1}$$

$$R_{12}^{stim} = B_{12}\rho(h\nu)N_1 \tag{1.2}$$

$$R_{21}^{spon} = A_{21}N_2 \tag{1.3}$$

with $\rho(h\nu)$ photon energy density and B_{21}, B_{12} and A_{21} the Einstein's coefficients for stimulated emission, stimulated absorption and spontaneous emission, respectively. It can be noted how Equations (1) and (2) depend on the number of photons with sufficient energy to overcome the energy gap ($E_{ph} = h\nu > E_2 - E_1$).
In thermal equilibrium:

- radiation from the atoms must give rise to an equilibrium photon energy density ρ_ν defined Planck's black body radiation distribution law:
$$\rho_\nu = \frac{8\pi h\nu^3}{c^3}\frac{1}{e^{h\nu/k_BT}-1} \tag{1.4}$$
- the number of upward transitions must be equal to the number of downward transitions
$$R_{12}^{stim} = R_{21}^{stim} + R_{21}^{spon} \iff B_{12}\rho(h\nu)N_1 = B_{21}\rho(h\nu)N_2 + A_{21}N_2$$
$$\Rightarrow \rho_\nu = \frac{A_{21}N_2}{B_{12}N_1 - B_{21}N_2} = \frac{A_{21}/B_{21}}{(B_{12}/B_{21})(N_1/N_2)-1} \tag{1.5}$$
- the population of energy levels follows the Boltzmann statistics:
$$\frac{N_2}{N_1} = exp\left(\frac{-(E_2-E_1)}{k_BT}\right) \tag{1.6}$$

from the previous equations it follows that:

$$B_{12} = B_{21} \tag{1.7}$$
$$\frac{A_{21}}{B_{21}} = \frac{8\pi h\nu^3}{c^3} \tag{1.8}$$

The ratio between stimulated to spontaneous emission is

$$\frac{R_{21}^{stim}}{R_{21}^{spon}} = \frac{B_{21}\rho(h\nu)}{A_{21}} = \frac{c^3}{8\pi h\nu^3}\rho(h\nu) \tag{1.9}$$

and the ratio of stimulated emission to absorption is

$$\frac{R_{21}^{stim}}{R_{12}^{stim}} = \frac{B_{21}\rho(h\nu)N_2}{B_{12}\rho(h\nu)N_1} = \frac{N_2}{N_1} \tag{1.10}$$

Equations (1.9) and (1.10) confirm what explained at the beginning of this section: in order to increase the probability of stimulated over spontaneous emission a high photon concentration is needed, while to have more stimulated emission than absorption, the population inversion is needed ($N_2 > N_1$).

1.4 Photon generation and loss

The typical structure used to enhance the light in a certain direction using a resonant cavity structure is called a Fabry-Perot cavity and is illustrated in Fig. 1.5. It is made of a linear optical cavity with a high-reflectivity mirror

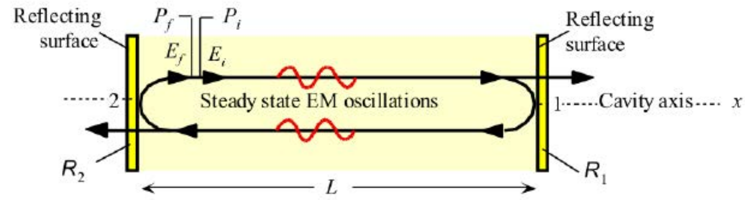

Figure 1.5: Schematic view of a Fabry-Perot resonator.

on one side and a low-reflectivity mirror on the other, so that photons of the cavity modes are reflected and can pass through the gain medium multiple times before being absorbed or escaping the cavity. The gain medium amplifies light through the process of stimulated emission, as already explained. The gain medium does not amplifies all optical frequency equally, but possesses a gain profile. For lasers there are usually many cavity modes, given by

$$nL = \frac{m\lambda}{2} \tag{1.11}$$

where the mode number m is an integer and refers to the cavity mode number and n is the effective index of refraction, λ is the selected wavelength and L the cavity length. The gain medium spectral response, in combination with the cavity modes, will define the amplified cavity mode that will be coupled out the resonator.(Fig. 1.6). A photon can be lost through its interaction with an atom's bound electrons. In this way the photon is absorbed and an EHP is generated. The electron will eventually recombine and return to the lower state, but this process will not necessary occur radiatively or by stimulated emission.
Free carrier absorption is another kind of optical absorption. It occurs when an electron is the conduction band absorbs a photon and moves to a higher state. The electron then moves to higher states and can cause lattice heating. The photon can also be absorbed by the lattice structure and results in lattice vibrations and consequence heating. Such an effect can increase the chance of the same type of absorption, which will cause further heating.
There is also the probability of absorption by impurities and defects, as well as by the non-ideality of the mirrors, resulting in absorption, diffusion and diffraction of radiation.
To achieve lasing, optical gain must at least equal the losses. Increasing the current injection level, there will be eventually a point at which the gain will overcome the losses. Referring to Fig 1.5, the cavity of length L has two reflecting mirrors with reflection coefficients R_1 and R_2. Considering a point and assuming that the starting radiation power of that point is P_{i}, then the final power P_{f}, that is the radiation after being reflected off of surface 1 and 2 respectively, will become $P_f = R_2 R_1 P_{\mathrm{i}}$. If g is called the optical

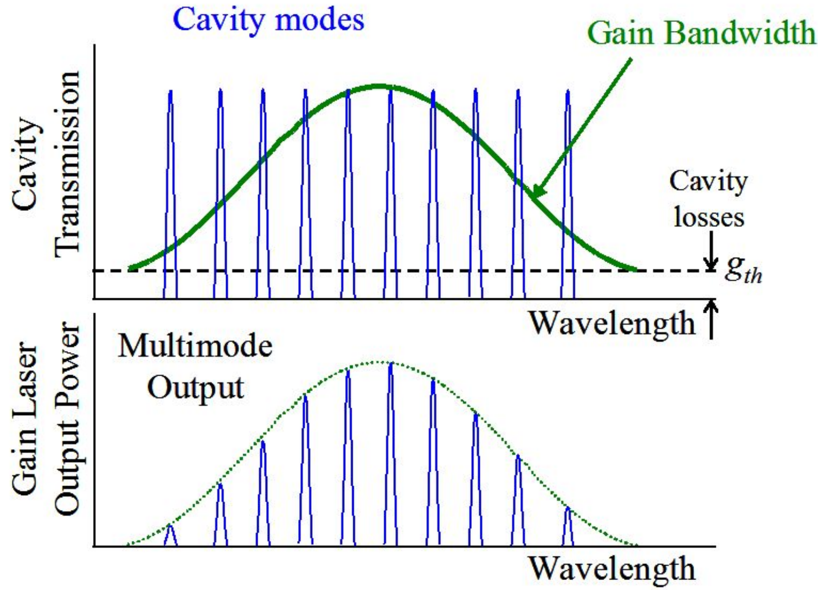

Figure 1.6: Modes amplification in the cavity due to the gain medium spectral response.

gain coefficient and is defined as the variation of the radiation power per unit length, it will be increased according to $e^{g \cdot x}$. As radiation travels inside the cavity it also stimulates more coherent emission. On the other hand some emission will be absorbed: the losses can be represented for the same distance as $e^{-\gamma \cdot x}$, where γ represents losses inside the laser. The optical round-trip gain can be defines as:

$$G = \frac{P_f}{P_i} = R_1 R_2 e^{2(g-\gamma)L} \tag{1.12}$$

From here one can calculate the threshold optical gain, g_{th}, that is the value of the optical gain for which the gain balances the losses (G=1):

$$g_{th} = \gamma + \frac{1}{2L} ln \left(\frac{1}{R_1 R_2} \right) \tag{1.13}$$

For electrically-pumped laser diodes, this value corresponds to a current injection value, called threshold current I_{th} (or referring to threshold current density J_{th}): below threshold spontaneous recombination dominates, while above threshold stimulated emission begins to take over, as shown in Fig. 1.7. However, increasing the pump rate above threshold will not increase the carrier density or the gain, that will clamp at their threshold values. What happens when the current is increased to a value above threshold is that the carrier density and gain initially increase to values above their

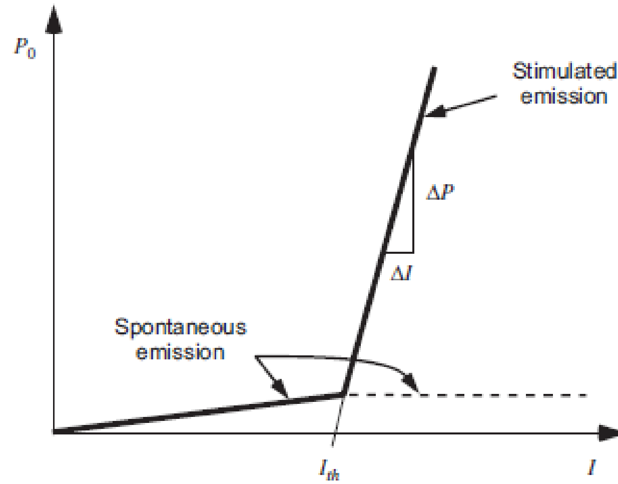

Figure 1.7: Optical power vs. injected current: below threshold the light emission is due to spontaneous emission, above threshold stimulated emission dominates

threshold levels and the photon density grows. Afterwards the stimulated recombination rate increases rapidly, reducing the carrier density and gain to a new steady-state value.
This relationship can be explained considering the definition of the optical gain coefficient defined above. Optical power is proportional to the coherent photon concentration N_{ph} and to its energy $h\nu$. The optical gain coefficient can be expressed as

$$g = \frac{dP}{Pdx} = \frac{dN_{ph}}{N_{ph}dx} = \frac{dN_{ph}}{N_{ph}}\frac{n}{cdt}, \tag{1.14}$$

since photons travel with velocity c/n, with n refraction index of the active medium, so they cover a distance $dx = (c/n)dt$.
The rate of coherent photons can be seen as the difference between stimulated emission and absorption:

$$\frac{dN_{ph}}{dt} = (N_2 - N_1)B_{21}\rho(h\nu) \tag{1.15}$$

Therefore, the optical gain of the medium respect to the frequency $g(h\nu)$ can be calculated considering that $\rho(h\nu)$ is the density of energy per unit frequency. For photons with energy $h\nu_0$:

$$\rho(h\nu_0) = \frac{N_{ph}h\nu_0}{\Delta\nu} \tag{1.16}$$

where $\Delta\nu$ is the spectral broadening of the emission and absorption mechanisms caused by the Doppler effect, collision with phonons or natural damping

of the transition lifetime.
Finally, an expression for the optical gain of the medium at the center frequency ν_0 can be obtained from Eqs. 1.14 and 1.16:

$$g(\nu_0) = (N_2 - N_1)\frac{B_{21}nh\nu_0}{c\Delta\nu} \tag{1.17}$$

Substituting Eq. 1.17 into Eq. 1.13, the threshold population inversion value is calculated

$$(N_2 - N_1)_{th} = g_{th}\frac{c\Delta\nu}{B_{21}nh\nu_0} \tag{1.18}$$

This relationship shows that, when population inversion reaches threshold, its value do not increase if the pumping increases. What increases, however, is the output power (Fig. 1.8).

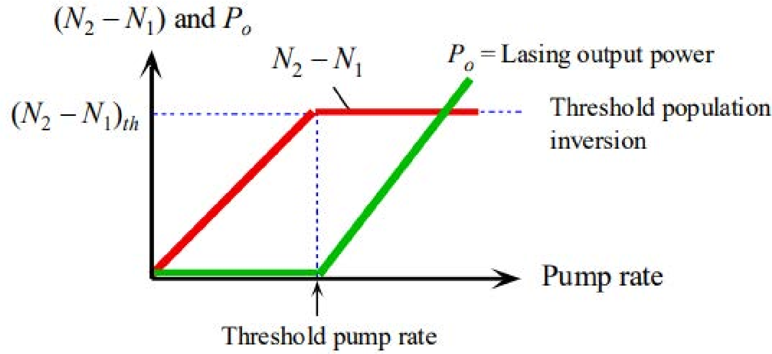

Figure 1.8: Injected carrier concentration and optical power vs. current: carrier concentration clamps at threshold.

1.5 Carrier and optical confinement

A semiconductor laser can be seen as a pn junction. The simplest structure has the same direct bandgap throughout and is called *homojunction*. However, this arrangement is characterized by poor carrier confinement and almost no optical confinement. In a homojuction the population inversion takes place on a distance proportional to the carrier diffusion length. Since confinement is poor, the threshold current density is usually very high and such devices are inefficient for practical values. High carrier confinement can be achieved using a double heterostructure (DH), composed of two junctions between different semiconductor materials with different bandgaps. In DH junctions carriers are confined into the material with the lower E_g, thus the region where carriers recombine does not depend on carrier diffusion length. Therefore, the "active" recombination region is much more reduced, which

increases the carrier concentration for population inversion and the probability of radiative recombination. At the same time, placing the material with higher refractive index (and lower bandgap) between two material with lower index will create an optical dielectric waveguide necessary for a higher optical confinement. Further details are given in Chapter 2. The differences between homojunction and heterojunction are summarized in Fig. 1.9.

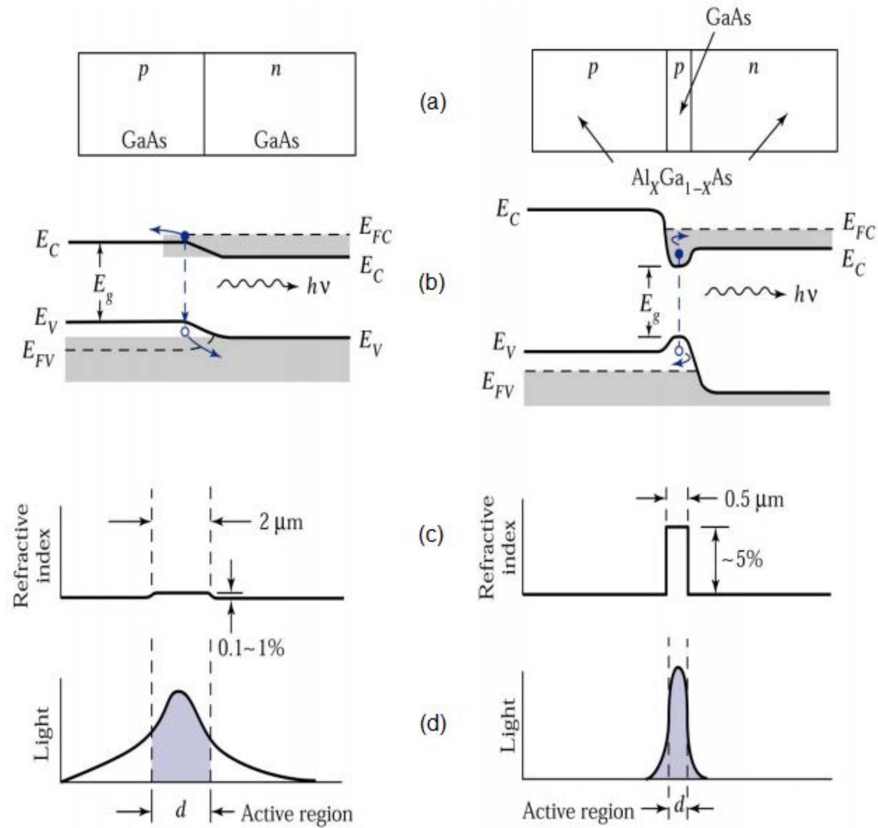

Figure 1.9: Homojunction (left) and heterojunction (right): (a) material (b) band diagram (c) refractive index (d) optical confinement.

1.6 Electrical properties

1.6.1 Current-Voltage characteristics

From the electrical point of view, a laser can be considered as a pn junction [20, 21] by making the following (simplifying) assumptions:

- abrupt junction: the dopant concentration (N_D and N_A for donors and acceptors respectively) is constant in the doped region and zero elsewhere, without gradual transitions between the different regions

- implanted dopants are entirely ionized and contribute to the free electrons and holes ($n = N_D$, $p = N_A$)

Therefore, carriers diffuse to the opposite zone, because of the difference in the concentration gradient, where can recombine. The result is the creation of a region depleted of free carriers, called Space Charge Region (SCR). An external bias-voltage applied drops almost entirely across the SCR, modulating the potential barrier through which electrons and holes can move (Fig. 1.10). The analytic relation that describe this phenomenon has been studied by Shockley and shows how current saturates in reverse-bias regime and exponentially increases with forward-bias voltage. The characteristic does not

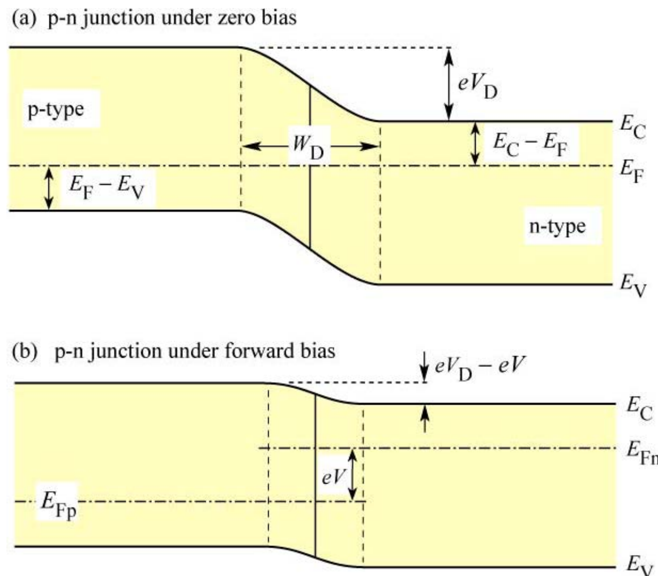

Figure 1.10: pn junction under (a) zero bias and (b) forward bias. The potential barrier is modulated by the applied voltage V_D.

follow the ideal trend because of parasitic resistances:

- the series resistance accounts for the metal contacts and the undoped region of the junction. Its effect arises especially at high voltage values and decreases the diode current.

- the parallel resistance originates from damaged regions or surfaces leakage that generate conduction paths parallel to the diode. The effect of the shunt resistance is to contribute to carrier flow for reverse and low-forward applied voltage

Figure 1.11 summarizes the resistances effect on the ideal I-V curve. The

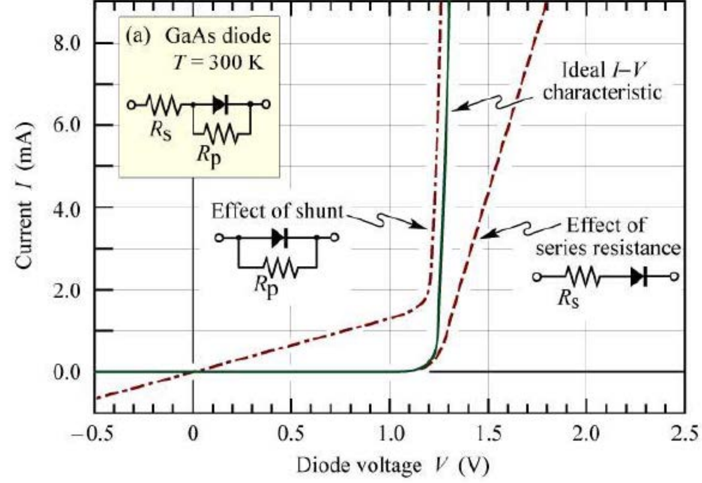

Figure 1.11: Effect of the parasitic resistances on the ideal I-V characteristic.

electrical characteristic of the laser diode follows the classic Shockley equation

$$I = I_s \left(exp \left(\frac{qV}{n_{ideal} k_B T} \right) - 1 \right) \quad (1.19)$$

where I_s is the reverse-bias saturation current, T is the junction temperature and n_{ideal} is the ideality factor, that can be expressed from the evaluation of the first differential conductance σ_D

$$\sigma_D = \frac{\partial I}{\partial V} = \frac{I_s q}{n_{ideal} k_B T} exp \left(\frac{qV}{n_{ideal} k_B T} \right). \quad (1.20)$$

Finally, the ideality factor can be expressed as

$$n_{ideal} = \frac{q}{k_b T} \left(\frac{\partial ln(\sigma_D)}{\partial V} \right)^{-1} \quad (1.21)$$

An ideal pn homojunction has an ideality factor of 1, that can increase to 2 due to generation/recombination currents within the space-charge region, while that of a DH junction is typically higher (2-3). [21].

1.6.2 Capacitance-Voltage characteristics

The capacitance-voltage characteristic of the devices provides important informations of the devices such as the distribution of charge in proximity of the junction and the extension of the SCR.
The charge (per unit area) in the SCR is only due to fixed donors and acceptors:

$$Q = qN_D x_n = qN_A n_p \quad (1.22)$$

The second equality is true according to the principle of charge neutrality. From here one can evaluate the capacity as

$$C = \frac{dQ}{dV} = qN_D\frac{dx_n}{dV} = qN_A\frac{dx_p}{dV} \tag{1.23}$$

The charge generates an electric field and a built-in potential drop, that acts as a barrier for the diffusion of the carriers:

$$\phi_i = \frac{k_BT}{q}ln\left(\frac{N_DN_A}{n_i^2}\right) \tag{1.24}$$

with N_D and N_A are the donor and acceptor concentrations, respectively, n_i the intrinsic carrier concentration of the semiconductor.
The width of the SCR can be expressed as the sum of the amplitude of the depleted region at the n and p sides:

$$x_d = x_n + x_p = \sqrt{\frac{2\epsilon}{q}(\phi_i - V)\left(\frac{1}{N_D} + \frac{1}{N_A}\right)} \tag{1.25}$$

with ϵ the dielectric permettivity of the semiconductor and V the voltage applied to the junction.
We can finally calculate the expression for the junction capacitance from Equations 1.23 and 1.25:

$$C(V) = \sqrt{\frac{q\epsilon}{2(\phi_i - V)\left(\frac{1}{N_D} + \frac{1}{N_A}\right)}} = \frac{\epsilon}{x_d} \tag{1.26}$$

From this result, the apparent charge profile can be expressed, hypothesizing the case in which one region in much more doped than the other one. For example, if the p-side is more heavily doped than the n-side ($N_A \gg N_D$) then $x_p \ll x_n$ and the SCR tends to extend entirely on the n-side. The Eq. 1.26, including the area of the junction A, becomes:

$$C(V) = A \cdot \sqrt{\frac{q\epsilon N_A}{2(\phi_i - V)}} \tag{1.27}$$

The carrier concentration is simply

$$N(V) = \frac{-2}{q\epsilon A^2 \frac{d}{dV}\left(\frac{1}{C^2}\right)} \tag{1.28}$$

thus, knowing that $C(V) = \epsilon/x(V)$, the apparent charge concentration as function of the apparent depth is:

$$N(x) = \frac{-2\epsilon}{qA^2 \frac{d}{dV}(x^2)} \tag{1.29}$$

As the name suggests, this is not the real doping profile since the hypothesis $N_A \gg N_D$ is not always verified and the SCR can expand in the p-side of the junction.

1.7 Optical properties

As previously stated, lasing condition is reached when the optical gain of the medium can overcome the cavity losses, which implies that the diode current has to exceed a certain threshold value I_{th}. Below this value, the light from the device is incoherent and mainly originated from spontaneous emission. Above threshold the light is mainly composed of coherent photons and the device is lasing. Figure 1.12 shows the output light intensity as a function of diode current. The wavelength of emission depends on the

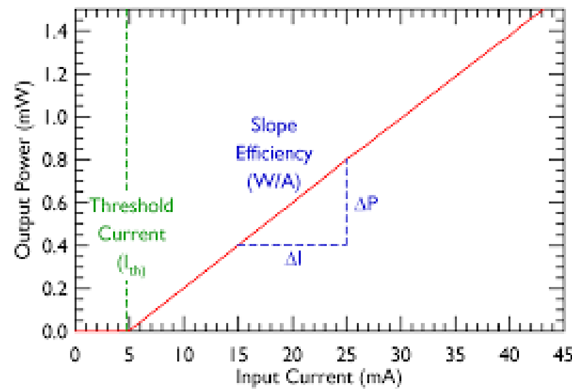

Figure 1.12: Laser output power vs. current with some spectra emission.

bandagap energy, the dopant concentration, the junction temperature and the cavity. The spectral width of the laser emission depends on the number of longitudinal modes excited. Above threshold, as the current increases, one of the intense modes becomes prominent at the expense of less intense modes. The prominent mode ends up using most of the injected electrons; there are insufficient electrons left for other modes to satisfy the threshold gain condition at those frequencies. The slope efficiency, in Fig. 1.12, is a very significant parameter for laser diodes. It can be expressed as $SE = dP/dI$ for $\mathrm{I} > \mathrm{I_{th}}$. The higher the slope efficiency is the higher the power conversion (from electrical power to optical power) efficiency is. Real devices tend to show a nonlinear optical power versus current characteristics above threshold and can have some slope variations called kinks. In general, multimode operation of laser is the most common mechanism limiting the effective power for a single spatial mode radiation. A P-I kink is usually linked to a change in the optical mode parallel to the active layer in the form of mode movement, mode transition, or excitation of higher order modes. Also the turn-on of current leakage paths at higher currents, which is usually due to ohmic losses, may lead to a rollover of the P-I. Some examples are sketched in Fig. 1.13.

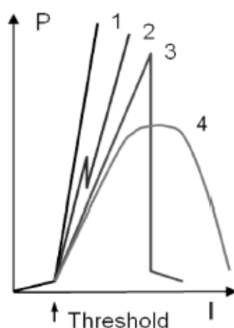

Figure 1.13: Limitations of laser diode optical output power versus current: (1) ideal output, (2) kink, (3) catastrophic optical damage (see Chapter 3) and (4) thermal rollover.

1.8 Temperature dependence

The temperature can heavily impact on the laser diode output characteristics. Fig. 1.14 shows the changes in the optical power vs. current with temperature. The threshold of a laser typically increases with increasing temperature and empirically follows an exponential law:

$$I_{th} = I_0 e^{T/T_0} \tag{1.30}$$

with I_0 a current constant and T_0 the overall characteristic temperature, that summarizes the temperature-dependent loss and the carrier redistribution due to the change of the Fermi distribution[1] with temperature. With increasing temperature, populated states below the quasi-Fermi level become unpopulated and nonlasing states become populated. Therefore, the gain decreases with increasing temperature. This redistribution must be compensated by an increase of the pumping rate. As previously mentioned, the emission wavelength and, thus, the emission spectrum, changes with temperature. Considering a single-mode laser diode, the peak emission wavelength exhibits jumps (*mode hops*) at certain temperatures as shown in Fig.1.15. At a different operating temperature another mode fulfills the laser oscillation condition. Between mode hops the emission wavelength slightly increases with temperature due to modifications with temperature in the refractive index of the cavity and because of the decrease in the energy gap of the material with temperature. Peltier-based temperature-controllers can be integrated in the package of the lasers to improve wavelength/power stability.

[1] In thermodynamic equilibrium, the distribution function for carriers is given by the Fermi-Dirac distribution $f(E) = \frac{1}{exp\left(\frac{E-E_F}{k_B T}\right)+1}$ with E_F the Fermi level that can be considered to be a hypothetical energy level of an electron or hole. If the Fermi level is not constant throughout the structure, for instance because of doping, then the quasi-Fermi level describes the local carrier density

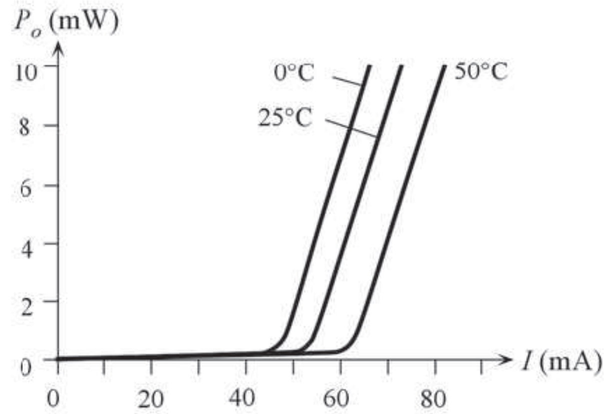

Figure 1.14: Output optical power vs. diode current at three different temperatures. The threshold current shifts to higher temperatures.

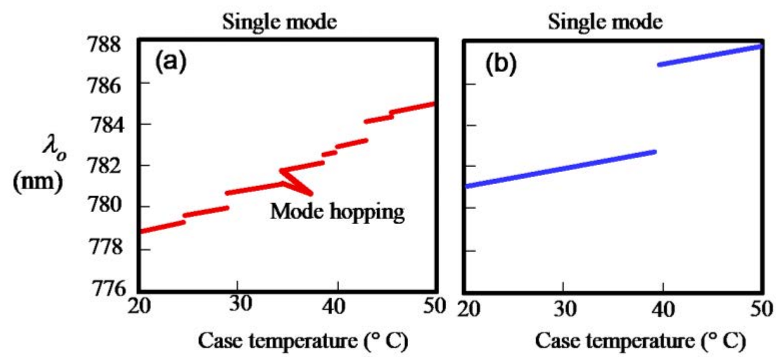

Figure 1.15: Peak wavelength λ_0 versus case temperature characteristics. (a) Mode hops in the output spectrum of a single-mode LD. (b) Restricted mode hops.

Chapter 2

Quantum dot structures

To truly achieve native substrate performance and reliability, quantum dot active regions must be adopted over quantum wells. In this chapter, the classification of quantum structures is followed by some characteristics of quantum dots, such as two-state lasing and ground state (GS) quenching. Finally, the self assembled QD growth technique is described. Quantum dots fundamentals are mainly taken from [22] and [23].

2.1 Classification of quantum structures

Reducing the size of materials to the nanometer scale is related to the confinement in the movement of electrons due to the *quantum confinement effect*. The consequence is the discretization of electron energy levels depending on the confinement size of the material [24, 25]. When the particle size approach the Bohr radius [26]:

$$a_0^* = \frac{\epsilon \hbar^2}{m^* q^2} \tag{2.1}$$

with ϵ the dielectric constant of the material and $m*$ the effective mass of the particle, the quantum confinement effect leads to a collapse of the continuous energy bands of a bulk material into discrete, atomic-like energy levels.
Quantum structures are mainly classified according to the number of degrees of freedom experienced by electrons and holes inside the material. Accordingly, quantum nanostructures can be divided into the following classes (schematic diagram in Fig. 2.1):

- Quantum Well (QW): film structures usually deposited on rigid substrates, in the order of a few nanometers. They are defined as two-dimensional (2D) structures because the particle is free to move in two directions, while quantized in the other. They can be experimentally realized by ephitaxial growth of semiconducting materials.

- Quantum Wire (QWr): one-dimensional (1D) structures in which electrons are free to move in one direction and quantization occurs in the remaining two. They appear like wires with diameters in the nanometer range and lengths of several micrometers.
- Quantum Dots (QDs): zero-dimensional (0D) structures in which the electron quantization occurs in all three directions.

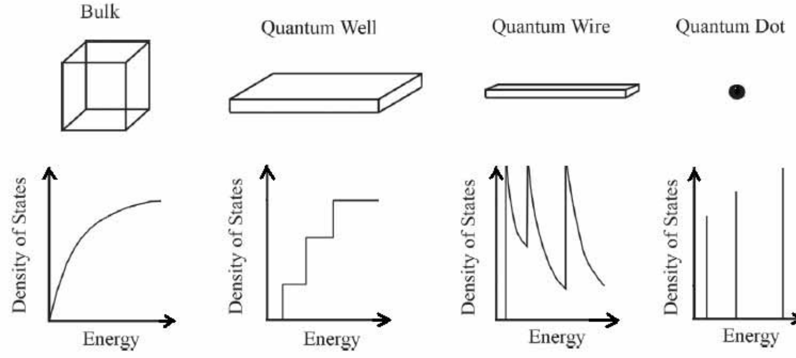

Figure 2.1: Schematic representation of low-dimensional semiconductor structures with the corresponding density of states.

The quantum confinement effect, depending on the size of the nanostructure, can be estimated via the effective-mass approximation model, which can predict the confined energy levels of nanostructures by solving Schrodinger equation assuming the barriers have an infinite confining potential. The effective mass solutions of the Schrodinger equation for electrons confined in a QW, QWr and QDs are, respectively:

$$QW : E_n(x,y) = \frac{\pi^2\hbar^2 n^2}{2m^* L_z^2} + \frac{\hbar^2}{2m^*}(k_x^2 + k_y^2), \psi = \phi(z)e^{ik_x x + ik_y y} \tag{2.2}$$

$$QWr : E_n(x) = \frac{\pi^2\hbar^2}{2m^*}\left(\frac{n^2}{L_z^2} + \frac{m^2}{L_y^2}\right) + \frac{\hbar^2 k_x^2}{2m^*}, \psi = \phi(z)\phi(y)e^{ik_x x} \tag{2.3}$$

$$QDs : E_n = \frac{\pi^2\hbar^2}{2m^*}\left(\frac{n^2}{L_z^2} + \frac{m^2}{L_y^2} + \frac{l^2}{L_x^2}\right), \psi = \phi(z)\phi(y)\phi(z) \tag{2.4}$$

where n, m, l are integer quantum confinement numbers, k_i is the wave vectors of the electron along the i- direction, L_x, L_y, L_z are the confining dimensions, ψ is the eigenfunction that can be expressed as the product of wavefunctions describing the motion in the three direction.

2.1.1 Quantum Wells

Quantum wells are heterostructures in which a thin layer of one semiconductor is sandwiched between two layers of a different semiconductor material, thereby forming a heterojunction. The central layer has the lower bandgap, while the two layers sandwiching the center create the potential barriers as shown in Fig. 2.2. Thus, materials are chosen so that electrons available

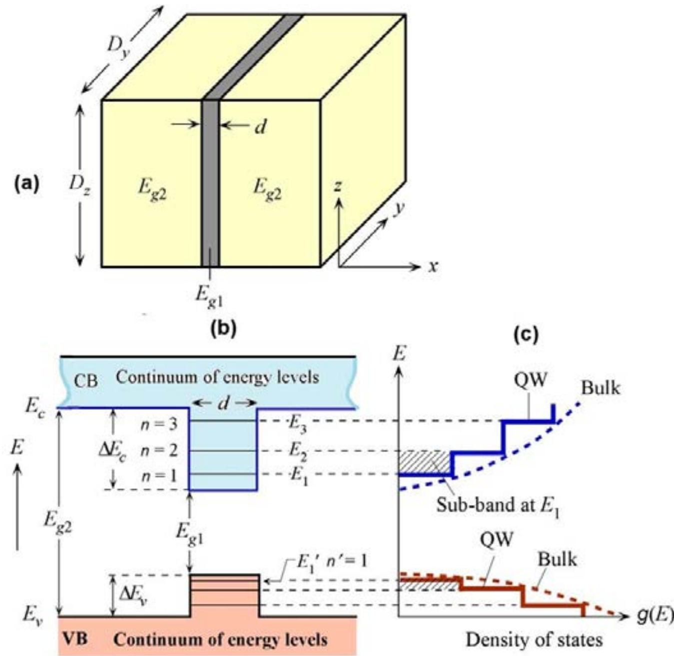

Figure 2.2: (a) a single quantum well, (b) the electron and hole energy levels associated with (c) the density of states.

for conduction in the middle layer have lower energy than those in the outer layers, creating an energy well that confines the electrons in the middle layer. The thickness of the middle layers is comparable with the wavelength of the electrons confined in it, thereby modifying the electron behavior, since they are now confined whithin a plane than in a bulk sample.
As previously said, the energies of electrons in the well exhibit quantized thresholds. Respect to a bulk semiconductor, where the density of allowed states, i.e. the number of electrons that can exist within a range of energies, is proportional to the square root of energy [27], the density of states in a quantum well layer turns out to be constant with energy: a step-like function. There are not discrete energy states for carriers, but sub-bands that start at the energies calculated for the confined states in Eq. (2.2). Thus, radiative transitions occur much more readily in the quantum well for the

same current as in the bulk device, where the carriers are spread more deeply into the conduction band. The differences can be observed in Fig. 2.2(c).

2.1.2 Quantum Wires

Quantum wires are extremely narrow structures where electron transport is possible only in a few transverse modes. Quantum wires can be fabricated starting from a standard quantum well layer patterned with photolithography for instance, and etched to leave a free standing strip of quantum well material, as shown in Fig. 2.3.

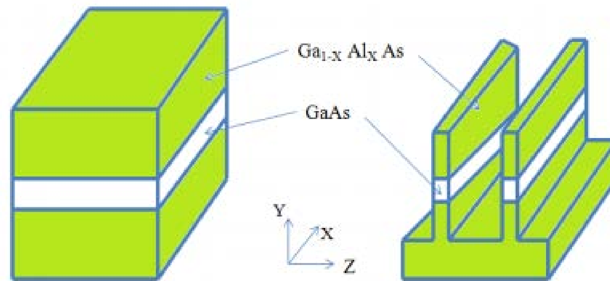

Figure 2.3: Schematic of a quantum wire structure.

Quantum wires can be used as electron waveguides, switchable high-speed lasers, nanotubes [28, 29].
The effects of electron-electron interaction become more pronounced when the transverse size of the quantum wire is of the order of the electron wavelength, and there is a single propagating mode. The motion of electrons along the longitudinal dimension is virtually 1D, and this leads to novel phenomena. The reason is that in 1D, the interaction between electrons is only weakly screened and interaction plays a central role. One of the most promising devices that exploit the fundamental properties of 1-D semiconductor structures is the nanowire field-effect transistor (NWFET). In such devices, quantum-wires provide smallness of the channel region, together with an excellent gate control, to enable fast switching and low off-currents [30, 31].

Quantum Dots

Quantum dots, due to the complete reduction of the remaining degree of freedom of a quantum wire, are very small semiconductor crystals in the order of nanometers. They confine electrons or electron-hole pairs called *excitons*. In order to understand the concept of excitons, one can consider the promotion of an electron from the valence band to the conduction band

in a bulk material, caused by thermal excitation or absorption of a photon, that leaves a hole behind. After a finite time, the excited electron will eventually recombine with a hole with the release of energy. In the case of QDs, when the size of the crystal material approaches its Bohr radius, the excited electron tends to form a weak bond with its hole. This bound state between carriers is called exciton (Fig 2.4). Every semiconductor material has its

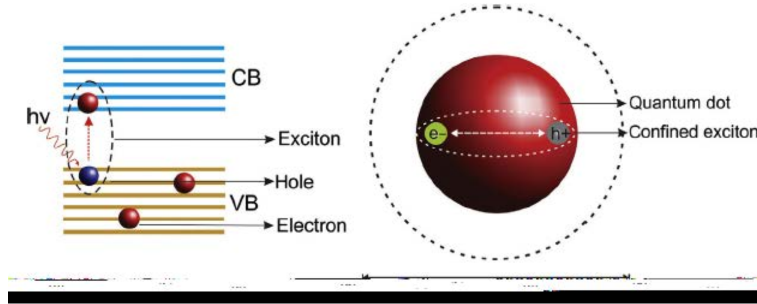

Figure 2.4: Formation of excitons in quantum dot energy bands with comparison respect to the QD size

own exciton Bohr radius below which the quantum confinement is realized. This property causes the band of energies to become discrete energy levels in QDs, so they are sometimes referred to as "artificial atoms" because they exhibit discrete electronic states as seen in atoms and molecules.
The optoelectronics properties of a QD are determined by their size and shape. For instance, larger quantum dots have a grater red spectrum-shift compared to smaller dots. As a consequence, these properties can be specifically tuned to have a desired output depending on the application field: in fact, QDs find application in many fields including solar cells, LEDs, transistors, laser diodes, quantum computing and medical imaging [32, 33, 34, 35, 36, 37]. Fig 2.5 illustrates the variation in the bandgap (and thus in the emission) of QDs as size varies.

To determine the emission energy of the first excited state (called *ground state GS*) of a quantum dot, the effective mass model leads to the expression [38]:

$$\Delta E = E_g^{bulk} + \frac{\hbar^2\pi^2}{2a^2}\left(\frac{1}{m_e^*} + \frac{1}{m_h^*}\right) - \frac{1.8q^2}{4\pi\epsilon a} \tag{2.5}$$

where a is the QD radius, m_e^* and m_h^* are the effective masses of the electron and the hole, respectively. The first term is the energy gap of the bulk material of which the quantum dot is made, the second term is the particle-in-a-box confinement energy for an electron-hole pair in a spherical quantum dot (this is the more convenient way to model real QDs), and the last term represents the Coulombic interaction due to exciton formation.
Fig. 2.6 illustrates the possible radiative and non-radiative transitions inside a quantum dot. Only optical transitions between energy levels with the

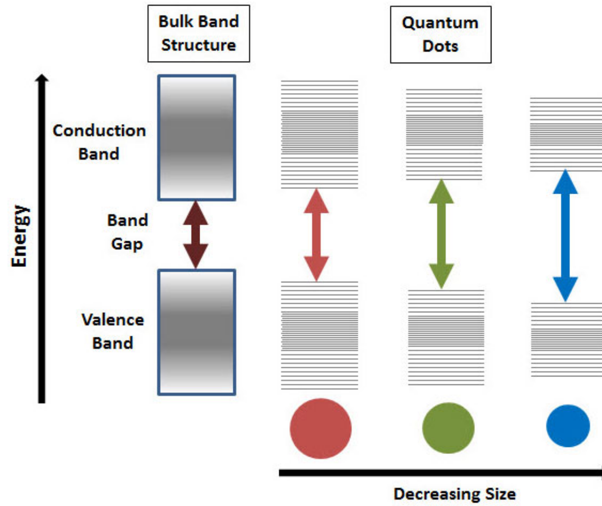

Figure 2.5: Correlation between QD size and bandgap.

same quantum number are considered. Typically the mean capture time of a quantum dot is in the picosecond range [39], which is very short compared to the nanosecond range of the non-radiative recombination time. Therefore, QDs also offer a robust and effective solution to defects and threading dislocations.

2.1.3 Two-States lasing

The existence of two-states lasing has been experimentally observed [40, 41]. The occupation of energy states rises with the injection of current, but then saturates for value above I_{th}. In the case of QDs, when the ground state starts lasing, its carrier population become clamped and GS inversion cannot increase further as any additional carriers added will be converted into GS lasing light. However, if the scattering process is included, as carriers are injected into the QW, if the GS is clamped, they can accumulate in the upper energy state (called *excited state ES*) or above. In this case, ES can reach inversion. Simultaneous emission is impossible to achieve for QW lasers, as the carrier population instantly equilibrates. In [40] it is demonstrated that the lower gain and the longer intersublevel relaxation compared to a QW, can lead to interesting effects such as simultaneous lasing at two state transitions.

2.1.4 Ground State quenching

Another interesting observation regarding two-state lasing is the complete roll-over of GS intensity for increasing currents, that has been studied and discussed in literature [42, 43, 44, 45]. This behavior is called *GS quenching*

and can be described with self-heating or electron-hole dynamics.
Self-heating of the device raises the device temperature, increasing the scattering processes and, thus, the carrier probability distribution. The ES gain is higher than the GS gain, so carrier heating tends to suppress ground state lasing and to lower the threshold of excited state lasing. When both levels have similar occupation numbers, the ES will therefore be the only state left lasing, as discussed in [46]. However, other authors report that GS quenching also occurs in pulsed mode [47, 48].
Another explanation considers a current-dependent homogeneous broadening, with consequent decrease ub the maximum gain [49].
Different energy separation factors and different transport time scales for holes and electrons could be concealed behind GS quenching, according to [50]. In fact, energy spacing and occupation for electrons and holes are not symmetric (Fig 2.2(b)), thus leading to a competition for holes between GS and ES in quantum dot structures. When holes occupation is low, ES will take over GS because of its higher degeneracy in terms of energy level (capture rate is faster, for instance).

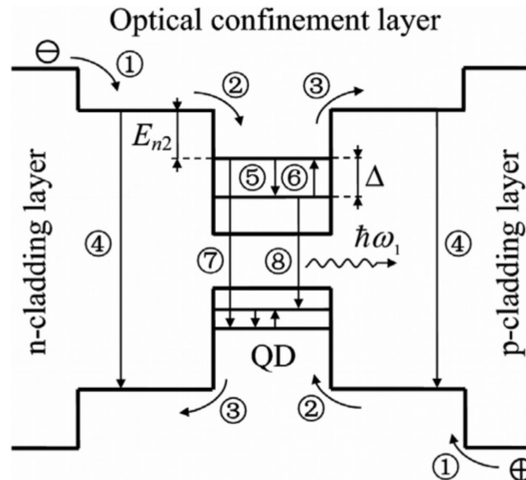

Figure 2.6: Energy band diagram of a QD laser. The main processes are: (1) carrier injection from the cladding layer to the optical confinement layer (OCL), (2) carrier capture from the OCL into the QD, (3) carrier escape, (4)spontaneous radiative recombination in the OCL, (5) intraband relaxation, (6) upward transition in the QD, (7) excited state radiative recombination and (8) ground state radiative recombination.

2.2 Self assembled quantum dots

The quantum dots of the devices studied in this thesis are obtained by the strain-induced self-organized growth technique called Stranski-Krastanov growth (SK-growth), which provides the possibility of island formation on a initially flat heteroepitaxial surface. Fig. 2.7 shows two typical growth modes for semiconductor heterostructures. When lattice constant is different and surface energy of the second layer is relatively low, SK growth mode occurs where growth mode changes from two- to three-dimensional. The

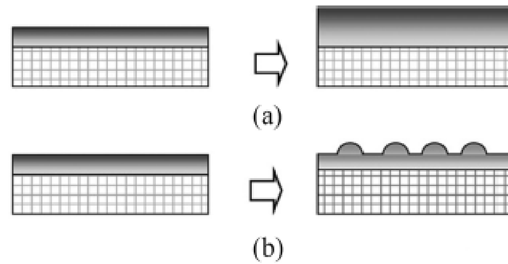

Figure 2.7: Typical growth modes for semiconductor heterostructures. (a) 2D growth, (b) from 2-D to 3-D growth.

surface is then covered by semiconductor islands without threading dislocations. From such growth mode, it is known that InAs quantum dots can be formed on GaAs. More in detail, one starts by sending fluxes of In and As on a thick GaAs substrate. The huge lattice-period mismatch between the two compounds (a_{InAs} = 6.06 Å, a_{GaAs} = 5.65 Å, $\Delta a_{InAs}/a_{GaAs}$ = 7 %) still leads to 2D growth: an In plane grows, followed by an As plane, forming a very thin InAs layer with GaAs lattice parameter in the layer plane, whose formation introduces a distortion of the atomic orbitals and thus excess energy in the chemical bonds. However, beyond a critical InAs thickness (d ≈ 0.7 monolayer, i.e. before the complete growth of one monolayer) the elastic energy accumulated by the distorted orbital bonds becomes too large. The nature of the growth changes spontaneously (thus the term "self-organized") to become three-dimensional (3D), which leads to the formation of unstrained (or less strained) InAs islands floating on a strained InAs "wetting" layer (WL). Fig. 2.8(a) schematically shows this growth technique. In Fig. 2.8(b) such high-density InAs QDs on GaAs surface is characterized by atomic force microscopy (AFM), resulting in a inhomogeneous distribution of islands with an average areal density of $10^{10} - 10^{11} cm^{-2}$. Thus, islands are fairly separated from each other and they can be considered as isolated QDs. Covering the strained InAs islands with GaAs allows the formation on a second layer of InAs islands on top of the first one. This so-called *capping* changes the shape of the QDs from purely pyramidal to truncated

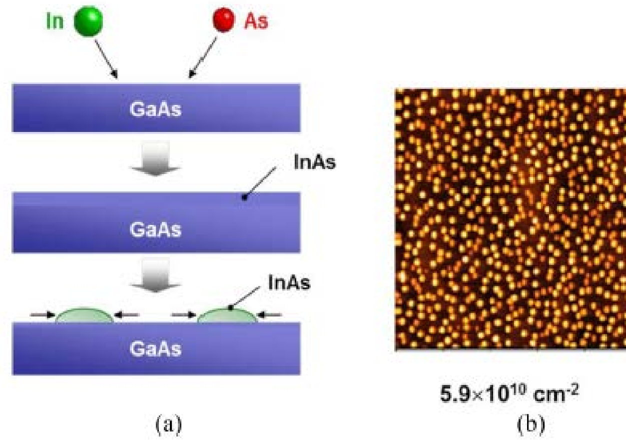

Figure 2.8: (a) Formation sequence of InAs self-assembled QDs. (b) atomic force microscope image (0.5 $\mu m\times$ 0.5 μm)of high-density InAs QDs on GaAs.

pyramidal [51], as shown in Fig. 2.9. The modelling of quantum dots is quite

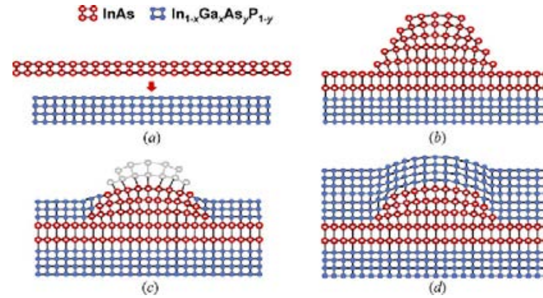

Figure 2.9: Schematic model for the capping process of the InAs QD structure: (a) Deposition of InAs layer, (b) formation of the 3-D structures, (c)-(d) deposition of GaAs capping layer and structure truncation.

complex for several reasons. Firstly, there is de facto a lack of precise sizes and shapes. This arises from the fact that characterization techniques are often destructive or are performed on samples that are different from those that have been used in optical measurements. It is well established that the dots' parameters crucially depend on the growth conditions. Moreover, one faces severe diffusion problems (e.g. In has a tendency to move towards the surface during growth) that generate non-trivial composition profiles inside the islands. Other parameters, such as the substrate temperature, also play an important part. Nowadays self-assembled quantum dots can be modelled as cones [52], pyramids [53] and lens-like [54].

Chapter 3

Defects in semiconductors

Crystalline solids exhibit a periodic crystalline structure. The positions of atoms or molecules occur on repeating fixed distances, determined by the unit cell parameters. However, the arrangement of atoms or molecules in most crystalline materials is not perfect. The regular patterns are interrupted by crystallographic defects. Even in good-quality crystals there are defects, which break the periodicity of the structure (Fig. 3.1), leading to the worsening of electrical and optical characteristics of the device. Defects

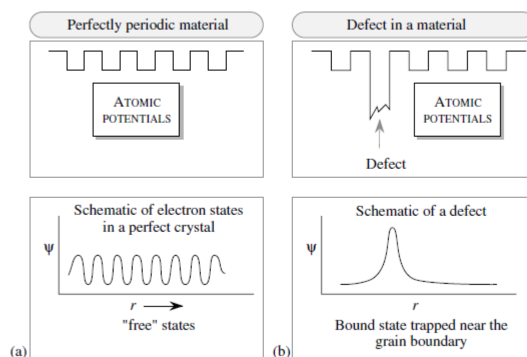

Figure 3.1: Structural and electronic properties of (a) an ideal crystal and (b) material with a defect

can break the crystal lattice regularity, that constitute the basis of the band theory on which the electrical behavior of the material is described, and can change the local resistivity of the material, with a consequence regarding the current distribution throughout the semiconductor. Moreover, defects usually act as non-radiative generation and recombination centers, decreasing the efficiency of the injected power.
In this chapter, the principal types of defects are presented. The main degradation mechanisms occurring as a consequence of the presence of defects will conclude the chapter.

3.0.1 Lattice deformations

The lattice constant difference between substrate and grown material creates strains inside the crystal lattice, that can change the length of the atomic bonds. Such a changing modifies the energy of the bonds, with variations in the charge transportation and in the optical emission, and can ultimately lead to the material breaking. Different mismatch cases are shown in Fig. 3.2, where an overlayer with lattice constant a_L is grown on a substrate with lattice constant a_S. If the strain between two materials is defined as

$$\epsilon = \frac{a_S - a_L}{a_L} \tag{3.1}$$

then after every $1/\epsilon$ bonds between the two layers, either a bond is missing or an extra bond appear as shown in Fig 3.2(b). Another case is shown in Fig. 3.2(c), where all the atoms at the interface of the substrate and the overlayer are bonded because of the overlayer lattice constant modification. In this case the overlayer is being strained and the system has a certain amount of strain energy.

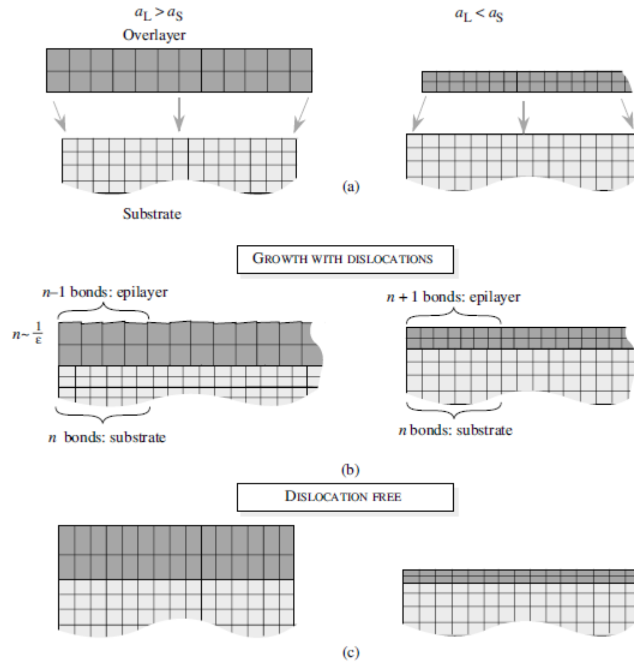

Figure 3.2: (a) An overlayer with one lattice constant is placed without distortion on a substrate with a different lattice constant. (b) Dislocations are generated at positions where the interface bonding is lost. (c) The overlayer is distorted so that the material is free of dislocation and coherent with the substrate.

3.1 Point defects

Point defects arise from missing atoms, atoms at the wrong sites, unintended impurities that only affect a region around their location. The simplest point defect is a vacancy, a missing atom at an atomic position. Defects are present in any crystal and their concentration is roughly given by

$$\frac{N_d}{N_{tot}} = A\ exp\left(-\frac{E_d}{k_B T}\right) \tag{3.2}$$

where N_d is the vacancy density, N_{tot} is the total site density in the crystal, E_d the defect formation energy, A is a dimensionless parameter and T the crystal growth temperature.
If an atom is at a position that does not belong to the crystal structure an interstitial (or Frenkel defect) is formed. These atoms can come both from elements belonging to the material (intrinsic defects) and from impurities (extrinsic defects), like elements of the deposition chamber. The electromagnetic field generated by the electrons of these atoms can modify the atomic shape and energy.
A substitutional impurity atom is an atom of a different type than the bulk atoms, which has replaced one of the bulk atoms in the lattice. Figure 3.3 sketches the point defects described above.

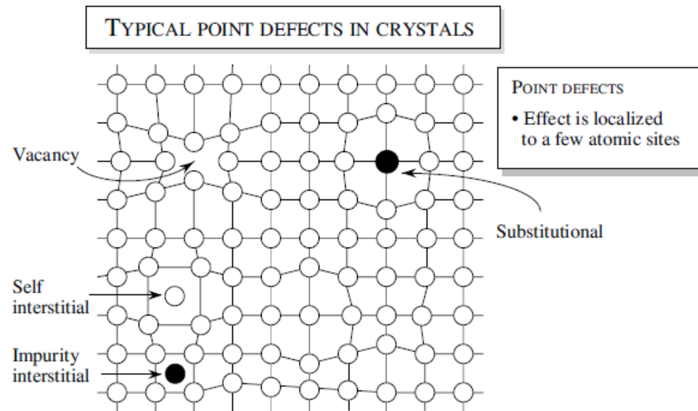

Figure 3.3: Schematic representation of point defects in a crystal

3.2 Dislocations

Dislocations, also called linear defects, are structures around which the atoms of the crystal lattice are misaligned. A threading dislocation is one that extends from the surface of a strained layer system, goes through the layer

and penetrates the substrate or bends at the interface into a misfit dislocation. The threading dislocations can be present in the heterostructure as a consequence of the crystal growth process. Most of the threading dislocations emerge from the substrate and thread through the epitaxial multilayer structure. Two different types of dislocation structures are shown in Fig. 3.4. The vector along the dislocation line is called line vector **L** and the vector **b** is the vector of the difference between a closed path in an ideal crystal and the dislocation core. An *edge* dislocation occurs if **L** and **b** are perpendicular to each other. For a *screw* dislocation **b** and **L** have the same direction. High concentrations of dislocations can act as non-radiative ge-

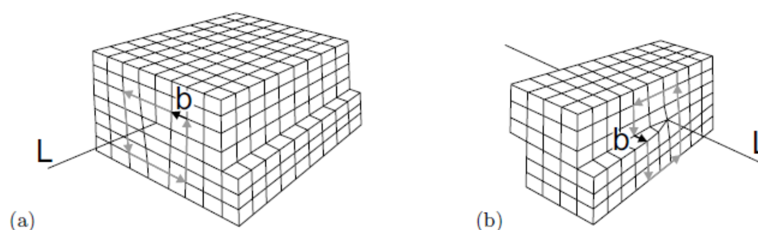

Figure 3.4: Model of (a) an edge and (b) a screw dislocation, with the respectively positions of the vectors **L** and **b**

neration/recombination centers, increasing the leakage current and reducing the optical efficiency of the material

3.3 Stacking faults

Stacking faults are caused by the lattice mismatch: inside the lattice, anomalies in the stacking sequence of crystal planes, that disrupt the continuity of a perfect lattice, occur in order to minimize the strain inside the material, resulting in different atomic layer sequences. Stacking faults present different characteristics respect on which direction they grow. Near the substrate, for instance, they generate defects that propagate vertically inside the material. However, the main effect of stacking faults is the modification of electrical characteristics such as the bandgap.

3.4 Degradation modes

The degradation processes are associated to the increase of defects and, therefore, to the non-radiative recombination processes. This mechanisms occur in a laser diode have a strong effect on the electrical and optical properties of the device, causing a reduction of the output optical power and an increase of the threshold current, and leading in some cases to the premature failure of the device. This modifications are mainly caused by the decrease of the

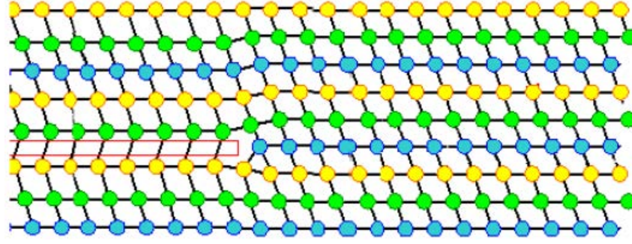

Figure 3.5: Schematic diagram of a stacking fault defect, highlighting the lattice modification

injected carrier lifetime and by the increase of the optical losses inside the active region. The degradation of the laser diodes occurs in different modes, which have their own characteristics depending on the substrate, layers and interfaces of the device, defects and strain of the materials. These factors, including external variables as temperature, current injection, optical power and ambient atmosphere, can lead to complex degradation mechanisms. Reliability of optical devices is limited by these degradation processes. An overview of the main degradation modes and the correlation between degradation mechanisms and the electrical and optical characteristics of laser diodes are presented in this section, further informations can be found in [57, 58, 59, 60].
The degradation of a laser diode can be observed as the evolution with time of either light output power at constant injection current or the operating current at constant light output power (Fig. 3.6). Examining the power

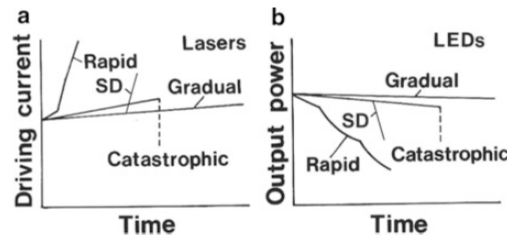

Figure 3.6: Time evolution of rapid degradation, gradual degradation and catastrophic degradation respect to (a) driving current and (b) output power

versus time and the current versus time plots, degradation can be classified as *rapid*, *gradual* and *catastrophic*, depending on the different time scales:

- Rapid degradation happens in the first hundred hours of operation. It appears as a quick decrease in the optical output power or increase in the driving current.

- Gradual degradation is the usual failure mode of a device operating

over its expected lifetime. In general, a gradual decrease in the quantum efficiency is observed.

- Catastrophic damage appears as a sudden failure after regular operation life of the laser and represents the end of the device lifetime [61]. Catastrophic degradation can occur inside the cavity or at the facet mirror and appears suddenly without a previous sign.

These degradation processes are closely related to the existence, generation and motion of defects within the laser structure: this means that defects must be avoided to allow good quality heterostructures.

3.4.1 Rapid degradation

Rapid degradation is associated with the presence of extended defects that destroy the active region of the laser and quench the optical emission. The study of these dark regions [62, 63] reveals two main defect structures: Dark Line Defects (DLDs) and Dark Spot Defects (DSDs), respectively shown in Fig 3.7. These defects appear as dense three-dimensional networks of dislo-

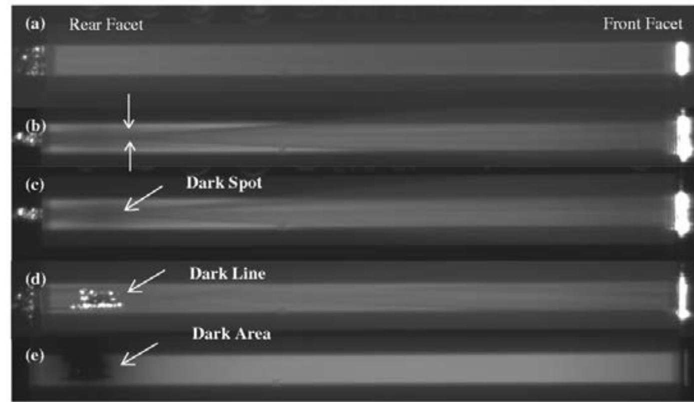

Figure 3.7: Snap shots of EL images captured from a laser diode at five different times: (a) initial condition, (b) self-focusing of light occurs, (c) a dark spot is developed, (d) dark line defects are developed and (e) dark line defects are developed into dark area defects [80]

.

cations, resulting in regions of very low optical efficiency: these clusters of crystal defects develop around a dislocation crossing the active layer and are found at the QW and the adjacent cladding layers.
The growth of the DLDs derives from the interaction between the dislocation, point defects and the minority carriers introduced in the active region by electric injection and optical generation due to self-absorption of the laser light inside the optical cavity. These dislocations can grow into networks

by non-radiative recombination processes with a growth rate promoted by the presence of mechanical strain and thermal gradients. The formation of DLDs is also sensitively dependent on the material system, and is much more pronounced in AlGaAs/GaAs than in InGaAsP/InP lasers: it has been reported that the presence of indium in the active layer increases the resistance of the material to dark-line defect (DLD) formation and propagation, and hence improves the optical strength and reliability of these diode laser types [65]. A DLD can act as a sink for injected carriers and as an absorber of laser light in the cavity. These effects can cause a rapid degradation of laser performance with final catastrophic failure in the active region due to strong Joule heating. The generation of dark defects is closely related to the reactions involving the generation, diffusion and motion of defects: these processes are thermally activated and are normally very slow, but can be accelerated by the energy released by non-radiative recombination of the injected carriers [64]. This mechanism is called Recombination Enhanced Defect Reaction (REDR). The dislocation motion proceeds by two different mechanisms, that eventually lead to the formation of DLDs:

- Recombination Enhanced Dislocation Climb (REDC)
- Recombination Enhanced Dislocation Glide (REDG)

Dislocation climb consists in the increase of the dislocation length mediated by either the absorption or emission of point defects, leading to the formation of dislocation loops and helical dipoles along one direction.
Two mechanisms can explain the dislocation motion by climb: absorption of extrinsic defects at the dislocation and emission of vacancies [63], emission of point defects by absorbing vacancies, intrinsic defects [62, 66].
Dislocation glide is characterized by the generation of 60° dislocation along the <100> direction of the crystal by a glide process from a dislocation source in the presence of minority-carrier recombination events. The dislocation velocity has been shown to depend on carrier injection rate and temperature, [67, 68] stress [69] and bandgap energy. It can also be influenced by the energy of the particular deep level involved [70].
Dark Spot Defects are observed as dark spot-like regions in the Electroluminescence (EL) images of the active region: large DSDs become efficient light absorbers, inducing a local increase in the cavity temperature around the DSDs [71]. The generation rate of DSDs increases with injection current [59], which can increase the non-radiative recombination process in the formation of DSDs.
Elimination of rapid degradation can be achieved [60]:

- using dislocation-free substrates to avoid the dislocation propagation into the active layer
- minimizing internal stress at the interface between the active waveguide and cladding layers to reduce REDC and REDG formation

- reducing the defects induced during fabrication processes such as diffusion, dielectric and metal depositions, ion implantation.

3.4.2 Gradual degradation

Gradual degradation corresponds to a slow and progressive decay of the optical output power throughout the device lifetime. The EL image shows a homogeneous darkening of the active region (Figure 3.7 shows the progressive darkening of the active region of a laser). The effect is due to the formation of point defects, for instance, by REDR. Deep levels can be observed by Deep Level Transient Spectroscopy (DLTS) and the concentration of these levels increases with operation time of the device [72]. Gradual degradation can be described as the following feedback mechanism: new point defects are produced by non-radiative recombination at already existing defects, assisted by REDR; these point defects further reduce the optical efficiency through non-radiative recombination phenomena, assisting the formation of other new point defects. The rate of this sequence of events depends on the concentration of defects and the quality of interfaces, as well as the stress distribution around the material.
The gradual degradation is typically a thermally activated process, for which the lifetime of the laser can be expressed by the following expression [73]:

$$\tau = \tau_0 \; exp\left(\frac{E_a}{k_B T}\right) \tag{3.3}$$

with E_a the activation energy, that for the degradation of lasers has been measured around 0.4-0.9 eV, lower than the required energy for defect formation and diffusion (2.6 eV) [74]. This further underline the role of non-radiative recombination in this degradation mode.
The elimination of deep-level defects, traps and impurities during the device fabrication processes can reduce the gradual degradation.

3.4.3 Catastrophic degradation

Catastrophic degradation, usually associated with the Catastrophic optical mirror damage (COMD), can also occur at the inner part of the cavity [75]. The degradation starts with a power reduction before any detectable degradation of the optical cavity, followed by a very fast degradation caused by dark defects. The degradation pattern is, thus, similar to rapid degradation, with the difference of the different time scale: in fact rapid degradation can be observed within the first 100 hours of operation, while catastrophic degradation appears after many hours of normal operation with a sharp output power decrease.
Both degradation modes are caused by the formation of dense networks of dislocation, but the growth rate of dark defects for catastrophic degradation is

considerably faster and appears without any previous warning. Dislocations inside the depletion layer, but outside the active region, could be responsible for this sudden degradation: they would approach the active region, assisted by non-radiative recombination processes, and quickly elongate as soon as they enter into the active region, causing the sudden degradation [75]. This could be the consequence of high concentration of point defects in lasers after long operation times that should activate the propagation of DLDs. The role of impurities diffusion could also produce disorder in heterostructures [76], suggesting an active p-type impurity outdiffusion in the case of AlGaAs/GaAs lasers in [77].

Facet degradation

Catastrophic optical mirror damage (COMD) consists in the destruction of the mirror facets, an event that strongly limits the lifetime of high power laser diodes. COMD is triggered by non-radiative recombination at the facet mirror, that releases thermal energy to the lattice, increasing the local temperature. This induces a band gap narrowing in the region close to the mirrors that leads the absorption rate to dominate over the stimulated emission rate, which finally leads to a thermal runaway with ultimate facet meltdown [78], as sketched in Fig. 3.8. Therefore, the main cause of facet degradation is the

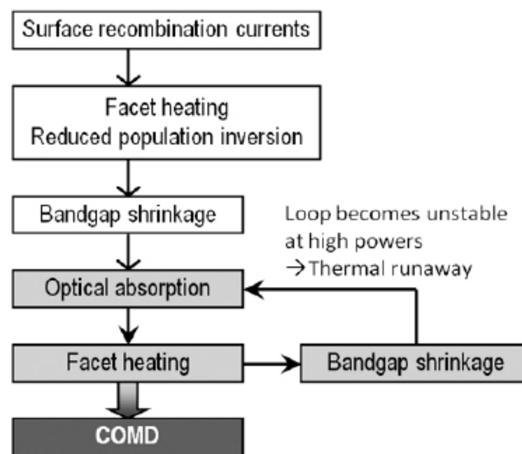

Figure 3.8: Generation mechanism and feedback loop leading to COMD

high temperature, which is the result of non-radiative recombination. Other factors are the density of defects at the facet, the facet treatment and coating, the temperature dependence of the bandgap of materials forming the active region, the thermal conductivities of the different layers forming the laser structure. The facet temperatures were found to depend on the *surface*

recombination velocity[1] showing the importance of the facet treatment for COMD [79]. In order to reduce COMD, passivation layers and films can be used to minimize the surface recombination velocity. Another solution can be the use of nonabsorbing mirror structures. A TEM image of a COMD is shown in Fig. 3.9

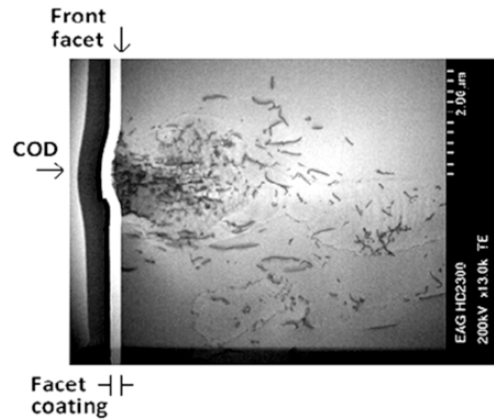

Figure 3.9: A melted-resolified region containing some material defects

[1]The surface recombination velocity is given by [60]: $v_s = N_s v_{th} \sigma_s$, with σ_s the minority carrier capture cross-section at the surface, N_s the surface state density.

Chapter 4

Experimental details

In this chapter, the epitaxial structures of the quantum dot laser diodes studied in this thesis work are presented. Then, the different experimental setups and instruments are described, followed by the preliminary characterization of the devices under test (DUTs).

4.1 Structure of the devices under test

The devices under investigation are Fabry-Perot laser diodes with an active region composed of three or five stacks of quantum dot layers, provided by the University of California, Santa Barbara (UCSB). Two bars (called "Bar3" and "Bar4") of epitaxially grown devices on silicon substrate and one bar (called "Die2 Bar4") in which the substrate is native (GaAs) were tested. The devices are narrow-ridge waveguide quantum dots lasers, with a cavity length of 1 mm. Every bar has 26 nominally identical devices: the first 13 have a ridge width of 3 μm whereas the other 13 were processed with a 6 μm ridge width. The bars are provided without packaging and pins for the external connection to a single device.
Regarding the devices on silicon substrate, the epitaxial structure starts with an on-axis (001) GaP/Si substrate. The pseudomorphic GaP layer is 45 nm thick and has been grown by metal-organic chemical vapor deposition (MOCVD). The lattice mismatch between GaP and Si is very small, so it is possible to deposit GaP on a Si substrate without any misfit formation and with an anti-phase domains (APDs) free surface. Anti-phase domain is a type of planar crystallographic defect in which the atoms within a region of a crystal are configured in the opposite order to those in the perfect lattice system. These planar defects are similar to stacking faults in that they are often created through slip of atomic planes and dislocation motion. The metamorphic growth of the desired III-V layer can then follow: a n-type GaAs buffer layer was grown on the top of the GaP/Si substrate in a molecular beam epitaxy (MBE) chamber with $In_{0.1}Ga_{0.9}As/GaAs$ strained superlattice

dislocation filter layers, in order to reduce the threading dislocation density (TDD).
The active region consists of 3 layers of InAs quantum dots embedded in ∼9 nm of $In_{0.15}Ga_{0.85}As$ quantum wells, which are separated by Be-modulation-doped ($N_A = 5 \times 10^{17} cm^{-3}$) GaAs barriers. The modulation p-doping approach increases the capture rate of holes from the QDs, thus partially solving the GS-quenching phenomenon mentioned in Chapter 2. The InGaAs film beneath the QDs, also called *wetting layer* (WL), is used to form the quantum-dot-in-a-well (QD-WELL) structure. When electric current is injected into the active region, the WL constitutes a reservoir for carriers that leads to a filling or depletion of the confined quantum dots.
The active region is embedded in a waveguiding structure to confine the light and enhance the stimulated emission inside the optical medium. Unlike conventional heterostructures, where the band energy changes abruptly at the active region, the waveguide is realized by growing a GaAs/AlGaAs graded-index separate confinement heterostructure: in other words, the cladding materials are organized so that their bandgap is reduced so as to meet the smaller bandgap material.
After the epitaxial growth, the material was processed into ridge-waveguide lasers with a width of 3 μm and 6 μm, using standard dry-etching techniques, corresponding to a device area of, respectively, 3000 and 6000 μm^2. The cavity length was defined by cleaving the end facets, in order to obtain the two mirrors and thus realizing a resonant optical cavity.
A schematic representation of the epitaxial structure of the devices and a sketch of flat-band diagram at 300 K is shown in Fig. 4.1.

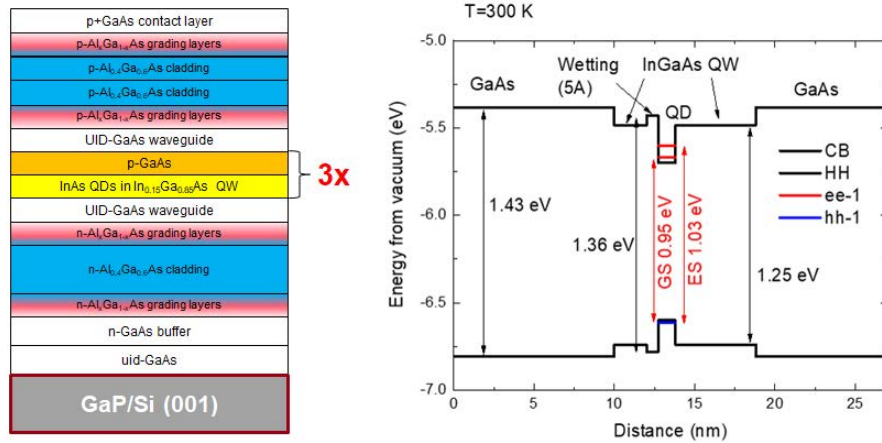

Figure 4.1: Simplified epitaxial structure of the silicon-substrate samples under investigation. The right portion of the figure shows the simulation of a flat-band diagram of the active region at 300 K.

A scanning-electron-microscopy (SEM) [81] front-view of one of the devices is shown in Figure 4.2. The protruding semiconductor material on the top of the n-GaAs buffer layer, over which the n-contact metal is placed, is called *mesa* and can be seen from the SEM image. In the image, it is possible to observe the metal contacts, the quantum dot layers and the GaAs buffer layer.

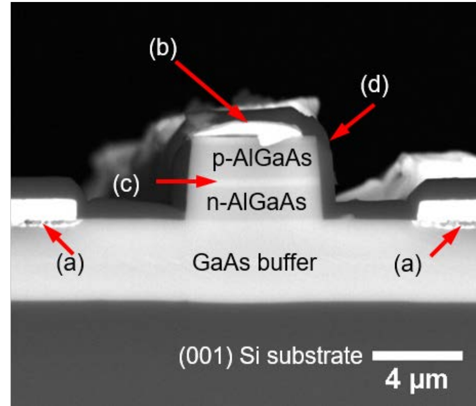

Figure 4.2: Front-view of a single device highlighting (a) the n-contact metal, (b) the p-contact metal, (c) the QD layers and (d) the SiO_2 isolation

A top-view of the bar is shown in Figure 4.3, where the cathode and the anode are the left and right strips, respectively, allowing the contact of the device to the electrical instrumentation through tungsten probing tips. Each probe tip is held on one end by a probe arm shaft which, in turn, is attached to a micro-manipulator.

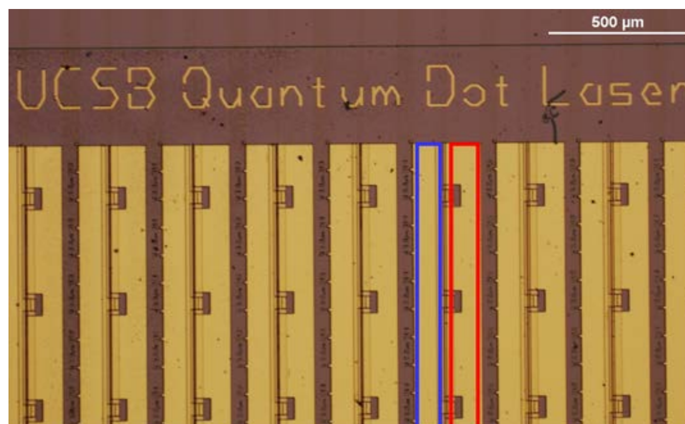

Figure 4.3: Top-view of a portion of the bar. The cathode strip (blue) and the anode strip (red) can be seen.

Regarding the native-substrate-device bar, the lasers follow the epitaxial growth processes mentioned above with some differences respect to the silicon-bar devices:

- the epitaxial laser stack is grown on a **thicker** substrate of **gallium arsenide** and therefore is free of misfit and threading dislocations ($7.3 \times 10^6 cm^{-2}$) [82],
- the active region consists of **5** layers of InAs quantum dots embedded in ∼**7** nm of $In_{0.15}Ga_{0.85}As$ quantum wells (3 layers in ∼9 nm of $In_{0.15}Ga_{0.85}As$ quantum wells for the silicon-substrate device),
- high-reflection **facet coating** was applied on one side of the bar to reduce optical carrier loss and improve light amplification,
- an additional separate confined heterostructure made of $Al_{0.2}Ga_{0.8}As$ to further improve carrier confinement.

Figure 4.4 illustrates the epitaxial structure of the lasers.

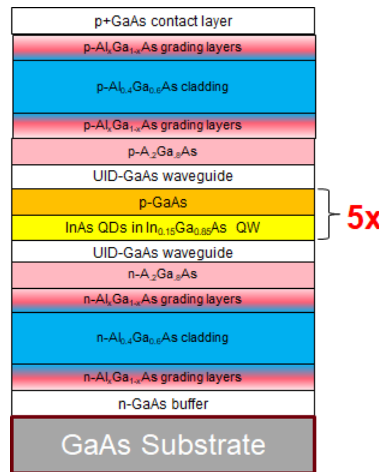

Figure 4.4: Simplified epitaxial structure of the native-substrate samples under investigation.

4.2 Stress and characterization at room temperature

To study the devices under test, a probe station, whose instruments will be described in this section, was used and several stress-test experiments have been performed. Electrical and optical parameters were monitored during time at different bias levels.
For the electrical characterization a *source meter* was employed: it integrates

many different source and measurement capabilities into one compact form factor, being able to source and measure both voltage and current. To observe the optical characteristics of the laser, both a photodetector (PD) and an optical spectrum analyzer (OSA) were used. A Thorlabs fg200lea bifurcated fiber was able to redirect the light coming out of the laser cavity towards both instruments: the fiber, also known as fanout or Y-cable, is constructed from 19 high-grade optical fibers that are mapped to a 10-fiber end and a 9-fiber end.
A Thorlabs ACL12708U uncoated aspheric condender lens was placed in front of the emitting facet of the device under test in order not to lose lateral optical beam emission. The bar was placed on top of a Peltier device, driven by a precision temperature controller, in order to impose the ambient temperature of the DUT. A picture of the probe station employed for the stress-experiments is shown in Figure 4.5, with a detail of the Peltier cell, the aspheric lens and the probe tips in Figure 4.6. As previously mentioned,

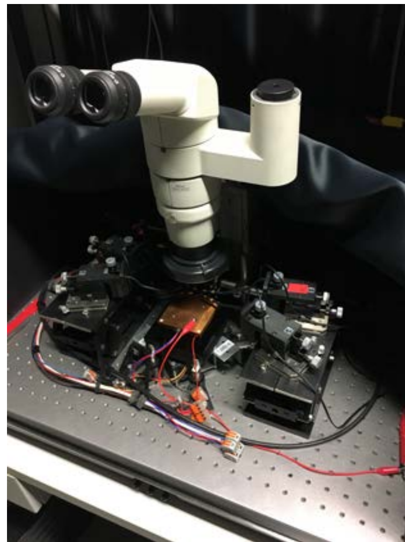

Figure 4.5: Picture of the probe station. A microscope is used for the precise positioning of the tips through the arms of the manipolators, fixed on a magnetic base.

the lasers are contacted by probe tips, each of which is fixed on a micromanipulator through a probe arm shaft. The manipulators are stabilized by a magnetic base, thus enabling the fine and precision positioning of the tip. Every tip is connected to the inner conductor (the core) of a coaxial cable. The probe station setup employs a 4-wire sensing technique, also known as *Kelvin sensing*. This method uses separate pairs of current-carrying and voltage-sensing electrodes to make more accurate measurements than the simpler two-wire sensing. In particular, the current is supplied by a

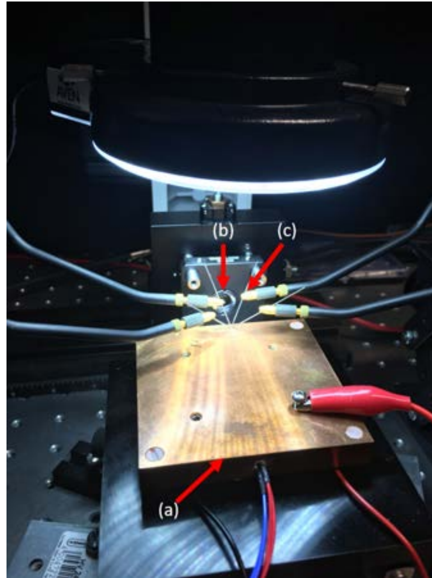

Figure 4.6: Detailed view of the probe station. (a) The copper Peltier cell, (b) the aspheric lens and (c) the probe tip connected to the arm shaft of manipulator.

pair of force connections (one denoted as high, for the anode, the other as low, for the cathode), while the sense connections provide for the voltage measurement. The sense measurement is more accurate because the voltage leads do not include the voltage drop of the force leads or contacts, thus eliminating cable resistance effects so that only the voltage drop across the DUT is measured. A schematic representation of a 4-wire sensing technique is shown in Figure 4.7.

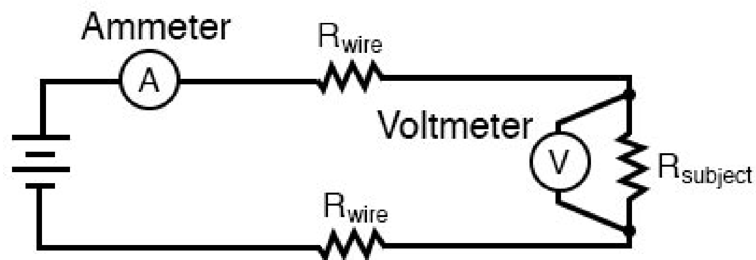

Figure 4.7: Schematic sketch of a 4-wire Kelvin sensing technique

4.2.1 Source meter

The source meter employed in the probe station is a Keysight B2912A. It is a compact and bench-top precision instrument that employs two Source/Measure Units (SMUs). SMUs are popular and widespread instrument for performing measurements in many different fields and applications due to their integrated voltage and current sourcing and measurement capabilities. SMUs are extensively used for test applications requiring high accuracy, high resolution and measurement flexibility. Such applications include I-V characterizing and testing semiconductors and other non-linear devices and materials, where voltage and current sourcing spans across both positive and negative values. SMUs also possess a voltage and current limit (compliance) feature that allows to set limits and to protect devices from damage caused by excessive voltage or current.
The instrument is equipped with a GPIB interface to enable connection to a computer, from where a *LabView* software allows the control of the automated test equipment. One of the two SMUs was used as a 4-terminal unit, thus enabling the current-bias of the DUT and the simultaneous sensing of the device voltage and viceversa. The second SMU was used for the connection to the photodetector, which simply requires a voltage sensing.

Photodetector

To detect the light output power of the laser diodes, a Thorlabs PDA50B Germanium-based Transimpedance Amplified Photodetector (PD) was used. A germanium junction photodiode generates a photocurrent when light is absorbed in the depleted region of the junction semiconductor. An external reverse bias needs to be applied to increase the width of the depletion junction, producing an increased responsivity with a decrease in junction capacitance. The output of the photodetector is a voltage signal (from 0 V to 10 V) that is linearly proportional to the input optical power. To increase the signal level, it is possible to adjust the gain of the transimpedance amplifier, from 0 dB to 80 dB, by step of 10 dB. As mentioned before, the voltage provided by the photodetector is monitored by the second Source/Measure Unit (SMU) of the source meter.

4.2.2 Temperature controller

The DUTs were placed on top of a TEC cooler, that is a copper plate on top of a Peltier cell whose temperature can be regulated with high precision by an Arroyo Instruments 5310 temperature controller. The Peltier cell is cooled through external fans. The controller is able to stabilize the plate temperature by means of a PID feedback system; the temperature sensing is performed by a resistance temperature detector (RTD). It consists

of a platinum resistance embedded into the cold plate which has an accurate resistance/temperature relationship, and thus provides an indication of temperature.

4.2.3 Optical spectrum analyzer

The Yokogawa AQ6370D optical spectrum analyzer (OSA) was used for the spectral measurements of the DUTs. An OSA is a precision instrument designed to measure and display the distribution of power of an optical source over a specified wavelength span, in this case nominally from 600 nm to 1700 nm. In this case, the OSA trace displays power in the vertical scale and the wavelength in the horizontal scale.
The input to the optical spectrum analyzer is a FC/PC optical connector, on which one end of the bifurcated fiber previously mentioned was attached. The instrument uses a monochromator to spatially separate the wavelength of the incoming light, with an optical detector placed at the output slit. A schematic illustration of the Czerny-Turner monochromator employed in the OSA is shown in Figure 4.8. It can be seen that the incoming light is collimated by a first mirror, which reflects the light to the diffraction grating. The grating spatially separates the different wavelengths of the incoming radiation. A second mirror then focuses the light on the optical detector. As the diffraction grating inside the monochromator moves, bands of different frequencies (wavelengths) are identified by the detector.

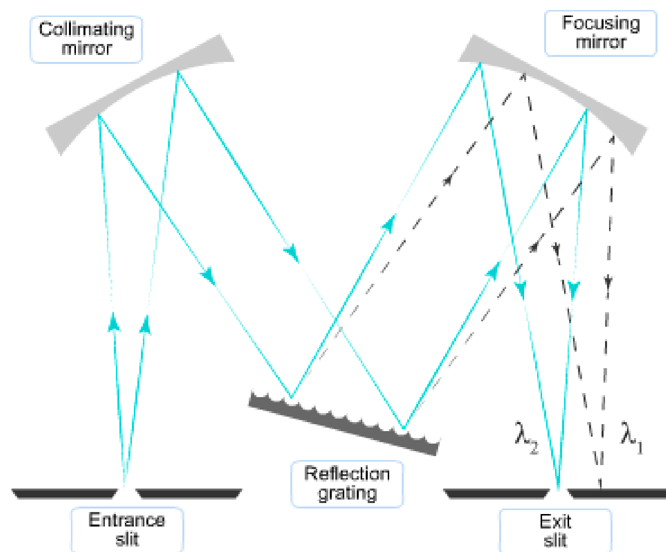

Figure 4.8: Czerny-Turner monochromator schematic, showing how it is possible to separate different wavelengths λ_1 and λ_2 through two mirrors and a diffraction grating.

4.3 Characterization at cryogenic temperatures

I-V and L-I measurements were performed on a silicon-substrate device in order to extrapolate and analyze the device characteristics at low temperatures. Additionally, Deep Level Transient Spectroscopy (DLTS) analysis was also carried out, in order to analyze the presence of deep levels near/within the space charge region.
Three devices of the bar were bonded on a PCB support and placed in an open loop cryogenic chamber of liquid nitrogen, that was connected to a system for capacitance DLTS by SULA Instruments: the main blocks of this system are a Lakeshore 335 Temperature Controller, whose heater and thermocouples were connected to the cryogenic chamber, and a capacitance meter, that measures the small signal capacitance while biasing the device to the proper DC bias voltage. The C-V measurements are carried out at 1 MHz. Figure 4.9 displays the bonded bar, ready to be mounted into the cryogenic chamber shown in Figure 4.10. The instruments employed for

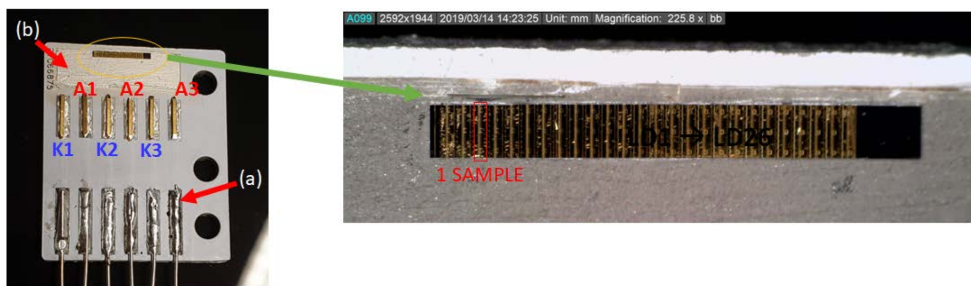

Figure 4.9: PCB board over which the bar is attached with (a) the pins connected to the cathodes (K1, K2, K3) and anodes (A1, A2, A3) of the three devices and (b) the paste solder process needed to place the bar over the PCB support

the I-V and L-I characterizations were a HP 4155A Parameter Analyzer and a Thorlabs PDA36A2, that is an amplified, switchable-gain, silicon detector designed for detection of IR light. To further analyze the devices behavior at different temperatures, an Agilent 8114A Pulse Generator was employed to deliver precise voltage/current pulses, and a RIGOL DS4054 4-channel oscilloscope was used for data displaying and measurement. In the next section, the fundamentals of DLTS are presented.

Deep Level Transient Spectroscopy

As already mentioned, impurities atoms and intrinsic defects can introduce energy levels in the bandgap of the material and act as non-radiative recombination centers for carriers, thus lowering the electrical and optical performances of the devices.

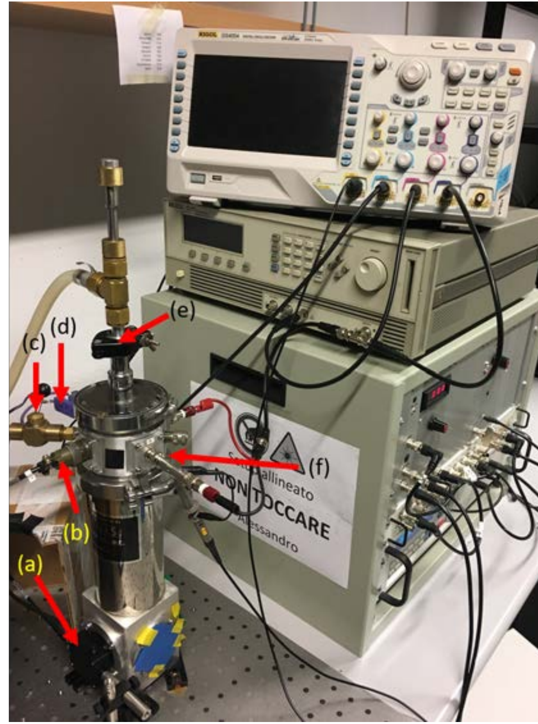

Figure 4.10: Picture of the open loop liquid nitrogen in the setup for the pulsed measurements. In the image it is possible to recognize (a) the detector, (b) the connection for temperature controller heater, (c) the vacuum pump entrance, (d) the thermocouples, (e) the liquid nitrogen chamber entrance and (f) the coaxial cable connection.

Defect states are referred to majority or minority carrier traps. A majority carrier trap is one that is induced to capture a majority carrier in the relative doped-type material and is then subsequently observed by the effect that the emission of that carrier has on the junction capacitance.
Considering an abrupt p$^+$-n junction diode, thus assuming that the SCR only extends toward the n-side, the junction capacitance C has already been calculated as

$$C = \frac{A\epsilon}{W} \tag{4.1}$$

with A the area of the junction, ϵ the dielectric constant of the semiconductor and W the width of the depletion region, that is given by

$$W = \sqrt{\frac{2\epsilon(\phi_i - V)}{qN_A}}. \tag{4.2}$$

Equations 4.1 and 4.2 suggest that a variation of applied voltage causes the junction capacitance to change. This variation is closely related to the thermal emission from a deep level, as shown in Figure 4.11: assuming a junction

with a majority-carrier trap having its energy E_T, in steady state condition the traps under the Fermi level are filled with carriers. However, varying the voltage applied to the junction (in this case a reverse bias) causes the traps to thermally emit carriers, to reach a new steady-state condition. Consequently, if the concentration of trapped charge is changed, this variation can be monitored by observing the corresponding change in the junction capacitance and can be only ascribed to deep levels, since carriers thermally emitted from traps are swept out of the layer in a very short time, typically 10^{-10} - 10^{-12} s [83]. Capacitance transients can be obtained by holding the

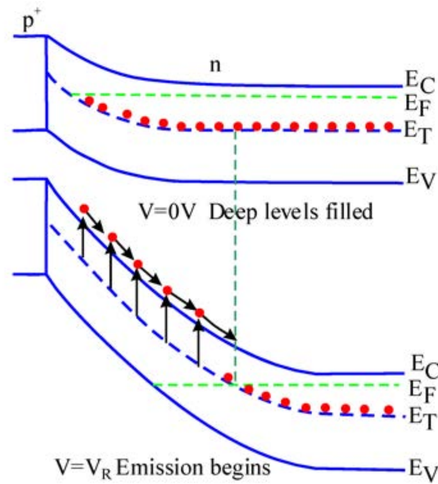

Figure 4.11: Basic concept of thermal emission of carriers from a deep level. The energy band bending due to reverse bias causes the emission of carriers from traps above the Fermi level.

sample at constant bias and temperature and applying a single filling pulse, as shown in Fig. 4.12. The resultant isothermal transient reveals that, when starting from a steady state value, the voltage is momentarily increased. Additionally, part of the region which was formerly within the space-charge region is now in neutral material, so that the traps are below the Fermi level: they can capture carriers and tend to become filled. Immediately after the pulse, the deep levels that are again within the SCR start emitting carriers and a capacitance transient will be produced. In the classic DLTS method, the capacitance transient is measured at two different times t_1 and t_2, and the difference $\Delta C = C(t_1) - C(t_2)$ is plotted as a function of the sample temperature to generate the DLTS spectrum. Scanning the sample temperature varies the time constant of the thermal emission transient, and the resulting signal is maximized when the emission rate matches the rate window of the instrument. An typical result can be seen in Figure 4.13.

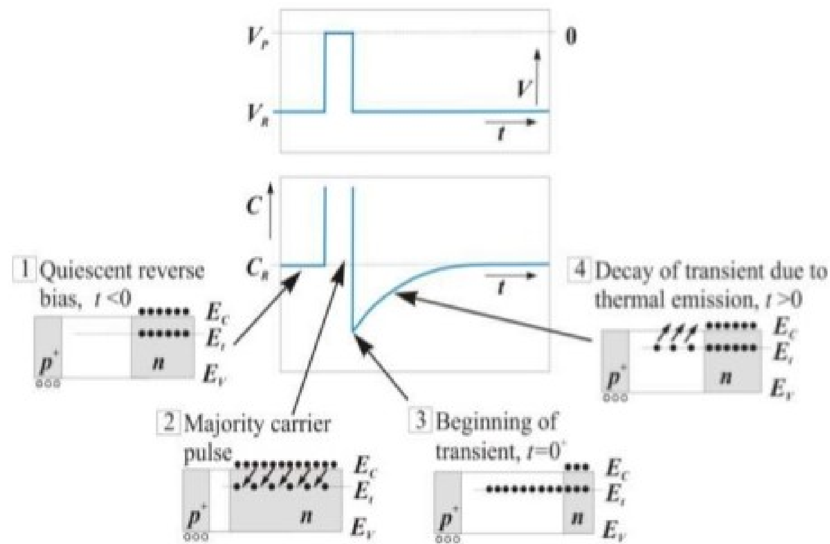

Figure 4.12: Isothermal capacitance transient for thermal emission of the majority carrier traps. The condition for the trap occupation during various phases of the transient are shown.

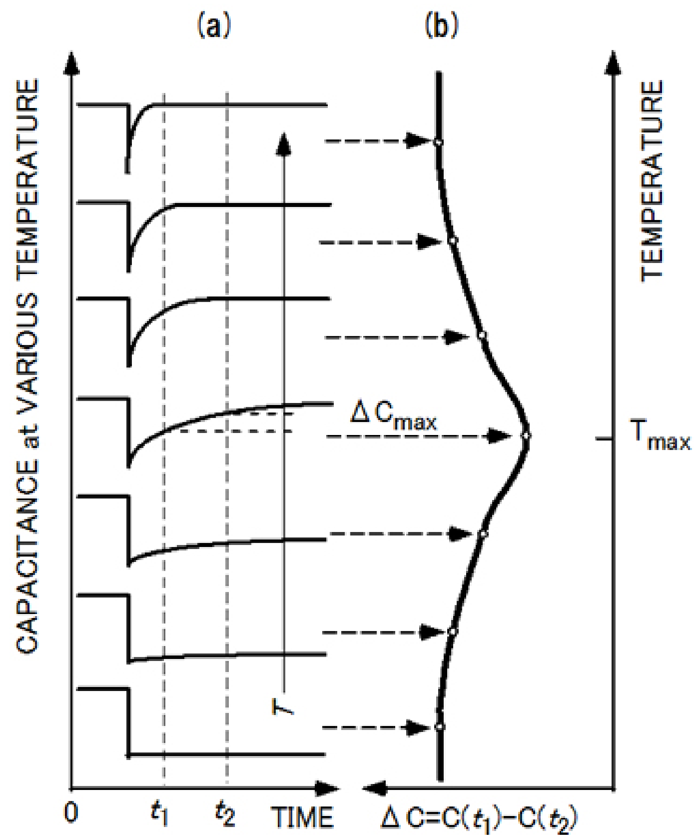

Figure 4.13: Application of the rate window concept. The left-hand side shows how the emission transient varies with temperature, while the right-hand side shows the corresponding DLTS signal calculated as the difference between the capacitance values at time t_1 and t_2

DLTS can provide different information about the deep levels, such as the nature of majority/minoiry carrier trap: in fact, a capacity transient due to majority carrier-emission is always negative [85]. Other characteristics that can be drawn out of DLTS signals are the trap activation energy, i.e. the thermal energy needed to free the carrier from the defect, and the trap capture cross section.
The trap capture cross sections for capturing electrons and holes are σ_n and σ_p, respectively. The electron capture rate is given by

$$c_n = \sigma_n N_C v_{th} \tag{4.3}$$

with N_C the electron concentration and $v_{th} = \sqrt{\frac{3k_BT}{m_e^*}}$ the thermal velocity of electrons, depending on the effective mass of electrons m_e^* in the material. Analogous for holes.
Thermal emission rates are proportional to a Boltzmann factor [84]

$$e_n = c_n exp(-\Delta E_A/k_BT) = (\sigma_n N_C v_{th}) exp(-\Delta E_A/k_BT) \tag{4.4}$$

where N_C represents the effective density of states in the conduction band, v_{th} is the electron thermal velocity and ΔE_A is the trap activation energy. Therefore, the emission time constant is given by

$$\tau_e = (\sigma_n N_C v_{th})^{-1} exp(\Delta E_A/k_BT), \tag{4.5}$$

By taking the temperature dependence of N_C and v_{th} into consideration, the activation energy and capture cross section of interface traps can be derived from the $\tau_e \sim T$ curves. The electron thermal velocity and the effective density of states in the conduction band are

$$v_{th} = \sqrt{\frac{3k_BT}{m_e^*}}, \quad N_C = 2(2\pi m_e^* k_BT/h^2)^{\frac{3}{2}}, \tag{4.6}$$

allowing the emission time constant to be written as the Arrhenius equation [86]:

$$\tau_e T^2 = (\gamma_n \sigma_n)^{-1} exp(\Delta E_A/k_BT), \tag{4.7}$$

with $\gamma_n = \left(\frac{v_{th}}{\sqrt{T}}\right) \cdot \left(\frac{N_C}{\sqrt{T^3}}\right)$.
A plot of the $ln(\tau_e T^2)$ values versus $1/k_BT$ (the Arrhenius plot) enables a straightforward determination of the activation energy and the cross section of the traps. The slope of the curve indicates the activation energy, while from the intercept of the fitted curve it is possible to calculate the capture cross section.
Finally, the concentration of traps can be obtained directly from the capacitance change [85]:

$$\frac{N_T}{N} = 2\frac{\Delta C}{C}1 \tag{4.8}$$

where N_T is the trap concentration, ΔC is the capacitance change corresponding to the maximum value of the DLTS spectrum, C is the capacitance of the diode under quiescent conditions and N the net carrier concentration.

4.4 Preliminary device characterizations

All the 26 devices from each bar were characterized by I-V and L-I measurements at an ambient temperature of 25°C. At the time the preliminary characterizations were carried out, the probe station was not yet equipped with the aspheric lens and the optical spectrum analyzer was not used, thus the photodetector was directly placed on front of the DUT, without the need of the bifurcated fiber.
The I-V measurement provides the current-voltage characteristic between the electric current through the device and the corresponding voltage across it. To carry out such a measurement, the source meter is programmed to perform a DC voltage sweep and simultaneously record the current flowing through the device. For the L-I measurement the source meter acts as a current source on the first SMU, and as a precision voltmeter on the SMU connected to the photodetector, performing a linear current sweep.
From now on, all the measurements on the samples are to be considered as 4-wire sensing measurements. The I-V and L-I plots are separated for the two groups of devices because of the different laser cavity widths, 3 μm for devices 1 to 13, and 6 μm for devices 14 to 26.

Silicon-substrate Bar4 devices

The I-V and L-I characteristics are plotted in Figure 4.14 and Figure 4.15, respectively. The I-V plot is also shown in semi-logarithmic scale, in order to evaluate the electrical behavior at small current values. It can be seen that some devices have a higher leakage current with respect to the others, in particular device QD9 and QD22 seem to have an unusual high parallel resistance, which can be associated to an increased lateral conduction, maybe due to a bad passivation process or a badly performed cleaving. Devices QD6, QD18 and QD24 show an abnormally high reverse leakage current, possibily associated to a high defect-density. Regarding the L-I plot, it can be noticed that there are devices, like QD11 and QD17, that start to emit light only at very high bias currents and, moreover, their optical power is extremely low when compared to the other lasers. The low slope-efficiency of some lasers (QD6, QD13 and QD17) is probably related to poorly reflecting mirrors, which could have been damaged during the cleaving process of the bar. The threshold current of every device was extracted by means of linear fitting of the L-I curves and the overall electrical and optical characteristics are summarized in Figure 4.16 As expected, the threshold current of the

second group of devices is higher, indeed for their larger width ridge and, thus, active region volume. A higher injection current is needed.

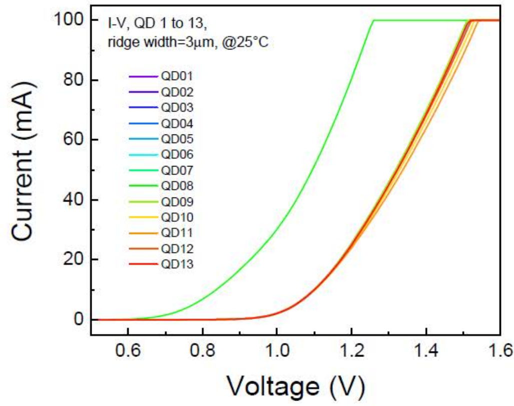

(a) Devices 1 to 13.

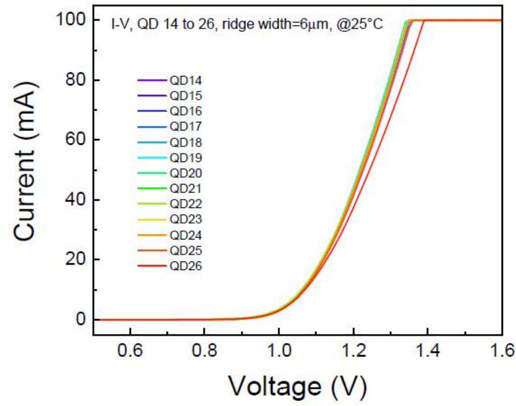

(b) Devices 14 to 26.

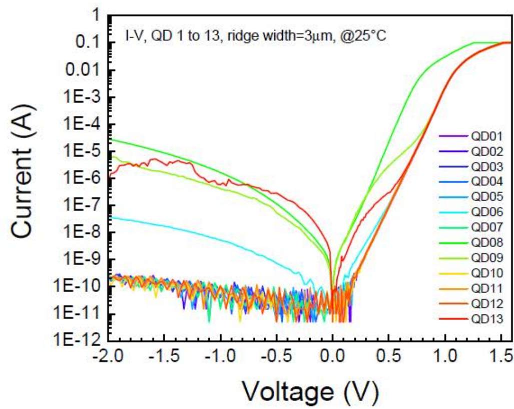

(c) Devices 1 to 13.

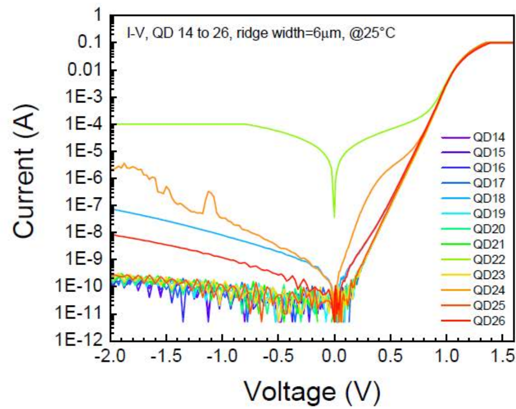

(d) Devices 14 to 26.

Figure 4.14: I-V characteristics of "Bar4" silicon-substrate devices, both in linear and semi-logarithmic scale.

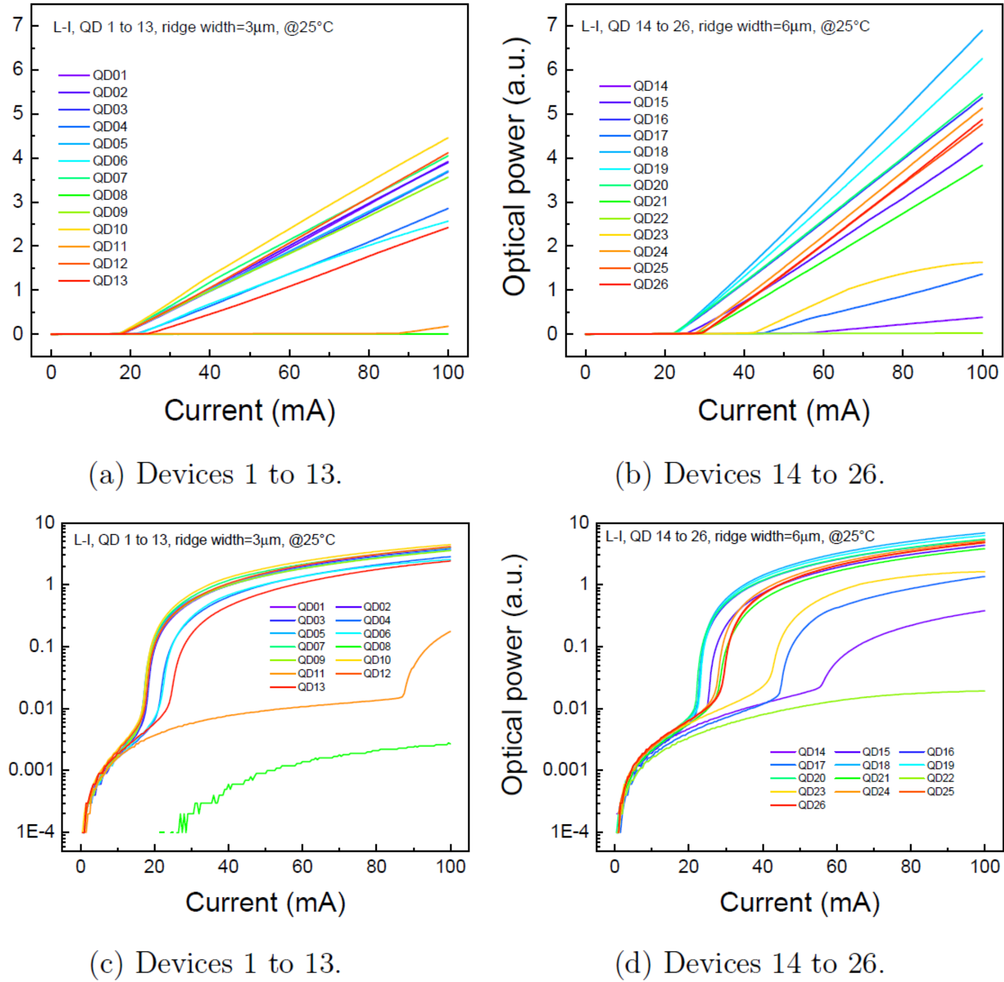

(a) Devices 1 to 13.

(b) Devices 14 to 26.

(c) Devices 1 to 13.

(d) Devices 14 to 26.

Figure 4.15: L-I characteristics of "Bar4" silicon-substrate devices, both in linear and semi-logarithmic scale.

Device	Width (µm)	I_{th} (mA)	Notes	Device	Width (µm)	I_{th} (mA)	Notes
1	3	17.71	healthy	14	6	n.a.	good I-V, bad (LED-like) emission
2	3	17.10	healthy	15	6	25.47	good I-V, bad emission
3	3	17.99	healthy	16	6	22.50	healthy (low SE)
4	3	21.52	good I-V, high Ith, low SE	17	6	44.22	good I-V, bad emission (high Ith, low SE)
5	3	17.01	healthy	18	6	22.56	high reverse current, good emission
6	3	22.01	high reverse current, high Ith, low SE	19	6	22.84	healthy
7	3	17.10	healthy	20	6	22.01	healthy
8	3	n.a.	high reverse current, no emission	21	6	28.46	healthy (low SE)
9	3	17.23	high reverse current, good emission	22	6	n.a.	bad I-V, no emission
10	3	17.23	healthy	23	6	41.77	good I-V, bad emission (high Ith, low SE)
11	3	n.a.	good I-V, bad (LED-like) emission	24	6	27.54	good emission
12	3	17.68	healthy	25	6	29.12	healthy
13	3	24.32	high reverse current, high Ith, low SE	26	6	29.07	high reverse current, good emission

Figure 4.16: Summary of the threshold current values obtained from the preliminary characterization of the "Bar4" devices. Green values represent healthy devices, yellow ones have bad electrical/optical features, red ones have either very high threshold current or are not emitting at all.

A second characterization of the devices from 14 to 26 of the same bar was performed after the bonding process, in order to choose the three devices to be bounded. The results are shown in Figure 4.17.

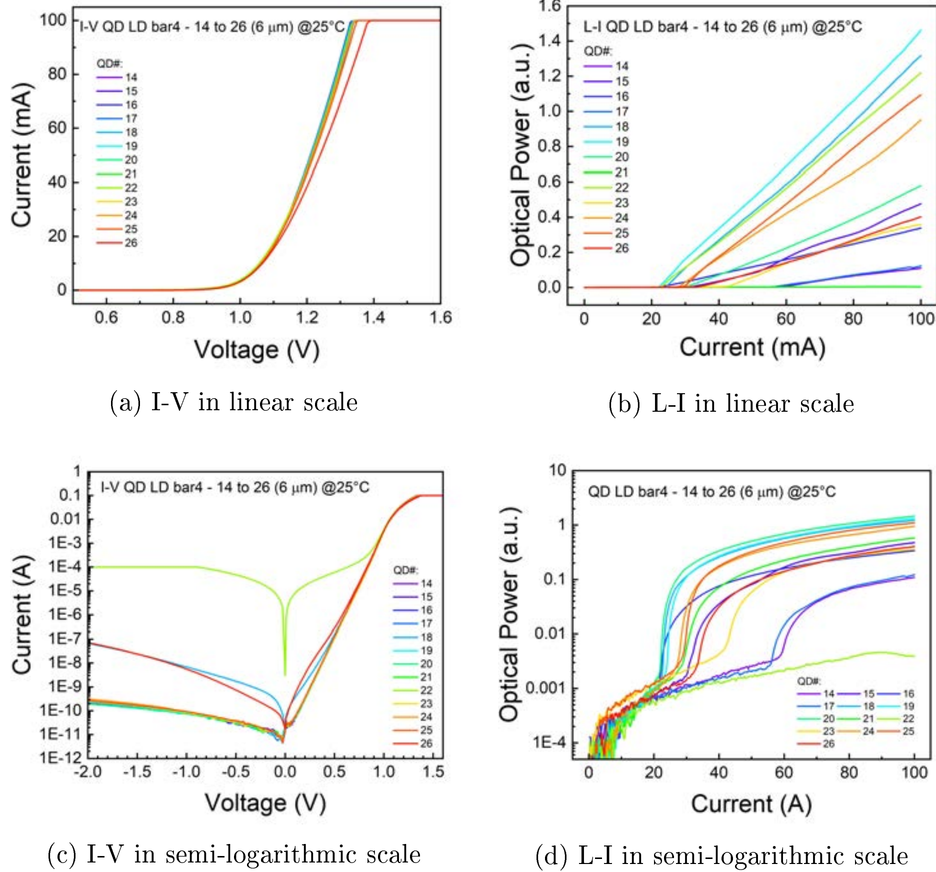

(a) I-V in linear scale

(b) L-I in linear scale

(c) I-V in semi-logarithmic scale

(d) L-I in semi-logarithmic scale

Figure 4.17: I-V and L-I characteristics of "Bar4" devices, both in linear and semi-logarithmic scale.

Respect to the healthy devices of Figure 4.16, QD15, QD19 and QD25 now have higher reverse and low-forward leakage current, as well as QD26. The L-I plot shows the major differences, probably ascribed to the solder process. In general, there is a worsening in the optical emission. Respect to the L-I curves, and excluding QD19 that was previously used for the current-step stress discussed in the next chapter, QD16, QD18 and QD20 were chosen to be used for the bonding process.

Silicon substrate Bar3 devices

The same characterization was performed on the other silicon-substrate bar and the results are presented and summarizes in Figures 4.18, 4.19 and 4.20. Regarding the I-V curve QD1, QD19, QD23 and QD25 show a very high reverse current. All the devices, except QD1, QD7, QD17, QD22, QD24 are healthy and show a good emission curve.

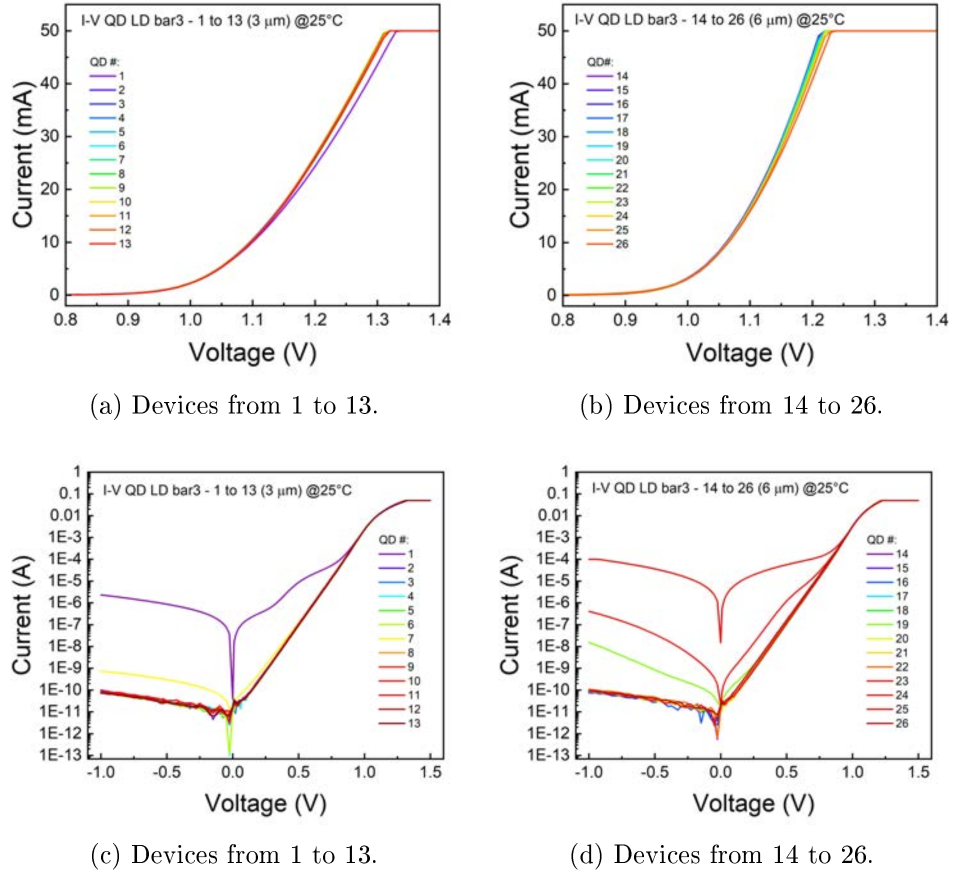

(a) Devices from 1 to 13. (b) Devices from 14 to 26.

(c) Devices from 1 to 13. (d) Devices from 14 to 26.

Figure 4.18: I-V characteristics of "Bar3" silicon-substrate devices, both in linear and semilogarithmic scale.

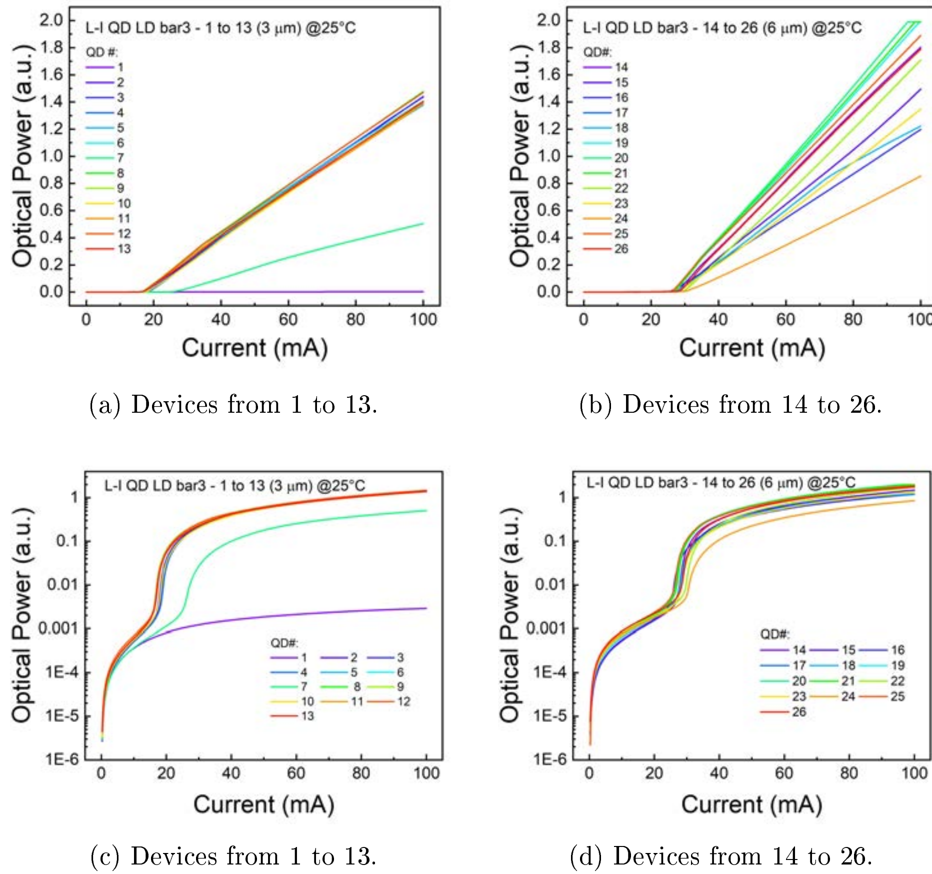

(a) Devices from 1 to 13.

(b) Devices from 14 to 26.

(c) Devices from 1 to 13.

(d) Devices from 14 to 26.

Figure 4.19: L-I characteristics of "Bar3" silicon-substrate devices, both in linear and semilogarithmic scale.

Width (µm)	I_{th} (mA)	Notes	Device	Width (µm)	I_{th} (mA)	Notes
3	n.a.	high reverse current, no emission	14	6	27.55	healthy
3	18.03	healthy	15	6	27.81	good I-V
3	17.69	healthy	16	6	25.41	good I-V
3	18.53	healthy	17	6	n.a	broken
3	16.69	healthy	18	6	27.39	good I-V
3	26.04	high reverse current, low SE, high Ith	19	6	26.54	high reverse current, good emission
3	16.70	healthy	20	6	26.60	healthy
3	16.51	healthy	21	6	26.80	healthy
3	16.56	healthy	22	6	29.41	good I-V, low SE, high Ith?
3	17.90	healthy	23	6	27.96	leakage in reverse/forward current
3	16.62	healthy	24	6	29.77	good I-V, low SE, high Ith?
3	16.87	healthy	25	6	26.09	high leakage in reverse/forward current
3	16.70	healthy	26	6	28.30	good I-V, good emission, high Ith?

Figure 4.20: Summary of the threshold current values obtained from the preliminary characterization of the "Bar3" devices. Green values represent healthy devices, yellow ones have bad electrical/optical features, red ones have either very high threshold current or are not emitting at all.

Native substrate Die2 Bar4 devices

The results of the I-V and L-I characterization of the devices are shown in Figure 4.21 and Figure4.22. It must be noted that this bar was physically divided into 8 different pieces, therefore the unusual high number of the devices in bad conditions can be ascribed to the cutting process. In fact, QD1, QD2, QD3, QD6, QD7, QD9, QD10, QD18, QD20, QD21 and QD25 are not emitting because they are shorted, as can be noted in the I-V graphs. Only QD11, QD14, QD16, QD17, QD22, QD23 and QD26 present a low reverse current and a good emission, thus they can be considered healthy, as summarized in Figure 4.23.

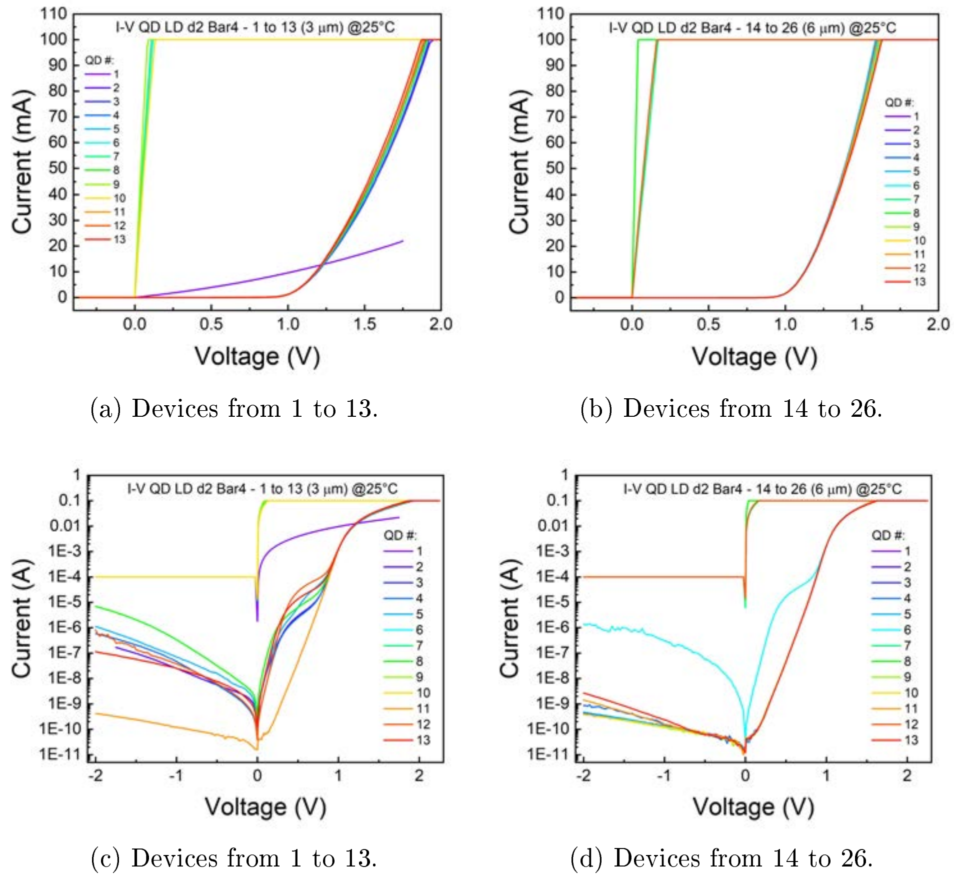

(a) Devices from 1 to 13.

(b) Devices from 14 to 26.

(c) Devices from 1 to 13.

(d) Devices from 14 to 26.

Figure 4.21: I-V characteristics of "Die2 Bar4" native-substrate devices, both in linear and semilogarithmic scale.

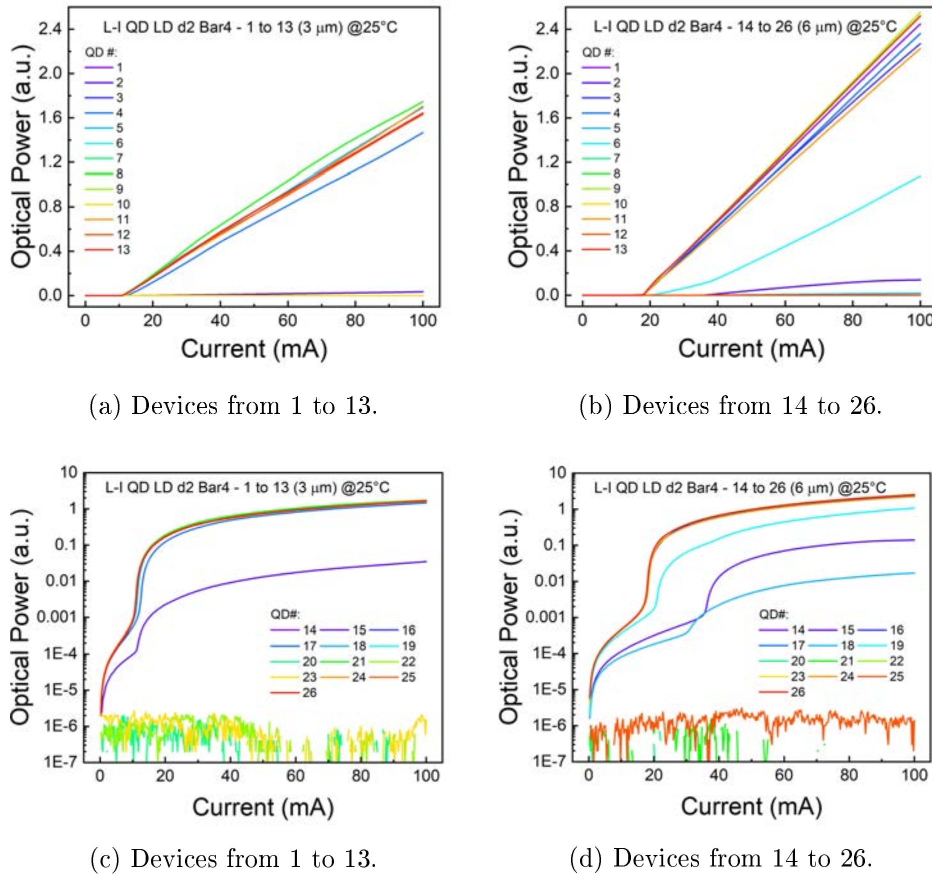

(a) Devices from 1 to 13.

(b) Devices from 14 to 26.

(c) Devices from 1 to 13.

(d) Devices from 14 to 26.

Figure 4.22: L-I characteristics of "Die2 Bar4" native-substrate devices, both in linear and semilogarithmic scale.

Device	Width (μm)	I_{th} (mA)	Notes	Device	Width (μm)	I_{th} (mA)	Notes
1	3	n.a.	no emission	14	6	17.86	healthy
2	3	n.a.	no emission	15	6	34.79	good I-V, high Ith, LED-like emission
3	3	n.a.	no emission	16	6	17.85	healthy
4	3	12.39	bad I-V, high Ith	17	6	17.98	healthy
5	3	11.31	bad I-V	18	6	32.36	good I-V, LED-like emission
6	3	n.a.	no emission	19	6	20.79	bad I-V, hight Ith, low SE
7	3	n.a.	no emission	20	6	n.a.	no emission
8	3	10.94	bad I-V, good emission	21	6	n.a.	no emission
9	3	n.a.	no emission	22	6	18.09	healthy
10	3	n.a.	no emission	23	6	17.83	healthy
11	3	10.85	healthy	24	6	17.98	healthy (low SE)
12	3	10.85	bad I-V, good emission	25	6	n.a.	no emission
13	3	10.89	bad I-V, good emission	26	6	17.77	healthy

Figure 4.23: Summary of the threshold current values obtained from the preliminary characterization of the "Die2 Bar4" devices. Green values represent healthy devices, yellow ones have bad electrical/optical features, red ones have either very high threshold current or are not emitting at all.

In the next chapter, it will be presented different current step-stress and constant-current-stress experiments performed on the samples, focusing on the comparison of the two different substrates. The chapter will end with the study of one device at cryogenic temperatures, including the DLTS results.

Chapter 5

Results

Following the results presented in the previous chapter, it was possible to determine which of the lasers were properly working and, thus, the most suitable for the stress experiments.
Before proceeding with the presentation of the results, a general description of the stress test procedures will follow.

Characterization pre- and post-stress

Before and after the stress, a characterization of the device was performed, varying the junction temperature. For every temperature value, the characterization was carried out by performing

- I-V measurement,
- L-I measurement,
- Electro-luminescence spectra at different current values, with a delay of 60 or 120 seconds between the end of a measure and the subsequent one.

Current step-stress

In a current step-stress the DUT is biased at a given current for a fixed amount of time, at the end of which the stress level (current) is increased and held for the same amount as before. The step duration was set to 60 minutes, with the bias current and step value chosen to compare different devices on equal current (or current density, depending on the cases). The experiments were always conducted at an ambient temperature of 35°C. Between each stress cycle, a complete characterization of the DUT was carried out by performing I-V, L-I, and spectral measurements at different current values. A delay of 300 seconds between the end of one step and the subsequent

characterization was employed. 60 seconds between each characterization measurement in order to stabilize the DUT temperature. During each step of the stress cycle, at the actual step-current, three spectral measurements were performed, at 1, 25 and 50 minutes from the beginning of the step. The spectra were set to a narrow- and wide-span values, in order to obtain high-resolution data. During the entire stress experiment, the device voltage and the output voltage of the photodetector were constantly monitored by the source meter.

Constant-current stress

In a constant-current stress, the device is submitted to a constant bias for prolonged time, in order to observe the operating condition of the laser during the stress. The constant-current experiments were performed at 35°C and have been divided in different stress-steps, this time each with the same bias-current. The duration of the steps was selected in order to get a logarithmically spaced sampling, as degradation processes in constant-level stresses are expected to show similar non-linear degradation kinetic.
Just like with the current step-stress, I-V, L-I and spectral measurements were conducted between each step and the voltage and the optical power were measured during the whole step duration, as well as additional spectra measurements with the same time spacing logarithmic rule mentioned before.

In the following sections a first current-step stress will be presented, containing some useful data interpretation and results for the following part: the two different substrates will be compared by means of a current-step stress and a constant-current stress both performed on different GaAs- and Si-substrate devices. The chapter will conclude with the study of a silicon-substrate device at cryogenic temperature and the DLTS results.

5.1 Silicon-substrate "Bar4" current step-stress

The current step-stress was performed on a 6 μm ridge width device (QD19) of the so-called "Bar4" silicon-substrate bar. Stress current was increased by 10 mA every hour, starting from 10 mA. The experiment was interrupted at 600 mA, i.e. the double value chosen for the 3 μm channel width devices that suggested to cause a significant degradation of the device.

Laser characteristics during stress

The L-I characteristics, both in linear and in semi-logarithmic scale, measured at different stages of the stress, are shown in Figure 5.1. It can be noted that the optical degradation becomes stronger for currents higher than 450 mA. The degradation kinetics can be clearly seen in Figure 5.2, that reports

the relative threshold current I_{th} and the slope efficiency SE trends as a function of stress time/current: in particular, when the current values are low, the threshold current increases slightly, while for higher stress currents ($I > 450$ mA) a significant faster degradation is observed. On the other hand, the slope efficiency, taken both near and far above threshold, shows a faster decrease for current values higher than 450 mA. These two quantities were extrapolated via linear fitting from the linear plot of Figure 5.1. The thre-

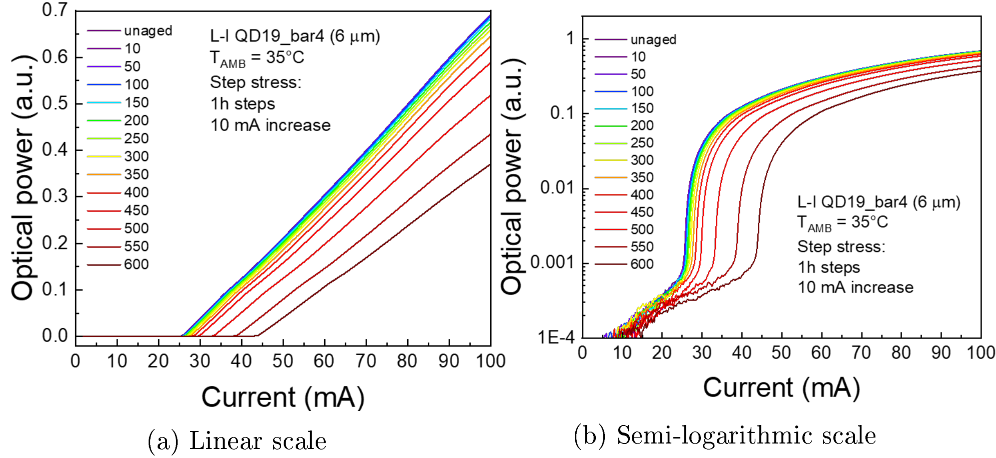

(a) Linear scale

(b) Semi-logarithmic scale

Figure 5.1: L-I characteristic as a function of the stress-time (not all the steps are shown for clarity). Due to the limited dynamic range of the photodetector, the sub-threshold region is relatively noisy.

shold current increases from 100% to 115% of its unaged original value, up to the 170% at 600 mA. The slope efficiency gradually decreases from 100% to 90% for currents lower than 450 mA, with a rapid variation to 74-70% from 450 mA to 600 mA. Interestingly, this phenomenon occurs in correspondence of the onset of the excited state ES emission, as shown later on.
To better understand the degradation process in place, it can be shown in Figure 5.3 that the variation of I_{th} is inversely correlated to the variation of SE. Both quantities can be calculated as function of the carrier injection efficiency η_{inj}, representing the fraction of the increment in current through the active area of the device which results in an increment in the total recombination current in the QD-WELL. In Chapter 1, the slope efficiency SE was defined as the optical power P in the lasing emission in terms of the diode current I above I_{th}

$$SE = \frac{\Delta P}{\Delta I}. \tag{5.1}$$

This quantity is directly related to the external differential quantum efficiency, defined as the increase in number of output photons per second respect

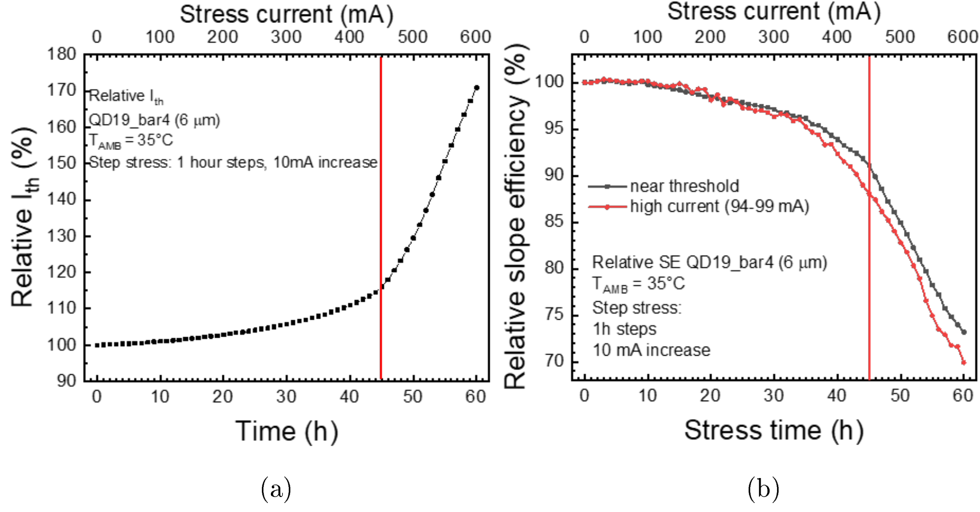

Figure 5.2: (a) Relative threshold current and (b) slope efficiency variation during the step-stress experiment.

to the increase in number of injected electrons into the diode per second:

$$\eta_{ext} = \frac{\Delta P/h\nu}{\Delta I/q} = SE\frac{q}{h\nu} \tag{5.2}$$

The external quantum efficiency can be also expressed as

$$\eta_{ext} = \eta_{inj}\frac{\alpha_{mirror}}{\alpha_{mirror} + \alpha_{internal}} \tag{5.3}$$

with α_{mirror} and $\alpha_{internal}$ the mirror and internal losses, respectively. Substituting Equation 5.3 in Equation 5.2 it is possible to obtain:

$$SE = \eta_{inj}\frac{\alpha_{mirror}}{\alpha_{mirror} + \alpha_{internal}}\frac{h\nu}{q} \tag{5.4}$$

This correlation can suggest that a decrease in SE can be caused by the increase/decrease in mirror/internal losses or by a decrease in injection efficiency, depending on the dominant factor.
Regarding the I_{th}, it can be found that this quantity is inversely proportional to the injection efficiency:

$$I_{th} = \frac{qVN_{th}}{\eta_{inj}\tau} \tag{5.5}$$

with N_{th} the threshold carrier density, V the volume of the active region and τ the electron lifetime.
Therefore, a linear correlation between I_{th} and 1/SE may be related to a decrease of the injection efficiency η_{inj}. Carriers might not even reach the

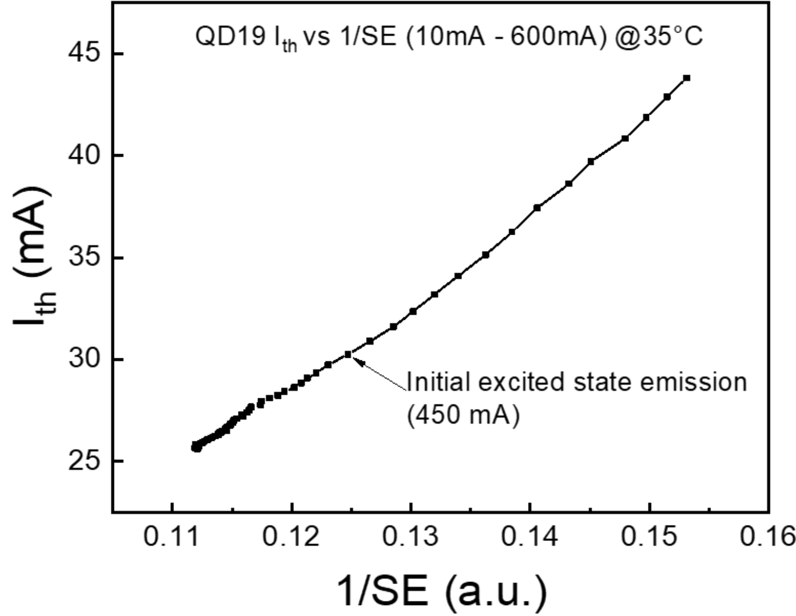

Figure 5.3: Relation between the variation of I_{th} and 1/SE.

active region due to the increase of potential barriers or electrostatic repulsion that occur at the boundary of the active region. The linear correlation could also indicate a higher escape rate of the carriers or losses due to recombination in the layer outside the active region. In either case, an increase of the non-radiative recombination processes occurs, thus leading to a reduced optical output power. Moreover, the reduction of the injection efficiency can conveniently be explained by a decrease of the non-radiative lifetime with respect to the relaxation time, i.e. the average time for a carrier in a quantum well to get captured by a quantum dot. It is therefore more probable for an injected carrier to recombine in the QW rather than into a QD, where it could recombine in a radiative manner.
The I-V curves taken at the beginning of each step of the stress are reported in Figure 5.4. The plots shows no significant change in the electrical characteristics of the sample during the experiment. From Figure 5.4(b) an increase in the reverse leakage current can be appreciated, as well as a slight increase in the low-forward bias current. As already mentioned in Chapter 1, a change with respect to the ideal characteristic of the diode is related to conduction paths originated from defects and damaged regions. Additionally, deviations in the ideality factor, indeed, indicate that either there are defect-related recombination mechanisms taking place, for instance due to

the generation of new defects that can increase the leakage current, or that the recombination is changing in magnitude. The ideality factor was already defined in Equation 1.21 as function of the applied voltage:

$$n(V) = \frac{q}{k_b T} \left(\frac{\partial ln(\sigma_D)}{\partial V} \right)^{-1} \tag{5.6}$$

Figure 5.5 displays the ideality factory of the device under stress as a function of the diode voltage. The same calculation was done before and after the stress experiment, at different temperatures. It should be noted that at low voltages the shunt resistance dominates the device performance, and, together with the strong temperature dependence of the ideality factor, the modeling of the I-V characteristic with the Shockley diode equation may not be valid and thus the corresponding ideality factor values are not meaningful. For voltage values between 0.3 V and 0.85 V, the ideality factor is around 2, suggesting that the conduction is dominated by the defects-related recombination currents within the SCR of the device. During stress the variation becomes stronger for higher voltages, thus suggesting an increased contribution of defect-related conduction mechanisms. The region of voltages greater than 0.85 V shows a significant raise of the ideality factor: it is indeed the region where the diode starts conducting. There is no significant variation of the diode "turn-on" voltage after stress.

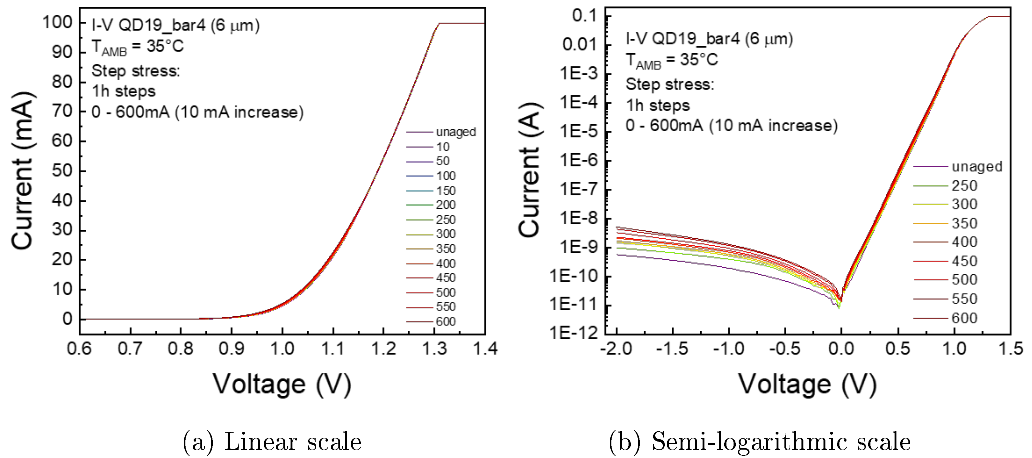

(a) Linear scale

(b) Semi-logarithmic scale

Figure 5.4: I-V characteristic as a function of the stress-time, at different currents (not all the steps are shown for clarity).

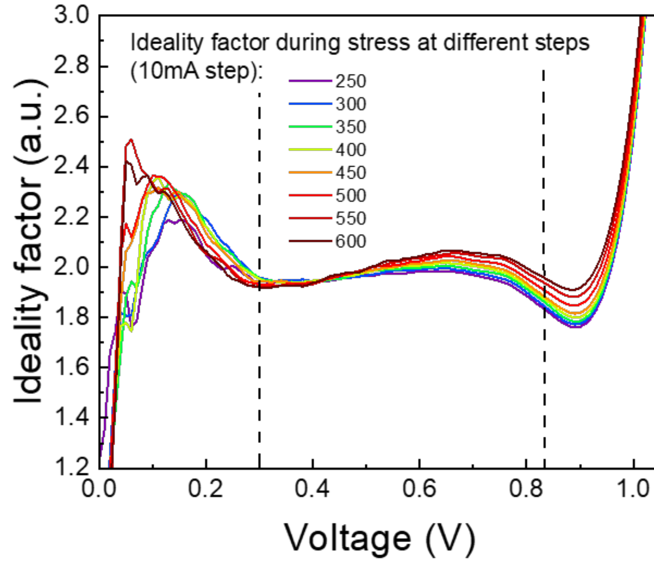

(a) During stress.

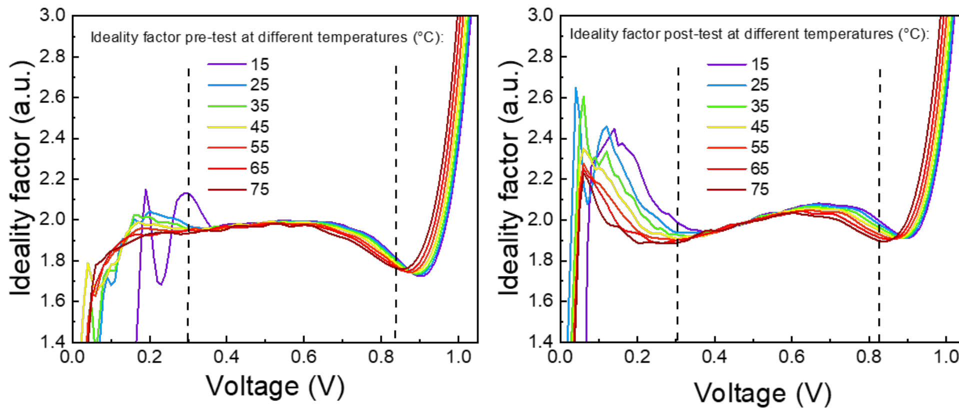

(b) Before-stress.

(c) After-stress.

Figure 5.5: Ideality factor extracted during the (a) step stress experiment, (b) pre-stress and (c) post-stress characterization.

Electroluminescence measurements were useful to understand the different emission dynamics and to relate them with the degradation processes. The wide-span spectra result is shown in Figure 5.6(a). The curves have been smoothed for a better readability. It must be noted that, when performing wide-span spectral acquisitions, the fiber response changes significantly,. The correction was performed by means of the point-wise multiplication between the optical power (in linear scale) and the fiber attenuation. In addition,

we had to take into account the spectral response of the photodetector. Similarly as for the fiber attenuation, we corrected the optical power values by multiplying the linear spectra by the photodetector responsivity, for each wavelength value. The increase of injected current causes a red-shift of the spectrum due to self-heating as a consequence of bandgap narrowing, in the case of QDs.
Figures 5.6(b),(c) and (d) better show the device emission in three different regimes: ground state (GS) emission only, both ground state and excited state emission (GS + ES), excited state (ES) emission only.

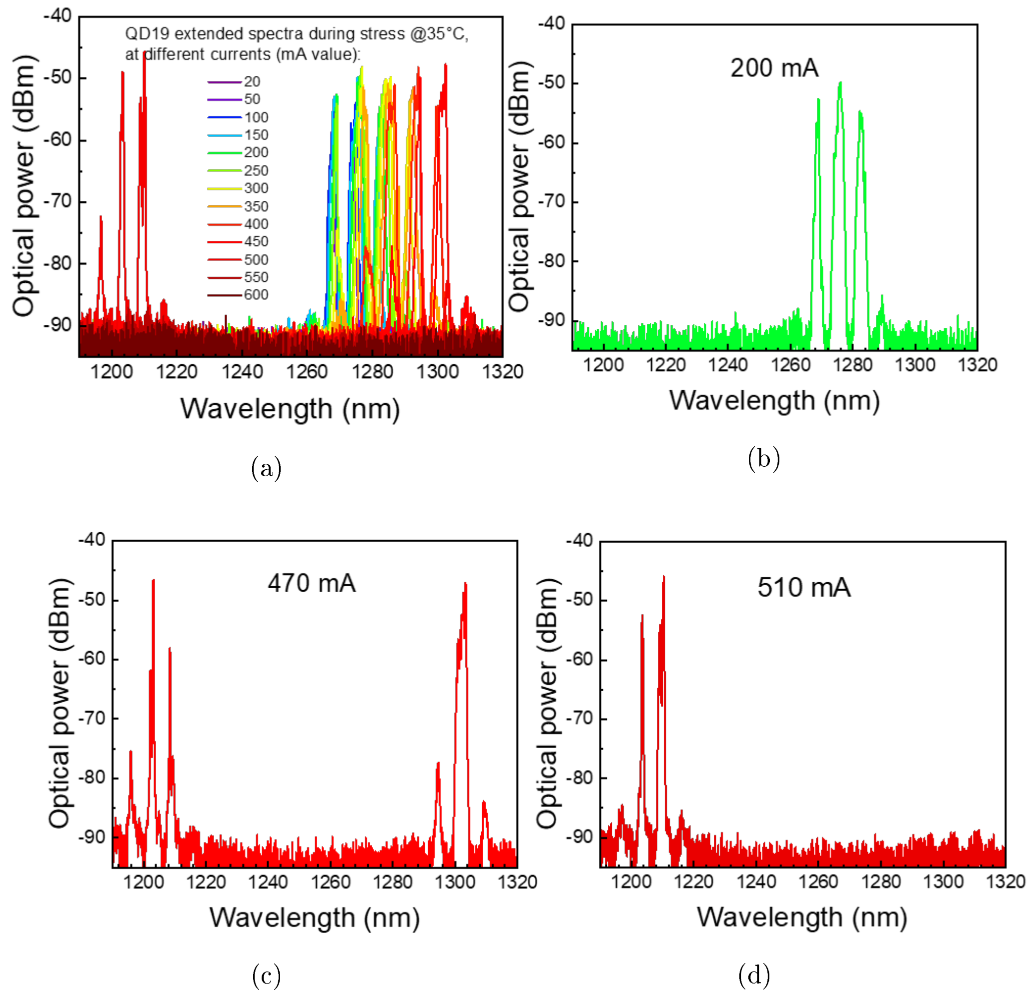

Figure 5.6: EL spectra (a) at increasing currents during the stress and (b), (c), (d) at three different current levels, corresponding to (b) ground state emission,(c) both ground state and excited state and (d) excited state emission.

The integral of GS and ES emission, in Figure 5.7 better helps to understand the emission dynamics. The onset of GS emission is followed by a monotonically increase of the emission from 30 mA to 340 mA. From 340 mA to 450 mA the emission shows a decrease in the GS emission, and carriers start to populate the ES. At 450 mA the ES starts lasing and from there to 500 mA both GS and ES are emitting, with a decrease in GS and an increase in ES. After 550 mA the device stops lasing, suggesting that a large portion of carriers is escaping from the active layers to recombine non-radiatively through defects, dislocations and other layers. This behavior can be explained with the two-state lasing and GS-quenching phenomenons analyzed, in Chapter 2: when GS starts lasing, the carrier density will be clamped and additional carriers will start filling the ES; when ES reaches its current threshold level it starts lasing as well, making two-state lasing possible (Figure 5.6(c) clearly shows that). GS-quenching can happen for factors: (a) at high current levels, the difference in carrier occupation probability disappears and, since ES has a higher degeneracy than GS, ES will be the only one lasing; (b) self-assembled quantum dots show homogeneous broadening of the optical gain as well as retarded carrier relaxation into the quantum-dot discrete energy states [88]; (c) hole injection is low at higher currents: in this bias regime, the carrier population of in the GS is clamped and, since the GS and ES levels for holes are very close, holes are shared between the electrons of the GS and ES, thus leading to their consumption only by ES due to its higher degeneracy (that can be seen as the reduction of the radiative lifetime associated to it).

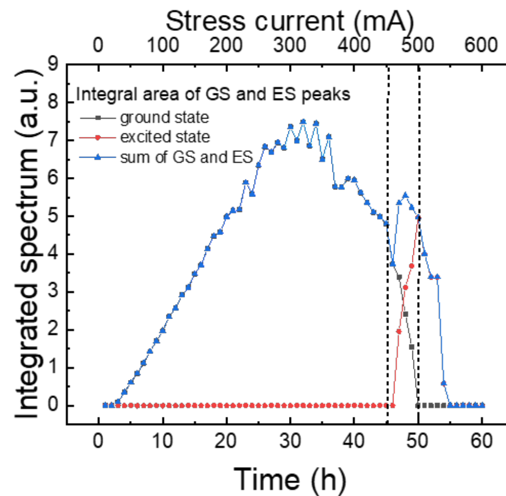

Figure 5.7: Variation of the integrated spectrum with increasing stress current and stress time. The GS, ES and their sum are plotted for comparison.

During the entire stress experiment, the device voltage and the output voltage of the photodetector were constantly monitored by the source meter. These two data sets are plotted as a function of the stress-time in Figure 5.8. The voltage clearly follows the I-V exponential relation of a typical diode; the initial drop is due to the self-heating of the device. The optical power follows the integrated spectrum trend of Figure 5.7, further confirming how the laser emission evolves with increasing current: it involves GS until it reaches two-state lasing and ultimately ES only emission, ending with a complete quenching of the elecroluminescence of the device. In particular, starting from 340 mA, but in a more pronounced way after 450 mA, carrier escape cannot be negligible: carrier escape and degradation are linked, in the sense that once electrons/holes escape from the WL, they can reach dislocations and extended defects and, hence, recombining non-radiatively. This can enhance the propagation of defects near the active layers and cause an increase in the degradation rate of the device.

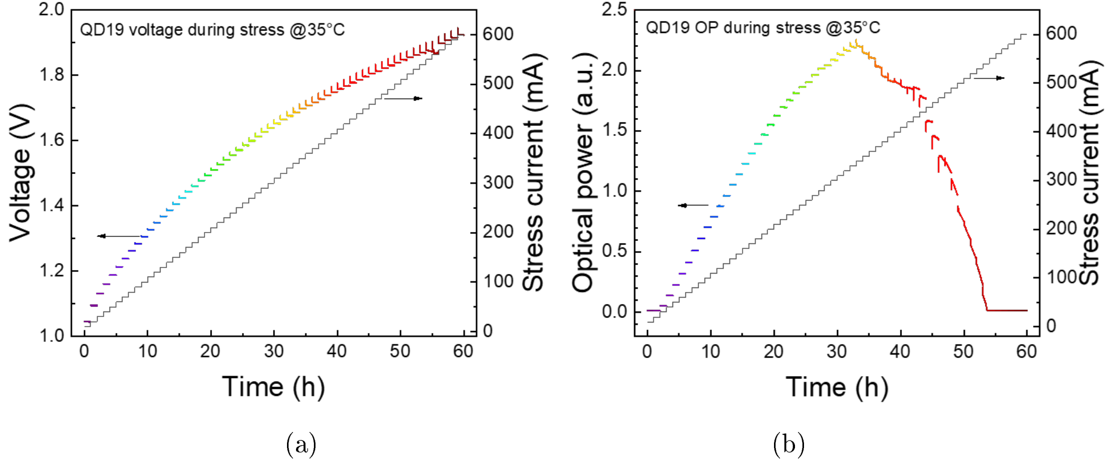

(a) (b)

Figure 5.8: (a) Device voltage and (b) optical output power measured during the step-stress experiment.

The spectral characterization performed between each stress-step is shown in Figure 5.9 In order to make the graphs easier to understand, a locally estimated scatter plot smoothing (LOESS) has been performed on the dataset. First of all, it is clear that the optical spectrum is composed of two distinct peaks centered at $\lambda_1 = 1268\ nm$ and $\lambda_2 = 1274\ nm$. This could be the result of different interactions, such as absorption and stimulation mechanisms, of ensembles of various properties. The estimated energy level for the corresponding wavelengths are $E_{g1} = 0.977\ eV$ and $E_{g2} = 0.973\ eV$. Especially for the last two measurements (55 mA and 65 mA), it can be seen that the optical power drop occurs mainly in the low-energy peak, while

the high-energy region seems to be less affected by the degradation process. This observations suggest a significant carrier escape, as the most energetic carriers are more likely to leave the quantum-dots and reach the surrounding quantum-well.

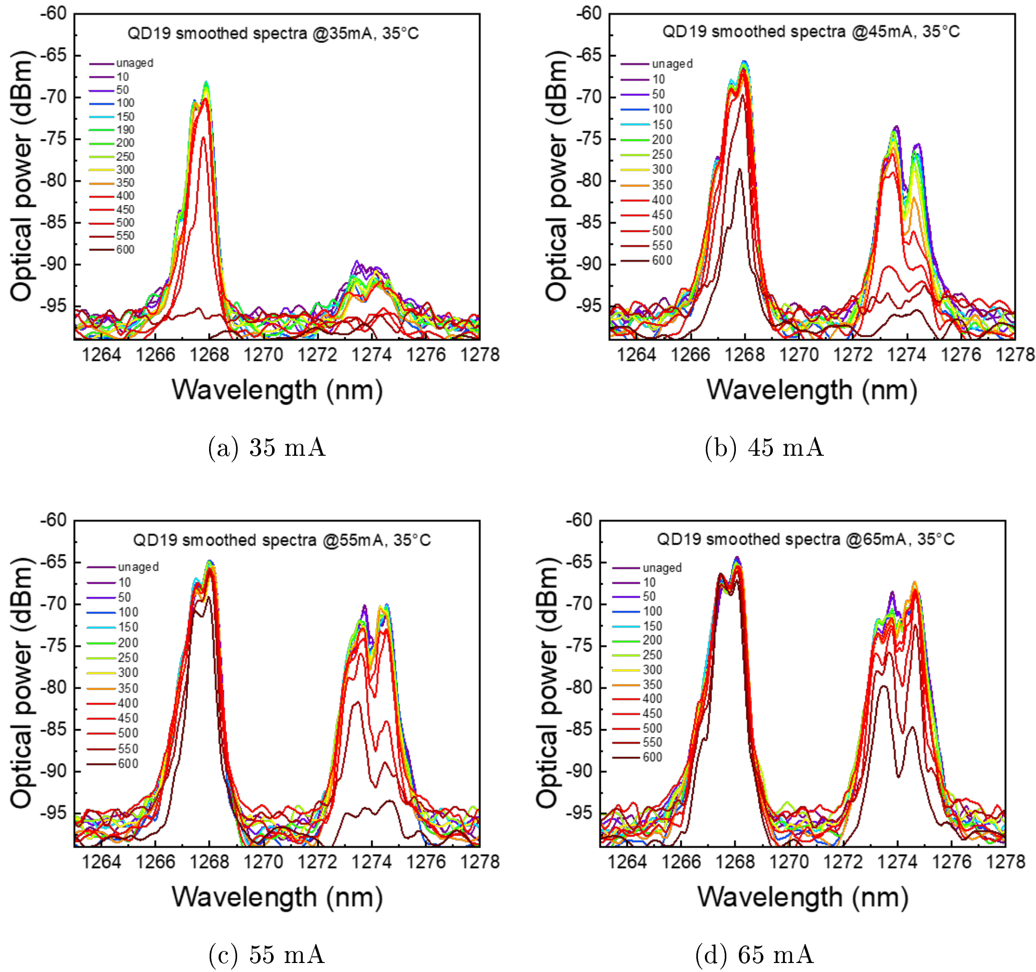

(a) 35 mA

(b) 45 mA

(c) 55 mA

(d) 65 mA

Figure 5.9: Characterization spectra of device QD19 at four different currents. The spectra shown are smoothed.

Laser characteristics before and after stress

For the characteristics before and after stress, the temperature was varied from 15°C to 75°C, with a step of 10°C, performing I-V, L-I and spectral measurements at fixed currents.
The L-I curves, as a function of the temperature, are shown in Figure 5.10.

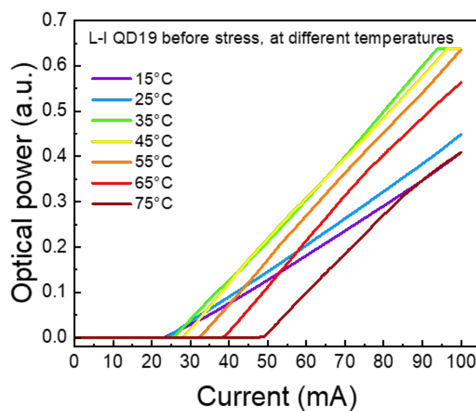

(a) Before stress, linear scale.

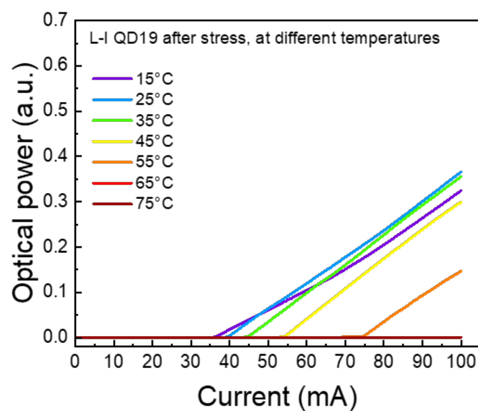

(b) After stress, linear scale.

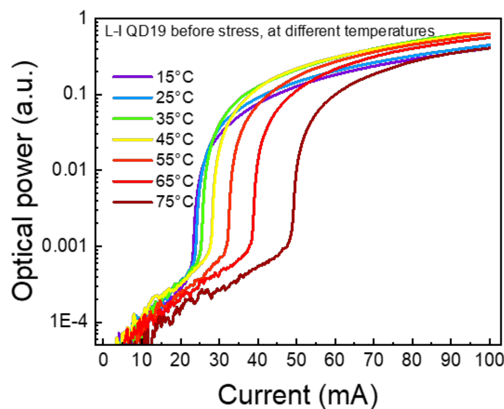

(c) Before stress, semi-logarithmic scale.

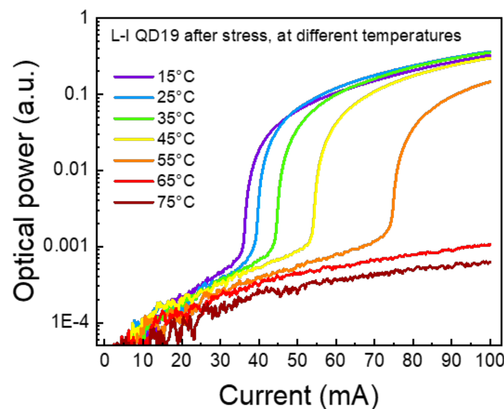

(d) After stress, semi-logarithmic scale.

Figure 5.10: L-I characteristics as a function of temperature, both beforeand after-stress.

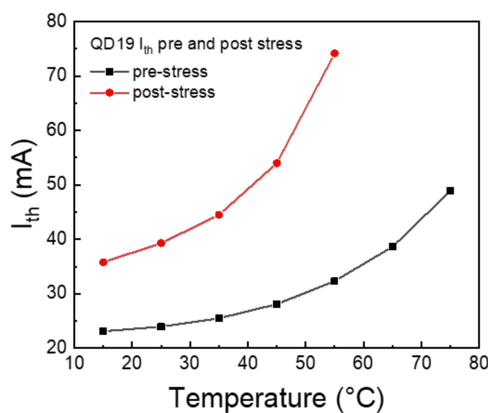

(a) Absolute value.

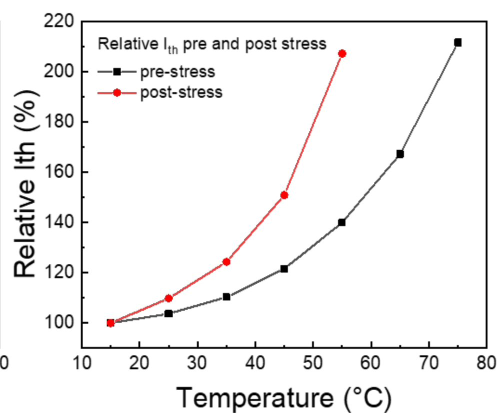

(b) Relative value.

Figure 5.11: Threshold current versus temperature, before- and after-stress.

The stress degraded the sample to the point that it no longer emitted stimulated radiation above 75°C; however, a general emission worsening can be noticed. From these, the threshold current-temperature relation, both before- and after-stress, is presented in Figure 5.11 in absolute and relative values.
The stress induced a general increase in the threshold current, with a stronger variation for higher temperatures. This may be ascribed to carrier escape from the quantum dots or to increase in non-radiative recombination caused by an increase of the defect concentration in the active layer as a consequence of the aging experiment.

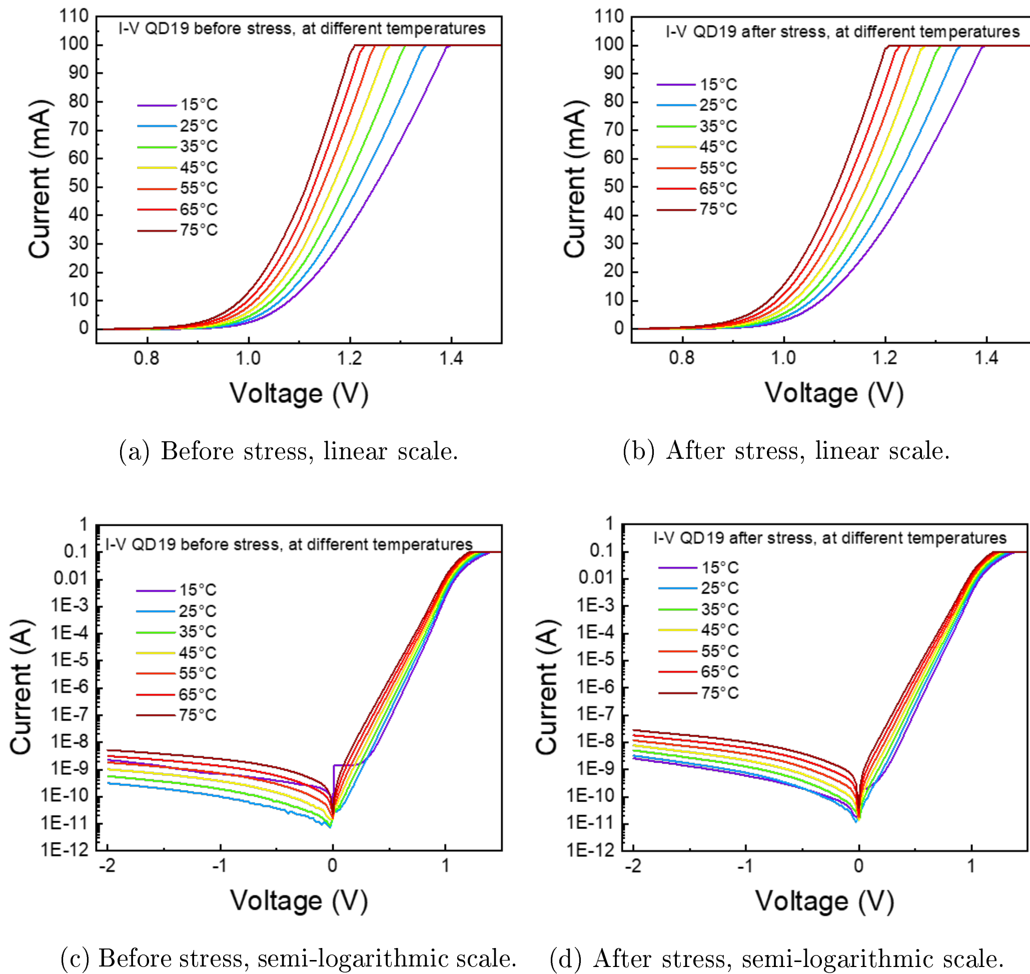

(a) Before stress, linear scale.

(b) After stress, linear scale.

(c) Before stress, semi-logarithmic scale.

(d) After stress, semi-logarithmic scale.

Figure 5.12: I-V characteristics as a function of temperature, both before and after-stress.

The I-V curves, both before and after stress are presented in Figure 5.12,

as a function of temperature. The curves do not show significant changes. The anomalous trend of the curve at 15°C can be explained by the formation of a small leakage path on the device.
Finally, the spectra taken at fixed currents are shown in Figure 5.13. Only the most significative curves at 25°C and 45° are presented. As expected, a general decrease in the optical power emission can be noted, with the disappearance of the secondary peaks.

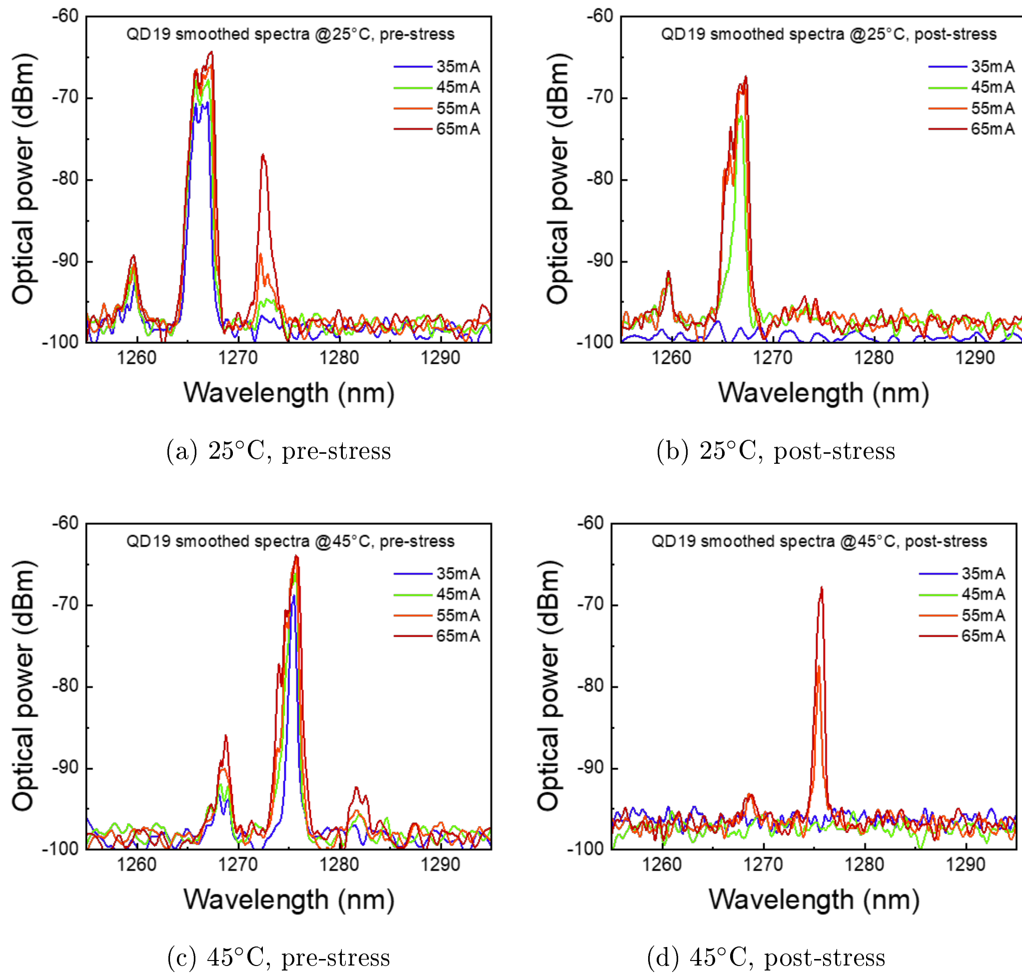

(a) 25°C, pre-stress

(b) 25°C, post-stress

(c) 45°C, pre-stress

(d) 45°C, post-stress

Figure 5.13: I-V characteristics as a function of temperature, both before and after-stress.

5.2 Current-step stress: GaAs-substrate and Si-substrate comparison

In the following section, a comparison between a silicon-substrate device from the "Bar3" lasers and a native-substrate device from the "Die2 Bar4" lasers is discussed. Both devices were submitted to a step-stress experiment with the following conditions:

- stress temperature of 35°C,
- stress current from 20 mA to 840 mA, with 20 mA increase every hour.

The only differences concern the currents chosen for the characterization spectra and the current sweep values during the L-I measurements, to avoid unnecessary stress and self-heating of the different DUTs:

- bias current equal to 20, 40, 60, 80, 100, 120 mA were chosen for the spectral characterization of the native-substrate device,
- bias current equal to 30, 50, 70, 90, 110 mA where chosen for the spectral characterization of the silicon-substrate device,
- Current sweep from 0 to 150 mA for the native-substrate device and from 0 to 100 mA for the silicon-substrate device.

The most significative results are discussed below.

Characterization pre-stress

From the characterization before-stress, the effect of the different temperature dependence due to different substrate must be highlighted. The L-I curves as a function of temperature of the unaged devices, in Figure 5.14, show how the absence or presence of dislocations, due to the absence or presence of lattice mismatch with a native and non-native substrate respectively, can impact on the optical efficiency of the devices. In particular, the L-I curves of the GaAs-substrate device (Fig. 5.14(a)) show no shift with increasing current, indicating that a high portion of carriers recombines radiatively and is not lost due to leakage paths that can be caused by impurities. Also, the stability of the curve with increasing temperature suggests that the carrier escape and overflow have a different impact on the lasers: carrier capture could also be improved by the two SCH additional layers in the epitaxial structure of the GaAs-substrate device, that can also contain carriers in high injection conditions. A further confirmation can be found plotting the I_{th} vs T and SE vs T curves, for both devices, as shown in Figure 5.15 in relative scales.

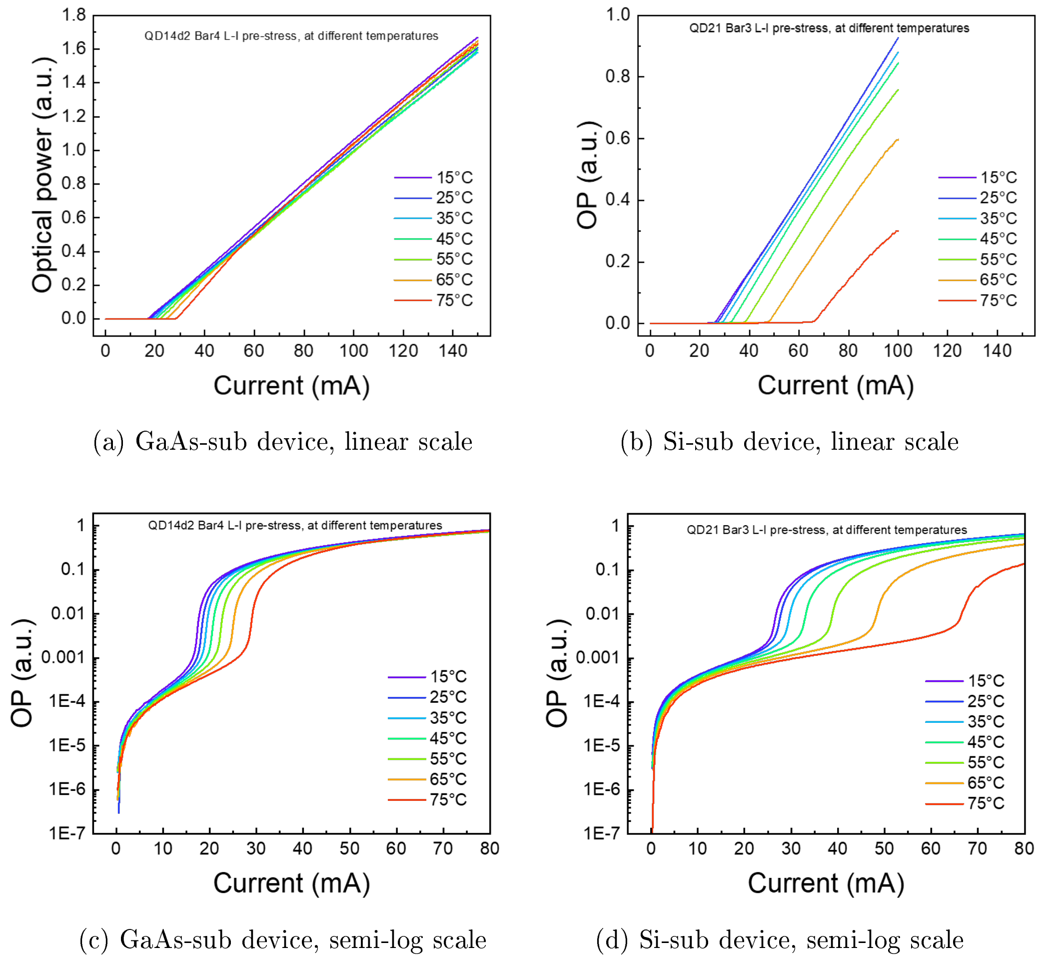

(a) GaAs-sub device, linear scale

(b) Si-sub device, linear scale

(c) GaAs-sub device, semi-log scale

(d) Si-sub device, semi-log scale

Figure 5.14: L-I characteristics as a function of temperature, before-stress.

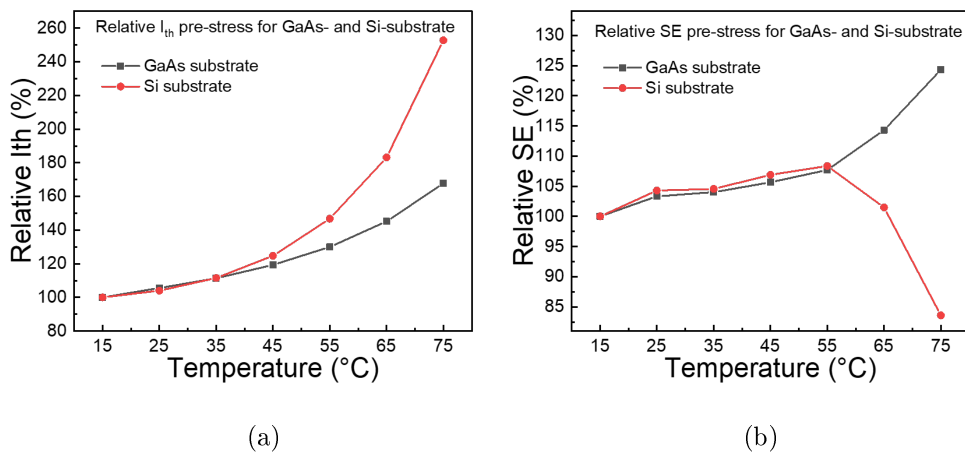

(a)

(b)

Figure 5.15: Relative (a) threshold current and (b) slope efficiency with varying temperatures for both GaAs- and Si-substrate devices.

The threshold current and the optical efficiency variation in temperature are stronger for the Si-substrate laser above 55°C, indicating an increase in carrier losses. Interestingly, the silicon-substrate device shows an increase in SE, maybe suggesting higher carrier injection. Afterwards, non-radiative mechanisms like SRH recombination start dominating.
Figure 5.16 compares the spectra at three different temperatures, for the two devices at two similar currents. The characterization spectra at different temperatures shows, for a given current, an interesting behavior of the native-substrate DUT: in Figures 5.16(a) and (c) the disappearance of the right shoulder of the spectrum, from 25°C to 75°C, corresponds to a drop for the low-energy side of the emission. In addition, a narrowing of the spectrum is found. These observations, together with the increased I_{th} and SE values for higher temperatures that can be seen in Figure 5.15, might suggest that, with increasing temperature, the subset of QDs responsible for the low-energy emission cannot reach the threshold population inversion necessary to emit.
The electrical characterization shows a similar behavior with varying temperature, as shown in Figure 5.17. A comparison between two curves at the same temperature is presented in Figure 5.18. The GaAs-substrate device shows a higher series resistance that can be originated from the higher number of layers, different doping levels or from the annealing of the ohmic contacts. Moreover, the devices show differences in low-forward bias condition.

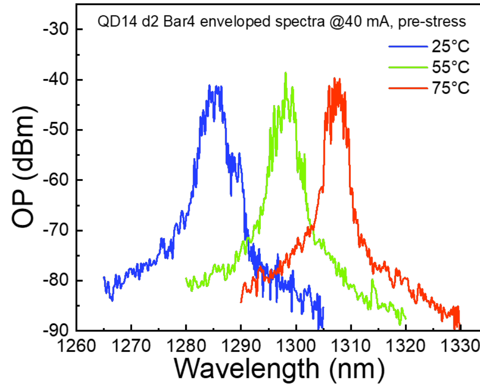

(a) GaAs-substrate device, 40 mA

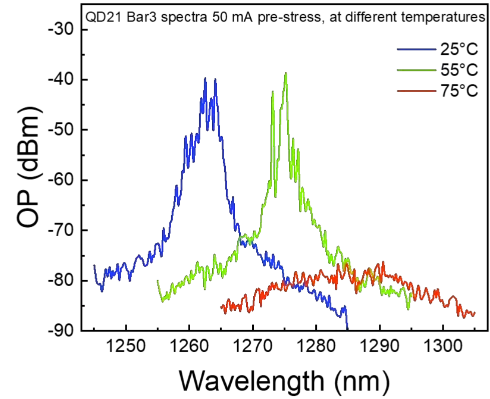

(b) Si-substrate device, 50 mA

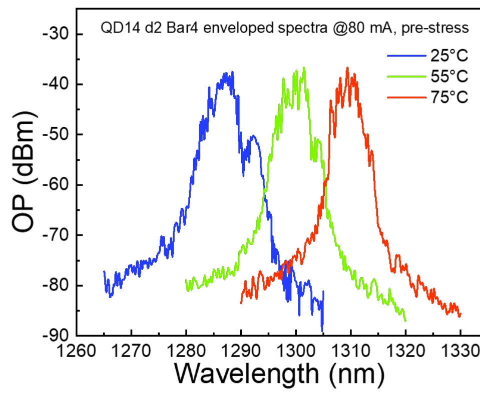

(c) GaAs-substrate device, 80 mA

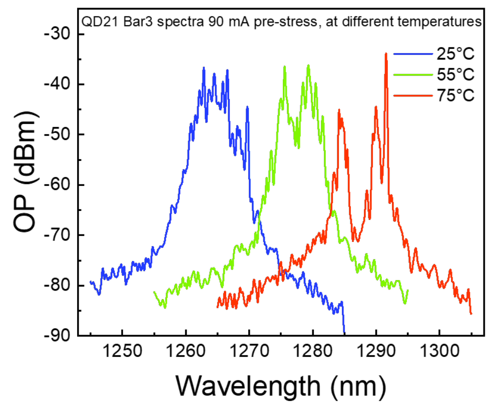

(d) Si-substrate device, 90 mA

Figure 5.16: Characterization spectra at 25°C, 55°C and 75°C, for (a), (c) GaAs-substrate and (b), (d) Si-substrate devices.

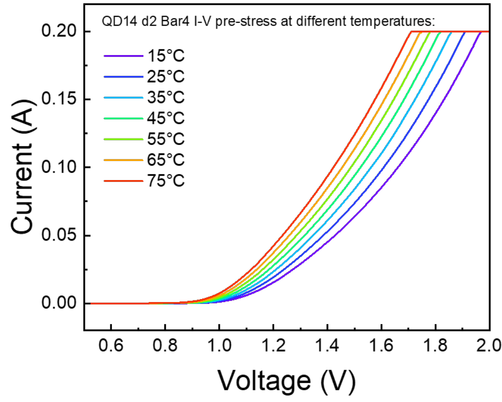

(a) GaAs-substrate, linear scale

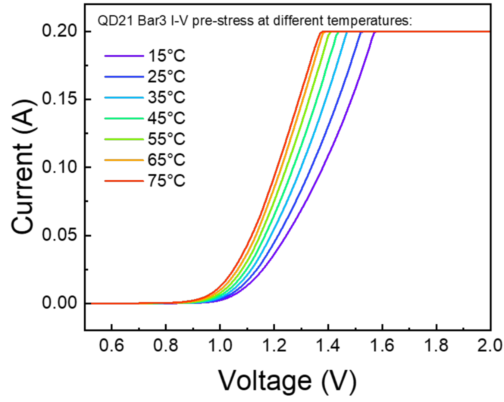

(b) Si-substrate device, linear scale

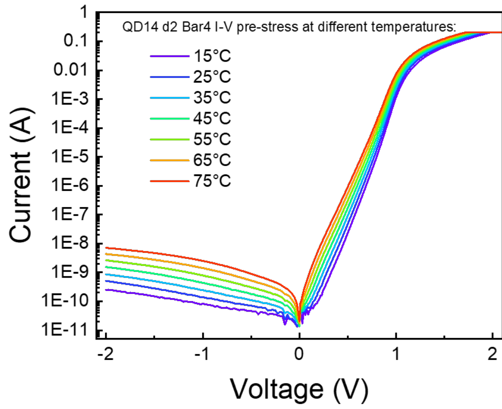

(c) GaAs-substrate device, semi-log scale

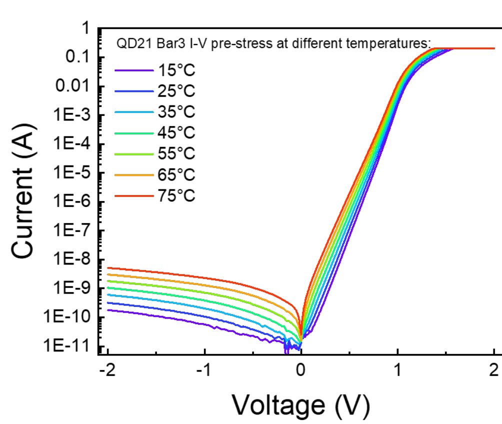

(d) Si-substrate device, semi-log

Figure 5.17: I-V characterization as a function of temperature.

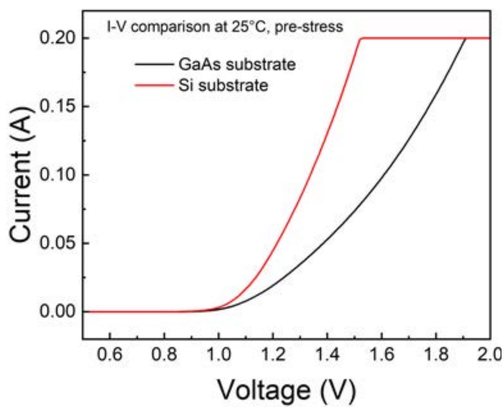

(a)

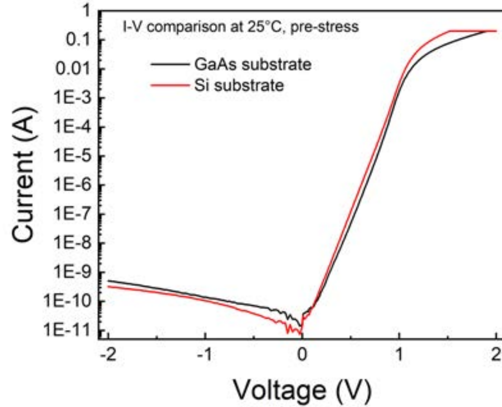

(b)

Figure 5.18: I-V characteristics in (a) linear scale and (b) semi-logarithmic scale, for GaAs- and Si-substrate devices.

Step-stress experiments

The step-stress experiments highlight other differences: the L-I curves during stress, reported in Figure 5.19, show how the degradation affects the devices in different ways. In particular, Fig. 5.19(a) shows an unexpected impact of the degradation on the optical characteristics of the GaAs-substrate laser. The onset of a stronger degradation can be noted at 520 mA, followed by a slowdown at 600 mA. The Si-substrate device, in Fig. 5.19(b), after 380 mA presents a stronger curve right-shift, towards higher threshold currents, indicating that the degradation rate of the device is increasing.
The I_{th} and SE curves, extrapolated from the L-I characteristics, are shown in Figure 5.20, in absolute and/or relative scales.
Fig. 5.20(b) displays that for low-current values the GaAs-substrate device seems to behave better than the Si-substrate device. However, once the degradation mechanisms arise, the GaAs-substrate I_{th} value grows enormously, reaching the 370% of its initial value at 840 mA and showing a plateau around 680 mA. The ES onset, GS and ES turn-off are (Figure 5.21):

- ES onset: 400 mA for the GaAs-substrate device, 380 mA for the Si-substrate device,
- GS quenching: 440 mA for the GaAs-substrate device, 400 mA for the Si-substrate device,
- ES turn-off: 620 mA for the GaAs-substrate device, 520 mA for the Si-substrate device.

The GaAs-substrate device behaves better before its own ES emission turn-off. The threshold current of the Si-substrate device starts increasing after the ES onset. Fig. 5.20(c) and (d) show the slope efficiency trend, taken at different ranges, that shows a decrease in correspondence of the onsets of stronger degradation at 520 mA for the GaAs-substrate device and 380 mA for the silicon-substrate device.
The intermediate acceleration in the degradation process could be ascribed to the excessive self-heating generated into the GaAs-substrate laser, due to the lower conductivity of the substrate material (0.455 $W(cm\ K)^{-1}$ for GaAs vs 1.412 $W(cm\ K)^{-1}$ for silicon), to the fact that the GaAs-substrate is thicker.
The relationships between I_{th} and 1/SE are shown in Figure 5.22.

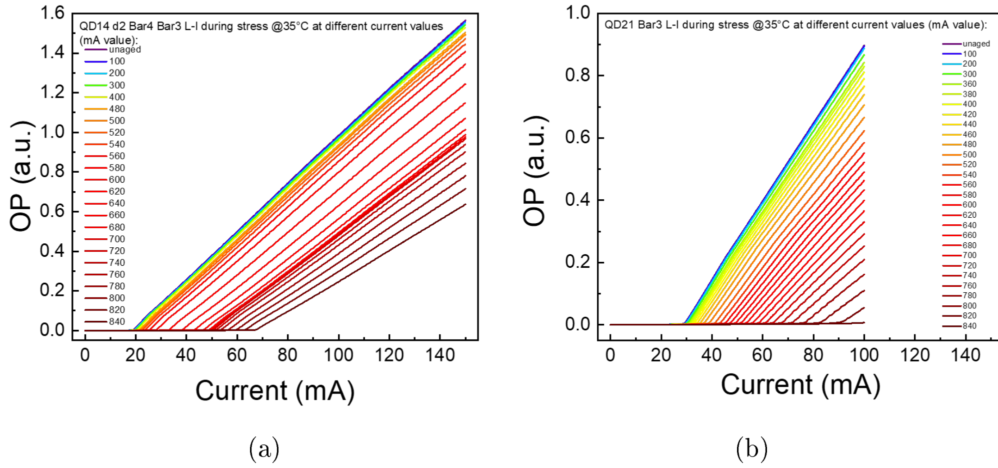

(a) (b)

Figure 5.19: L-I characteristics during stress for (a) GaAs-substrate and (b) Si-substrate devices.

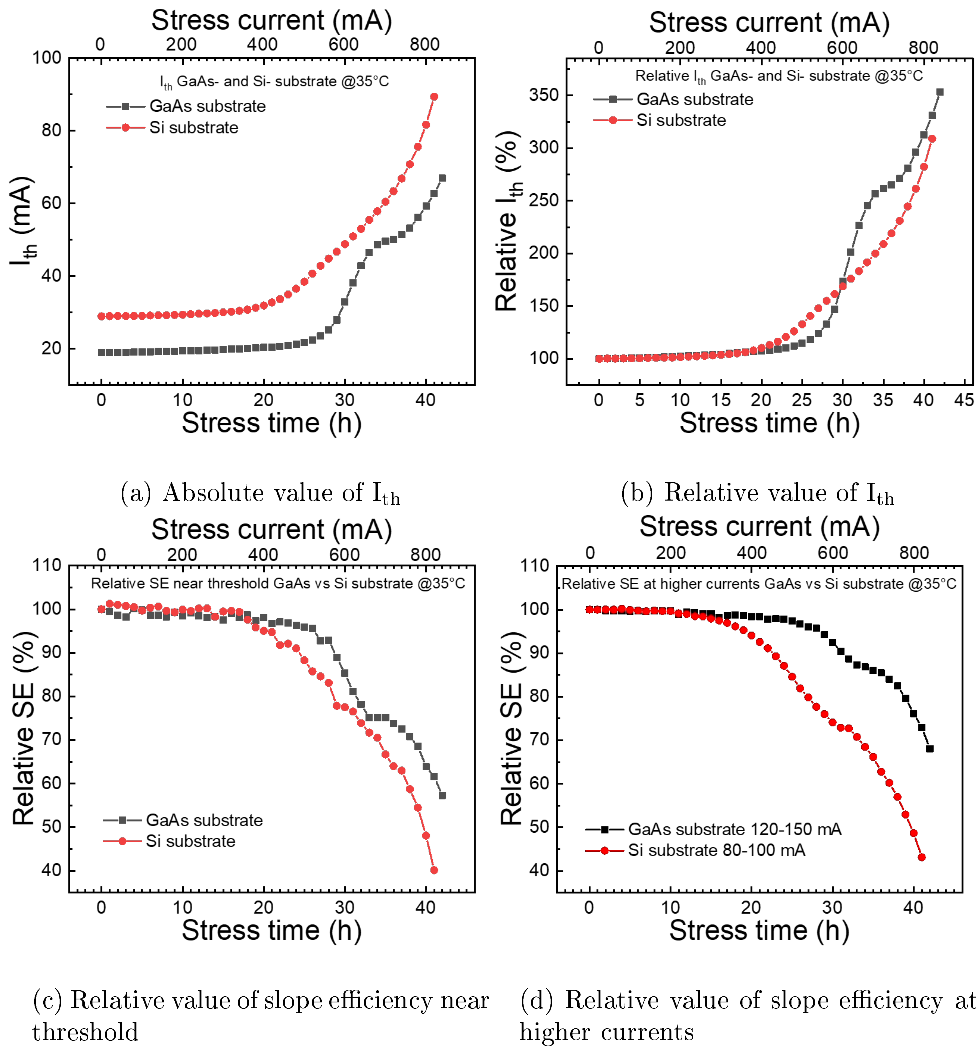

(a) Absolute value of I_{th}

(b) Relative value of I_{th}

(c) Relative value of slope efficiency near threshold

(d) Relative value of slope efficiency at higher currents

Figure 5.20: I_{th} and SE trends as a function of stress time and current.

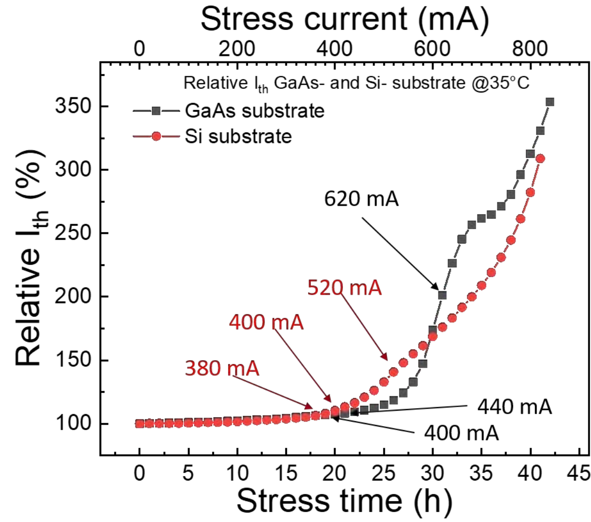

Figure 5.21: Relative I_{th} trend for GaAs- and Si-substrate devices, displaying excited-state onset and turn-off.

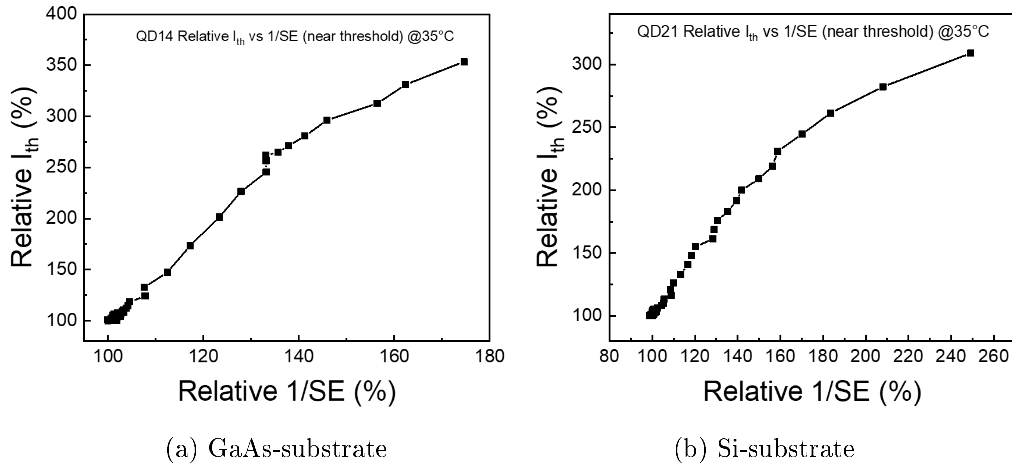

(a) GaAs-substrate

(b) Si-substrate

Figure 5.22: I_{th} vs 1/SE trend.

For the GaAs-substrate device, the curve presents a different slope for $I_{STRESS} > 680$ mA, that could suggest that a different degradation mechanism is affecting the DUT. The correlation is lost in the last current steps for the Silicon-substrate device.
In these two experiments, extended L-I measurements were performed right after the usual L-I characterization, in order to observe the thermal roll-off of the optical power of the devices. The sweep range was increased at every

step, following the ongoing current-stress value. The results are plotted in Figure 5.23, with the dashed lines that correspond to the thermal roll-off of the GS and ES emission (left and right line of each graph, respectively).

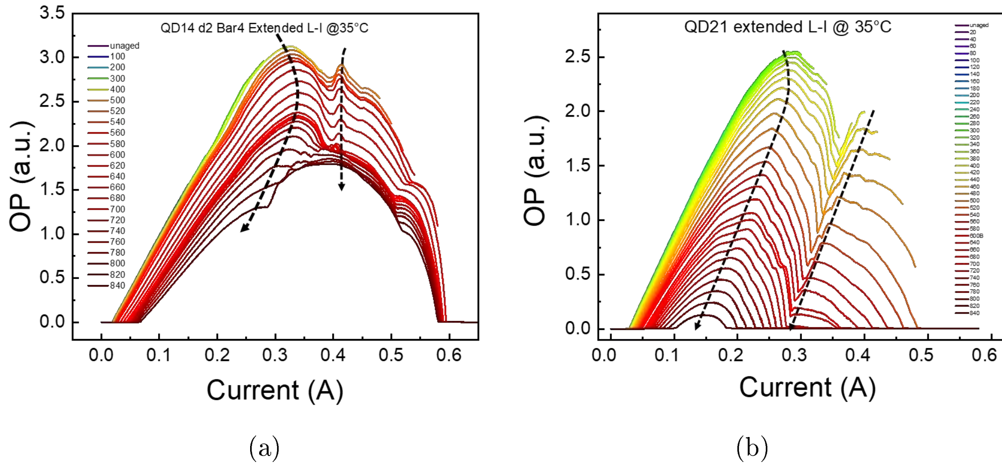

(a) (b)

Figure 5.23: Extended L-I characteristics during stress for (a) GaAs-substrate and (b) Si-substrate devices.

Figure 5.23(a) interestingly shows change in correspondence of 550 mA, that could be a possible different mode emission or the presence of the excited-state 2 emission, as it is hypothesized later.
The EL spectra during the stress, taken after 25 minutes of each step are reported in Figure 5.25. Interestingly, the silicon-substrate device exhibits, right from the start, three bumps. The result of the corresponding energy level of those emission can explain the origin of those bumps, as Figure 5.24 shows.
The two highest peaks correspond to the GS and ES emission, as demonstrated from the band diagram on the right portion of Figure 5.24. The lower peak, with an emission energy of 1.14 eV, is still localized inside the QD, thus it can represent the so-called *excited state 2*, that ultimately is the third lower peak that arises in Figure 5.25, around 1100 nm.

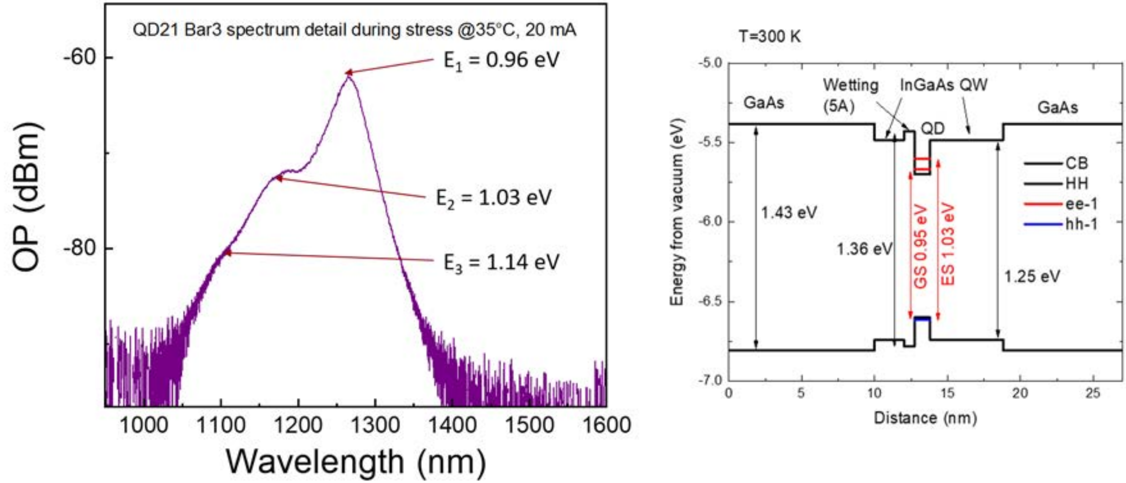

Figure 5.24: Origin of bumps, related to possible band-to-band emissions.

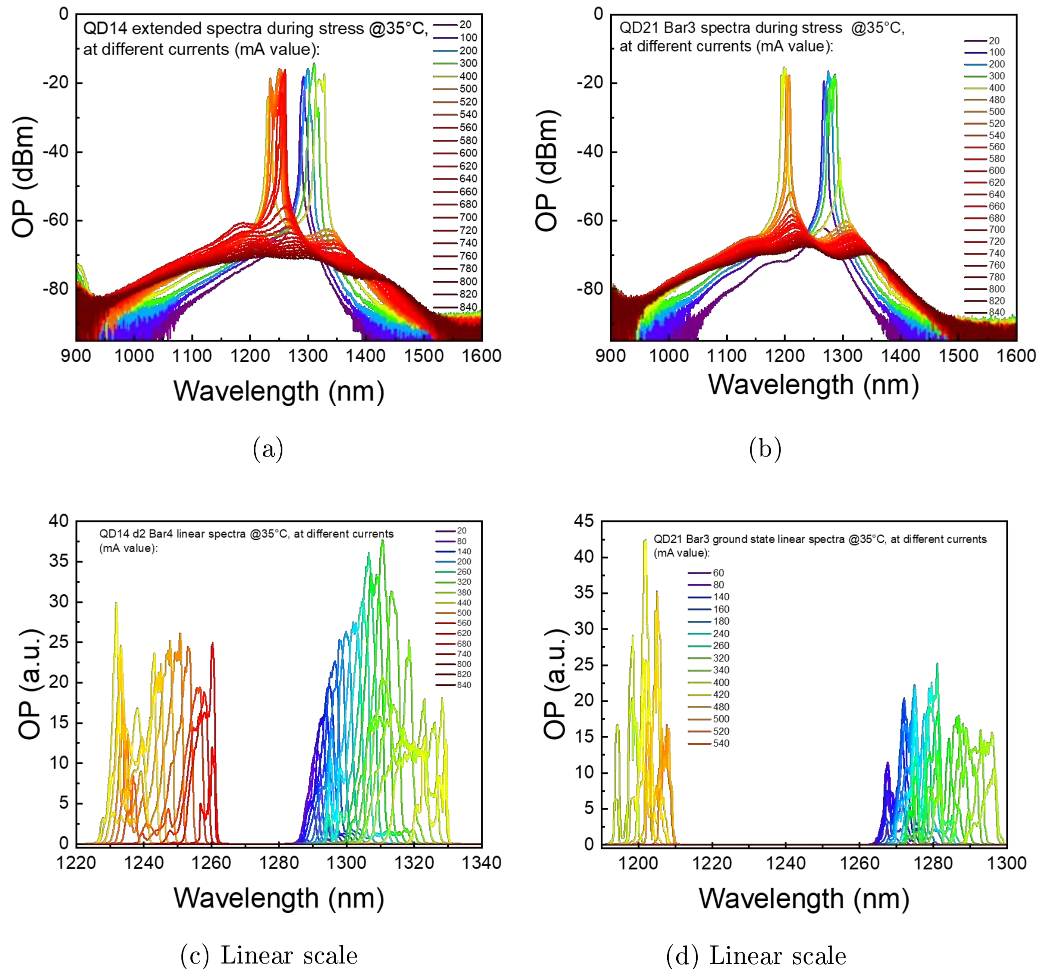

(c) Linear scale

(d) Linear scale

Figure 5.25: Spectra taken after 25 minutes of each step for (a),(c) GaAs-substrate device and (b),(d) Si-substrate.

As previously seen in the first step-stress experiment description, two-state lasing is present and GS quenching occurs with increasing currents. Both graphs show a first jump of the spectra emission, from 20 mA to 40 mA, representing the operating regime reached by the laser; in particular, the silicon-substrate device does not even crosses its threshold condition at 20 mA, since I_{th} is around 30 mA, as already seen in Figure 5.20(a). A second jump of the emission spectra can be observed at 600 mA for the GaAs-substrate device and 520 mA for the silicon-substrate device: this second phenomenon needs to be further investigated; however, one hypothesis might be related to carrier spreading into other semiconductor layers, that could justify the overall high-energy emission increase and be related to the excited state 2 emission. The low-energy portion of the spectra should always be linked to the emission from QDs. The integrals of the spectra, shown in Figure 5.26, suggest how degradation differently affects the two devices.

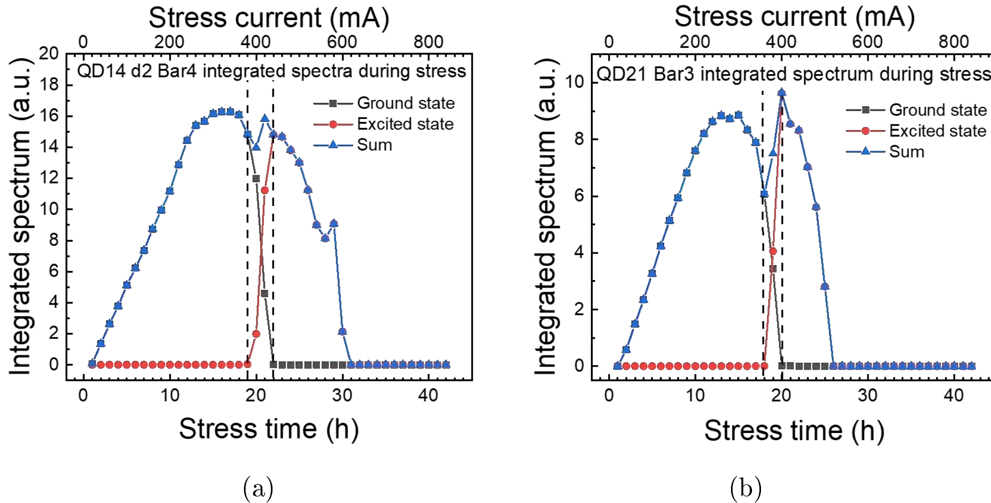

Figure 5.26: Integrated spectrum of (a) GaAs-substrate and (b) Si-substrate laser emission. Dashed lines distinguish between the three emission regimes: GS only, GS+ES and ES only.

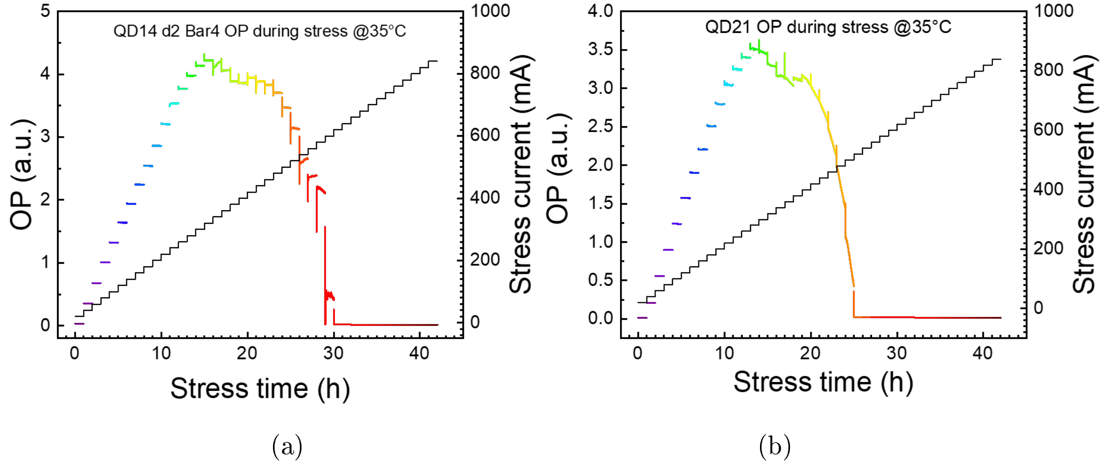

(a) (b)

Figure 5.27: Optical power as a function of stress time and stress current for (a) GaAs-substrate device and (b) Si-substrate device.

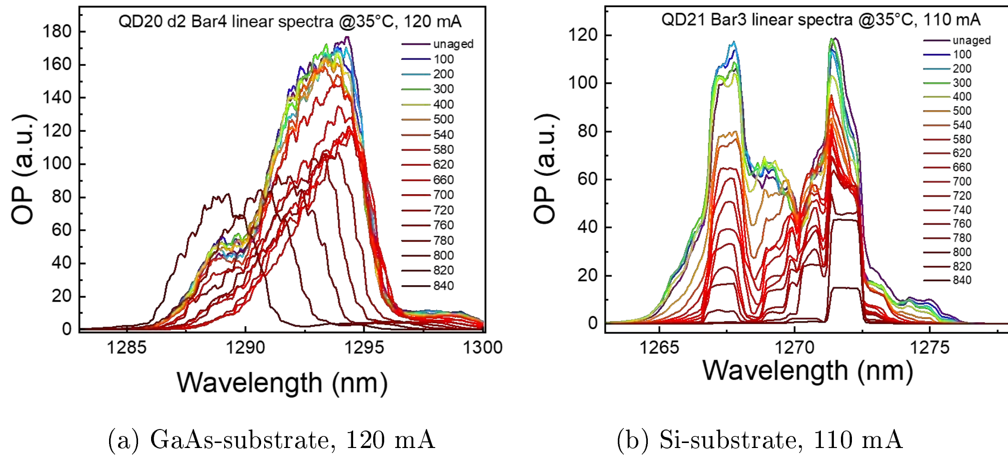

(a) GaAs-substrate, 120 mA (b) Si-substrate, 110 mA

Figure 5.28: Linear characterization spectra during stress.

Both devices exhibit the three regimes previously mentioned: GS emission only, both GS and ES emission and ES emission only. However, the silicon-substrate laser shows a faster degradation, with absence of emission from 520 mA. This can also be seen from the optical power versus stress time plot in Figure 5.27. As soon as the ES emission is fully reached (420 mA for the GaAs-substrate device and 400 mA for the silicon-substrate device) there is a significant drop in optical efficiency: carrier escape and overflow become dominant and population inversion, necessary for the laser emission, decreases. This phenomenon appears to be less rapid for the GaAs-substrate device, possibly due to the larger active region and the two additional con-

fining layer, that help reducing the escape rate.
The characterization spectra during the experiments, taken at fixed current values show unexpected results for the GaAs-substrate. Figure 5.28 reports the most significative example, at 120 mA and 110 mA for the GaAs-substrate and Si-substrate devices, respecitvely. It is immediate to see how the spectra in Figure 5.28(a) changes with increasing current: a drop at the high-energy side of the emission takes place for $I_{STRESS} < 680$ mA; this reduction in short-wavelength emission can be caused by a decrease in gain related to an ensemble of QDs. Then, an unexpected shift towards high-energy emission takes place: this phenomenon, in combination with the shift shown in the spectra taken during stress, could suggest a progressive reduction of the QDs dimension, due to damages to the material edges.
Regarding the electrical properties variation during the stress, the I-V characteristics are plotted in Figure 5.30. The excessive self-heating of the device could be the cause of the I-V trend in Fig. 5.30(a), showing an increase in the series resistance (Fig. 5.31) and a decrease in the diode cut-in voltage. Regarding Fig. 5.30(b) and (c), both devices show an increase in the reverse leakage current, ascribed to defect-related conduction paths.
The GaAs-substrate DUT also shows a bigger series resistance, as it can be noted from the different slope of Fig. 5.30(a) and (b). Its different effect can be observed from the operating voltage during the stress experiments, in Figure 5.29. A higher series resistance can increase the self-heating of the device.

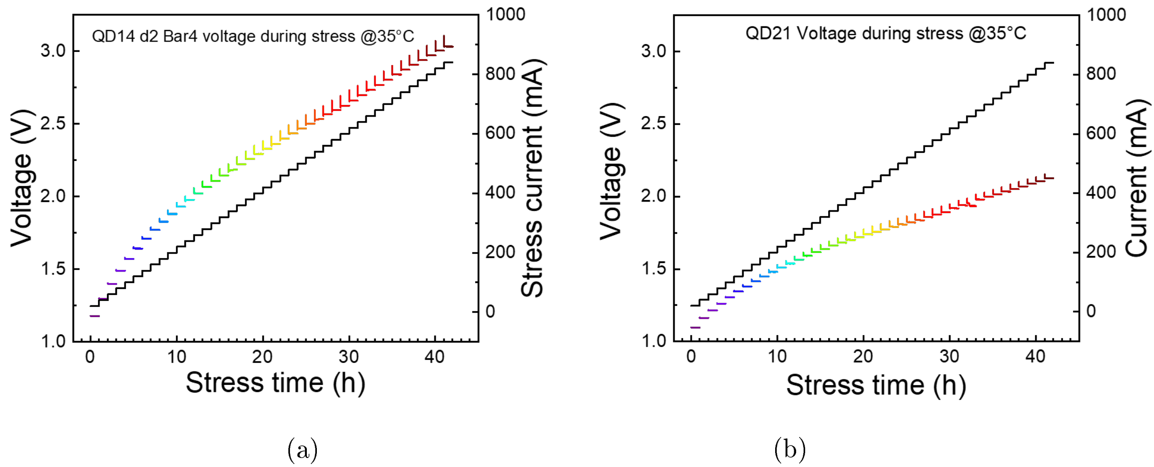

(a) (b)

Figure 5.29: Operating voltage as a function of stress time and stress current for (a) GaAs-substrate device and (b) Si-substrate device.

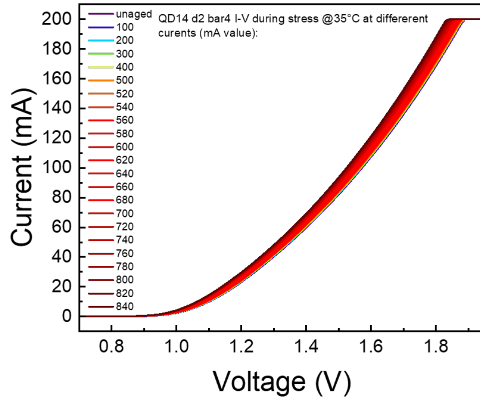

(a) GaAs-substrate, linear scale

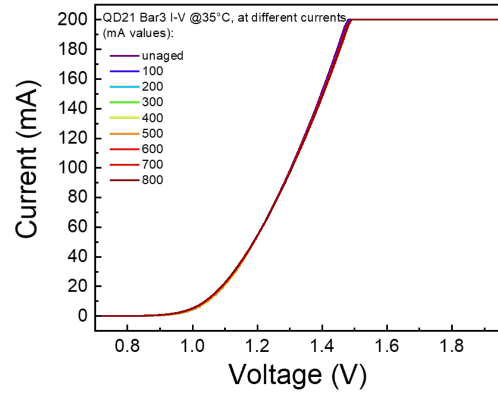

(b) Si-substrate, linear scale

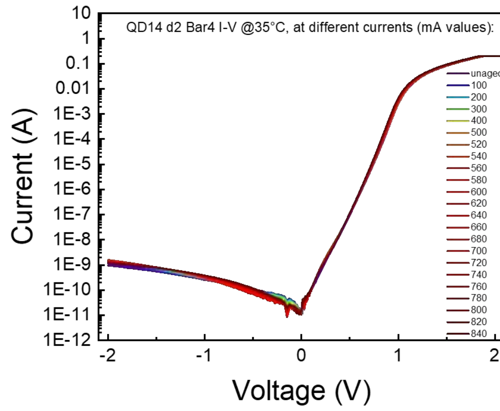

(c) GaAs-substrate, semi-logarithmic scale

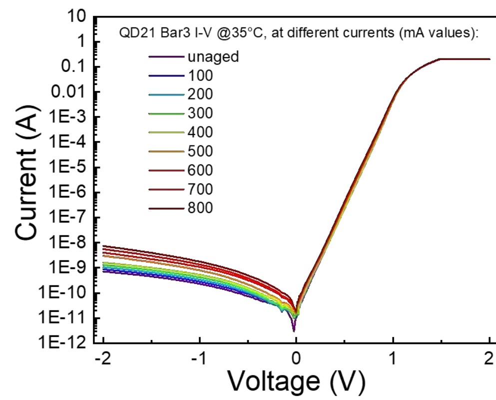

(d) Si-substrate, semi-logarithmic scale

Figure 5.30: I-V characteristics during stress.

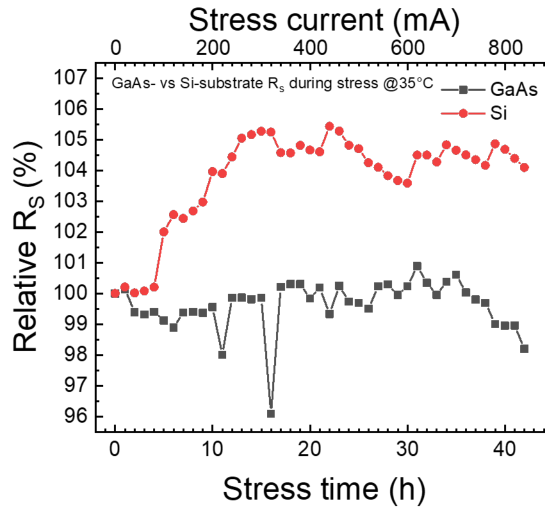

Figure 5.31: Relative trend of the series resistance for the two devices.

Summary

The current step-stress experiments on QD lasers with different substrate material composition highlighted some features in the two devices:

- a general increase in non-radiative recombination for both devices. This can be explained with SRH recombination, due to an increase of defects and diffusion processes in the active region, in combination with an increase in carrier escape rate from the quantum dots,
- a lower temperature dependence for the GaAs-substrate laser, from due to the much lower concentration of extend defects,
- an higher self-heating of the GaAs-substrate device, due to the GaAs material parameters (lower thermal conductivity) and the epitaxial structure of device itself (two additional separate confinement layers),
- a faster degradation rate for the silicon-substrate device, related to the presence of defects related to the substrate mismatch,
- similar dynamics regarding the spectra taken during the stress with increasing currents, showing the presence of the excited state 2 emission. The silicon-substrate device better shows this emission because of the reduced number of QWELLs
- an unexpected shift toward shorter-wavelength emission for the GaAs-substrate device at higher currents, possibly due to a progressive reduction in the QD dimensions as a consequence of damages in the edges of the material.

5.3 Constant-current stress comparison

In the following section, the comparison of constant-current stress between a 6 μm ridge width GaAs-substrate and Si-substrate device will be presented. Both devices were stressed at 300 mA, for 33970 minutes (566 h), i.e. when the devices showed sufficiently optical degradation. The characterization before and after-stress, as well as the constant-current stress procedure, follows the stages described in the first part of the chapter.

Characterization pre-stress

The optical characterization before-stress highlights the different temperature dependence of the two devices. Figure 5.32 exhibits again the different effects arising from a native-substrate device, in which dislocation density is low.

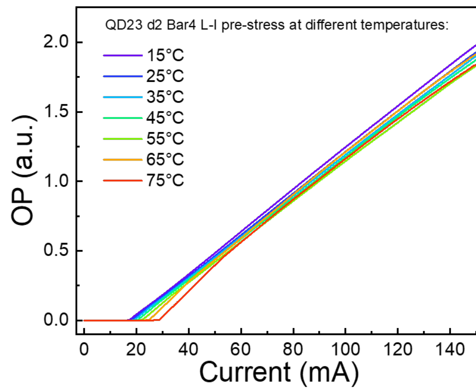

(a) GaAs-substrate, linear scale

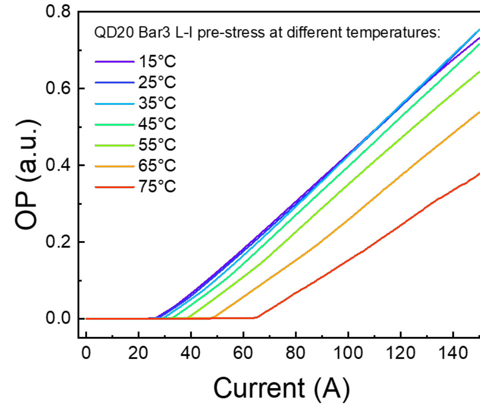

(b) Si-substrate, linear scale

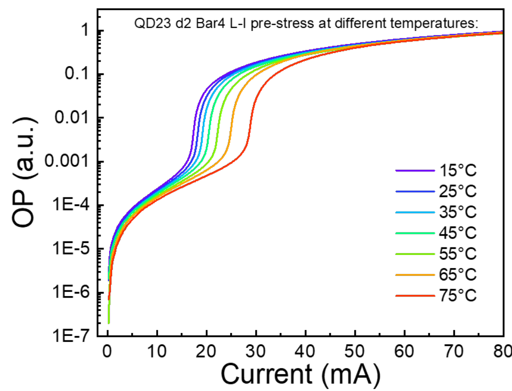

(c) GaAs-substrate, semi-logarithmic scale

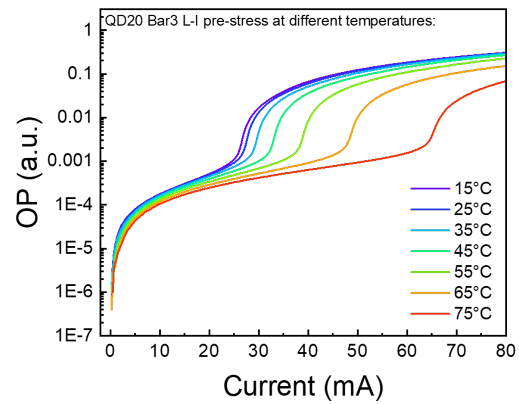

(d) Si-substrate, semi-logarithmic scale

Figure 5.32: L-I characteristics before-stress at different temperatures.

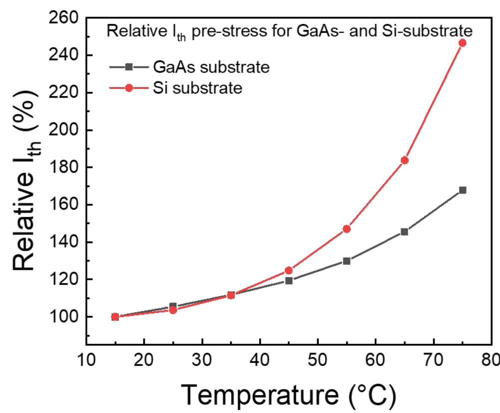

(a) Relative I_{th}

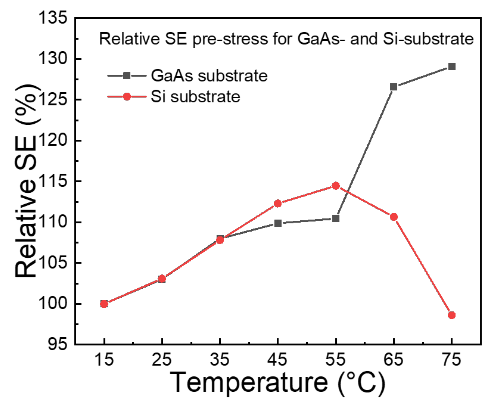

(b) Relative SE

Figure 5.33: I_{th} and SE trend in function of temperature.

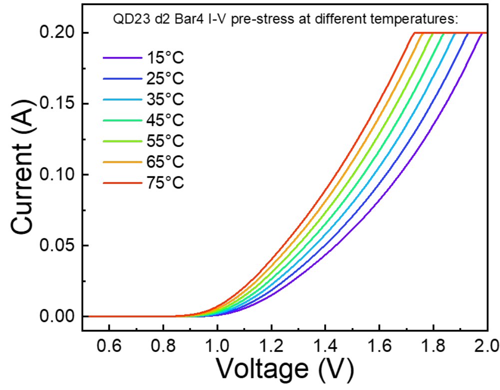

(a) GaAs-substrate, linear scale

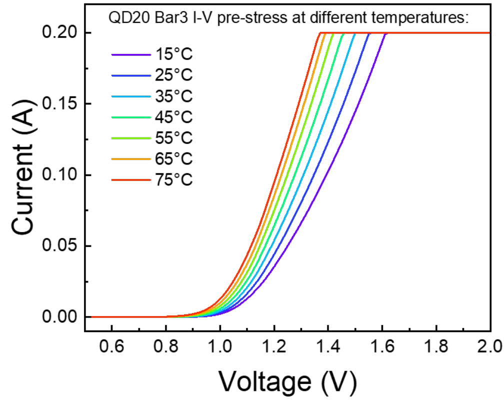

(b) Si-substrate, linear scale

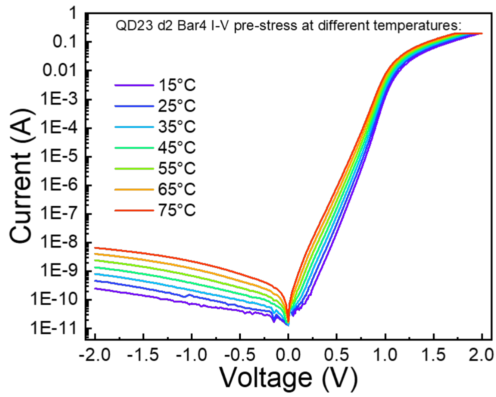

(c) GaAs-substrate, semi-logarithmic scale

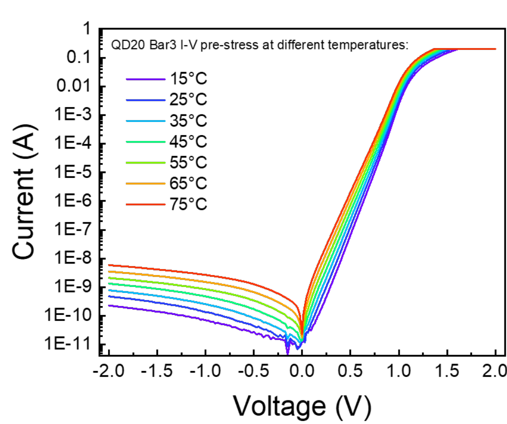

(d) Si-substrate, semi-logarithmic scale

Figure 5.34: I-V characteristics before-stress at different temperatures.

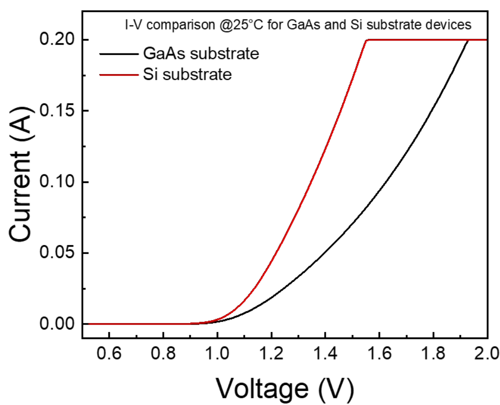

(a) GaAs-substrate, linear scale

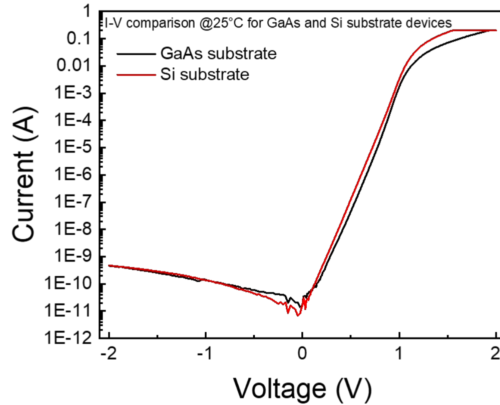

(b) Si-substrate, linear scale

Figure 5.35: I-V characteristics measured at 25°C.

Both devices show an increase in I_{th} with increasing temperature, caused by carrier escape and overflow. The slope efficiency trend shows how the silicon-substrate optical efficiency drops for temperatures higher than 55°C. The additional SCH layers of the GaAs-substrate device could improve the carrier confinement inside the active region. The I-V characteristics do not show particular differences besides the different series resistance contribute of the diode. The results are shown in Figure 5.34, while an I-V comparison of the two devices at a chosen temperature in shown in Figure 5.35.

Constant-current stress

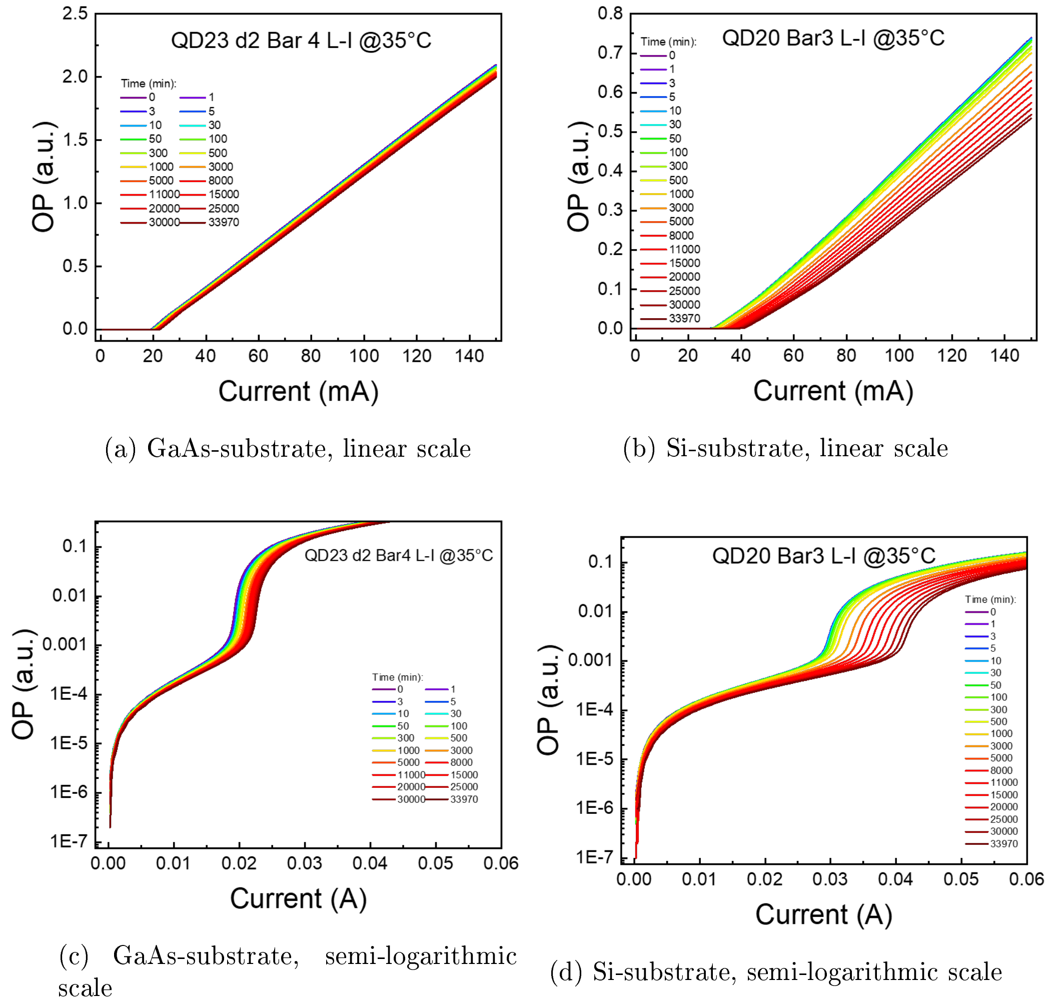

(a) GaAs-substrate, linear scale

(b) Si-substrate, linear scale

(c) GaAs-substrate, semi-logarithmic scale

(d) Si-substrate, semi-logarithmic scale

Figure 5.36: L-I characteristics versus stress-time.

The L-I characteristics taken at the beginning of each time-step are shown in Figure 5.36.
Both devices show an increase in the threshold current, a decrease in SE and a decrease in subthreshold emission. However, the variation from the silicon-substrate device is found to be stronger. The difference can also be shown by the I_{th} vs stress-time and SE vs stress-time, in Figure 5.37. In this case the silicon-substrate device shows a better behavior for stress-time less than 1000 min. After this, both characteristics diverge from the GaAs-substrate device trend, despite the junction temperature for the GaAs-substrate device should be higher.

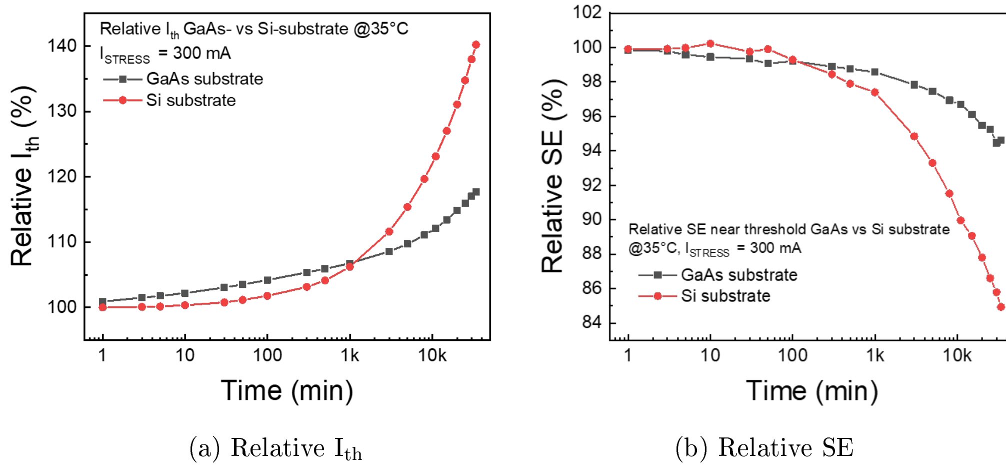

(a) Relative I_{th} (b) Relative SE

Figure 5.37: Relative I_{th} and SE vs stress-time.

In order to investigate the processes behind this faster degradation, it is useful to firstly observe the I_{th} vs 1/SE plot. It has already been shown that a strong correlation between the increase in I_{th} and the decrease in SE suggests that the optical degradation can largely be ascribed to a stress-induced decrease in injection efficiency. Figure 5.38 confirm this assumption. For the silicon-substrate device the linear correlation begins for $I_{STRESS} >$ 660 mA. The GaAs-substrate device shows a less linear correlation, due to a different effect of the degradation mechanism on the device especially at the beginning.

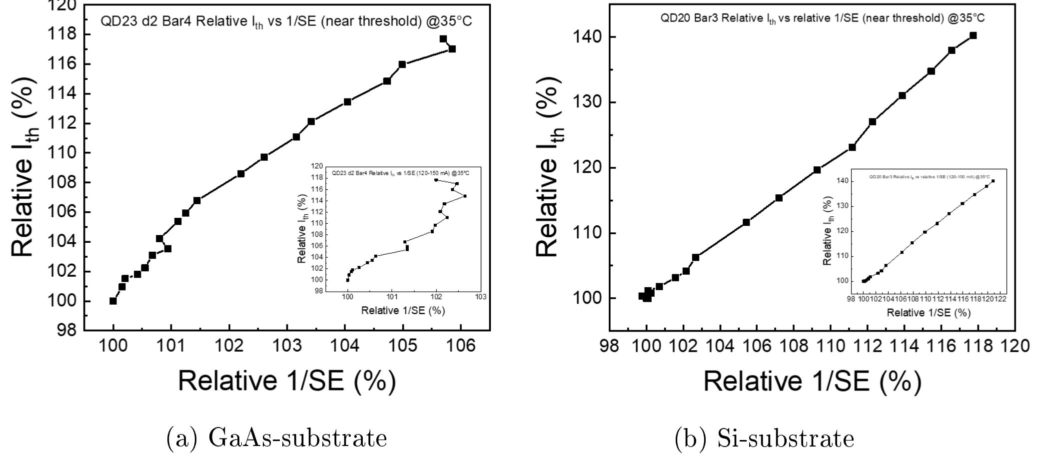

(a) GaAs-substrate

(b) Si-substrate

Figure 5.38: I_{th} vs 1/SE for (a) GaAs-substrate and (b) Si-substrate devices. The inset shows the results with the slope efficiency value taken for higher currents.

A second analysis concerns the threshold current dependence on the square root of time (Figure 5.39). This relationship suggests that impurities are diffusing towards the active region of the device. A diffusion process can be described through Fick's second law:

$$\frac{\partial N}{\partial t} = D\frac{\partial^2 N}{\partial^2 t} \tag{5.7}$$

with N is the impurity concentration per unit volume and D is the diffusion coefficient. Assuming a constant concentration of N_0 in the material, Fick's law can express the variation of concentration in terms of temporal variation t and depth x of the material

$$N(x,t) = N_0 \; erfc\left(\frac{x}{2\sqrt{Dt}}\right). \tag{5.8}$$

Additionally, the diffusion of defects has direct impact in the non-radiative lifetime, so a decrease in non-radiative lifetime is supposed to have a square-root dependence on time. Results in Figure 5.39 show the I_{th} linear dependence on the square-root of time, suggesting the diffusion of non-radiative recombination centers into the active region of the devices, that contributes to the degradation of the device through SRH recombination processes. From the slope of the curves in Figure 5.39(b) it can be seen how after 1000 min of stress-time the degradation in the silicon-substrate device greatly increases, as previously seen in the I_{th} and SE dynamics. This could be caused by the existence of a higher concentration of dislocation respect to the native-substrate device. Before 1000 minutes, the GaAs-substrate device shows a

non-linear and faster increase in the threshold current. It is possible that this initial phase is too fast to be observed in the silicon-substrate device.

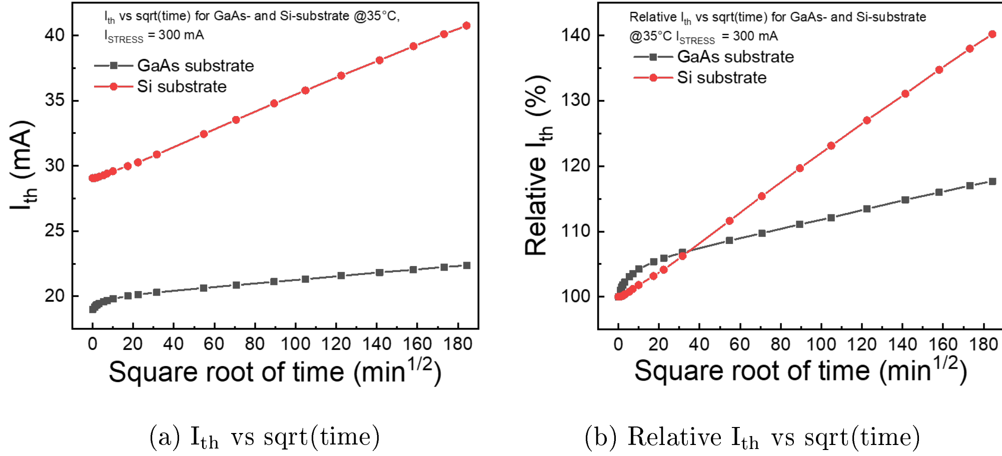

(a) I_{th} vs sqrt(time) (b) Relative I_{th} vs sqrt(time)

Figure 5.39: Variation of the threshold current as a function of the square root of stress-time.

The effect of SRH recombination can be observed from the correlation between the sub-threshold slope emission (OP_{sub}) and the threshold current.

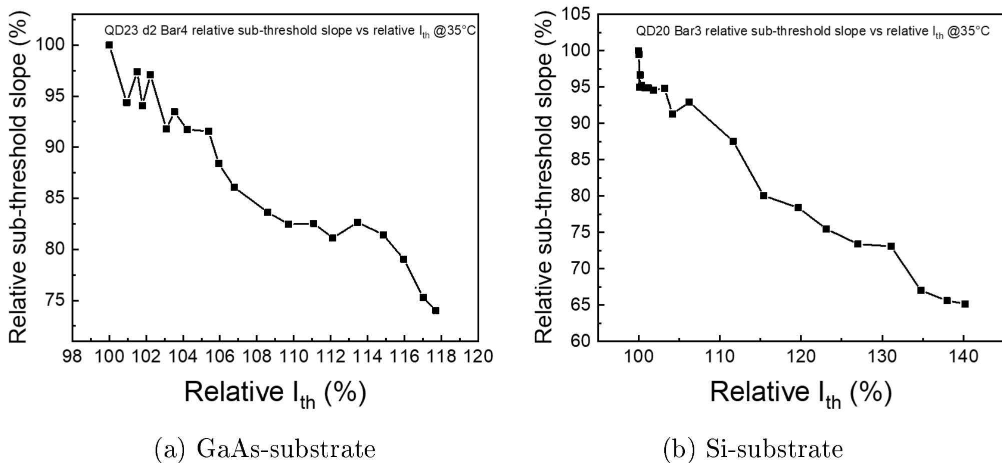

(a) GaAs-substrate (b) Si-substrate

Figure 5.40: Variation of the sub-threshold slope as a function of the threshold current.

Both quantities depends on the balance between radiative and non-radiative

recombination

$$OP_{SUB} \propto N/\tau \cong N(A + BN)$$
$$I_{th} \propto \frac{1}{\eta_{inj}} \frac{N_{th}}{\tau} \cong \frac{(A + BN_{th} + CN_{th}^2)N_{th}}{\eta_{inj}} \tag{5.9}$$

with A, B, C the SRH, bimolecular and Auger recombination coefficients, N_{th} the threshold carrier density. Thus, a correlated decrease of these quantities could be ascribed to an increase in the SRH recombination.
The difference between the optical power during stress is massive between the two devices and it is shown in Figure 5.41: the GaAs-substrate device results stable in time, while the silicon-substrate device shows a degradation in optical power up to the 85% of its initial value.

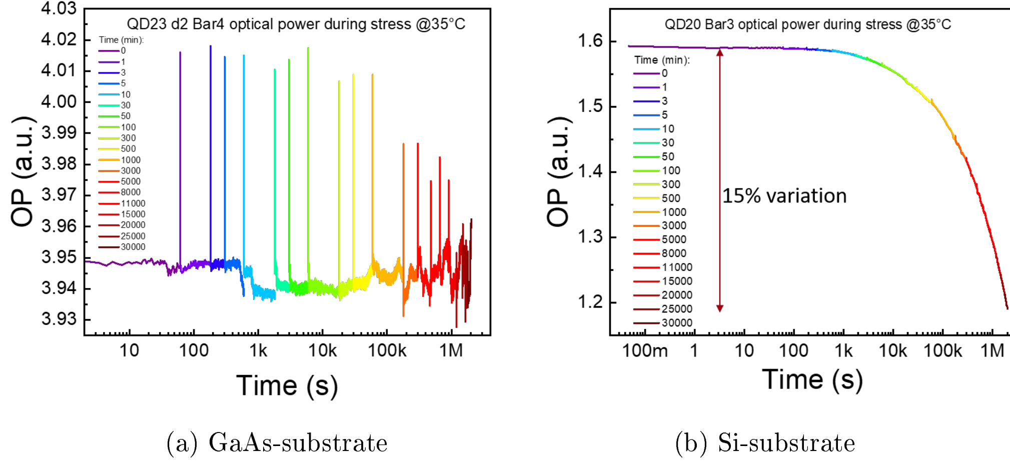

(a) GaAs-substrate (b) Si-substrate

Figure 5.41: Optical power trend at 300 mA, as a function of the stress-time.

The variation of the operating voltage as a function of stress-time is displayed in Figure 5.42 and shows, simply observing both the Y-axis, a massive decrease of voltage at the device turn-on, caused by the self-heating due to minor thermal conductivity and thicker substrate. The difference in absolute forward voltage can be ascribed to the different doping values or the annealing of the ohmic contacts.

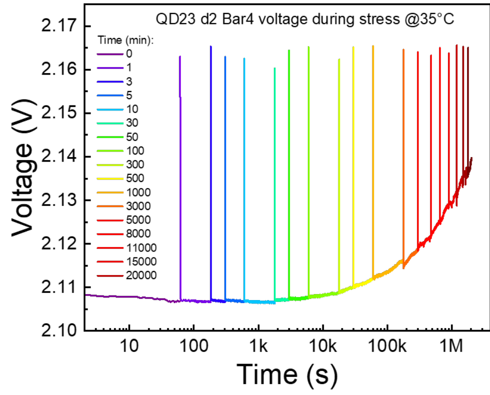

(a) GaAs-substrate

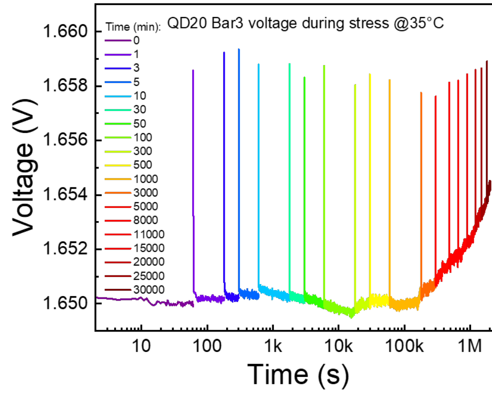

(b) Si-substrate

Figure 5.42: Operating voltage trend at 300 mA, as a function of the stress-time.

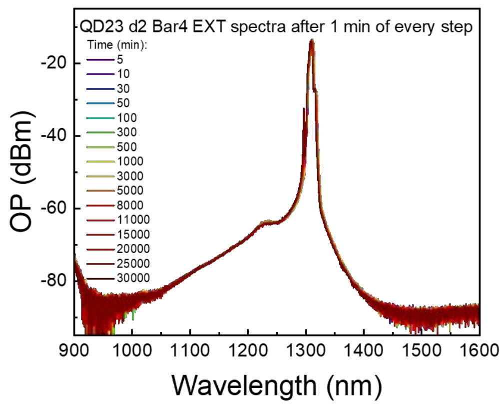

(a) GaAs-substrate

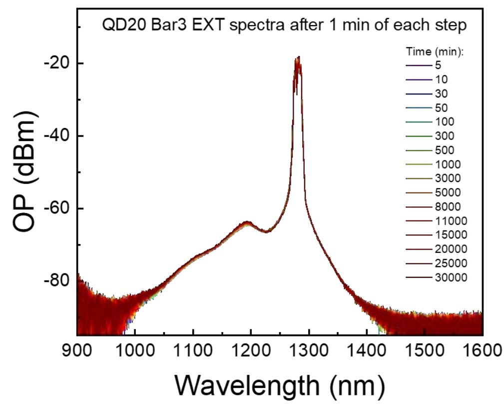

(b) Si-substrate

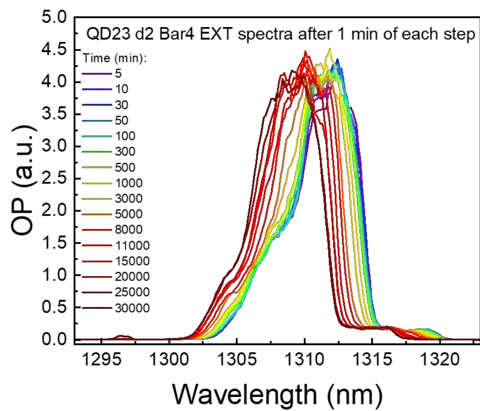

(c) GaAs-substrate, linear scale

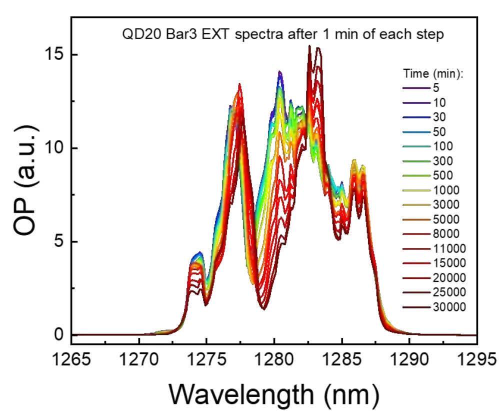

(d) Si-substrate, linear scale

Figure 5.43: Spectra taken after 1 minute from the beginning of each time step.

The spectra taken after 1 minute of each stress step are shown in Figure 5.43 and show the same differences described in the step-stress comparison: the silicon-substrate device exhibit a slight shift towards higher wavelengths due to self-heating and consequent bandgap narrowing of the device, while the native-substrate device seems having a rigid shift towards shorter wavelengths that needs deeper investigation. In Figures 5.43(a) and (b) it can be seen how the excited state 1 and 2 emissions are slowly turning on even in constant bias conditions, i.e. the carrier injection rate is constant. This can suggest that degradation is affecting the GS and could eventually favor the ES emission: the carriers that do not relax into the GS, and that do not overflow into the QWs, have to occupy other available states, such as the ES.

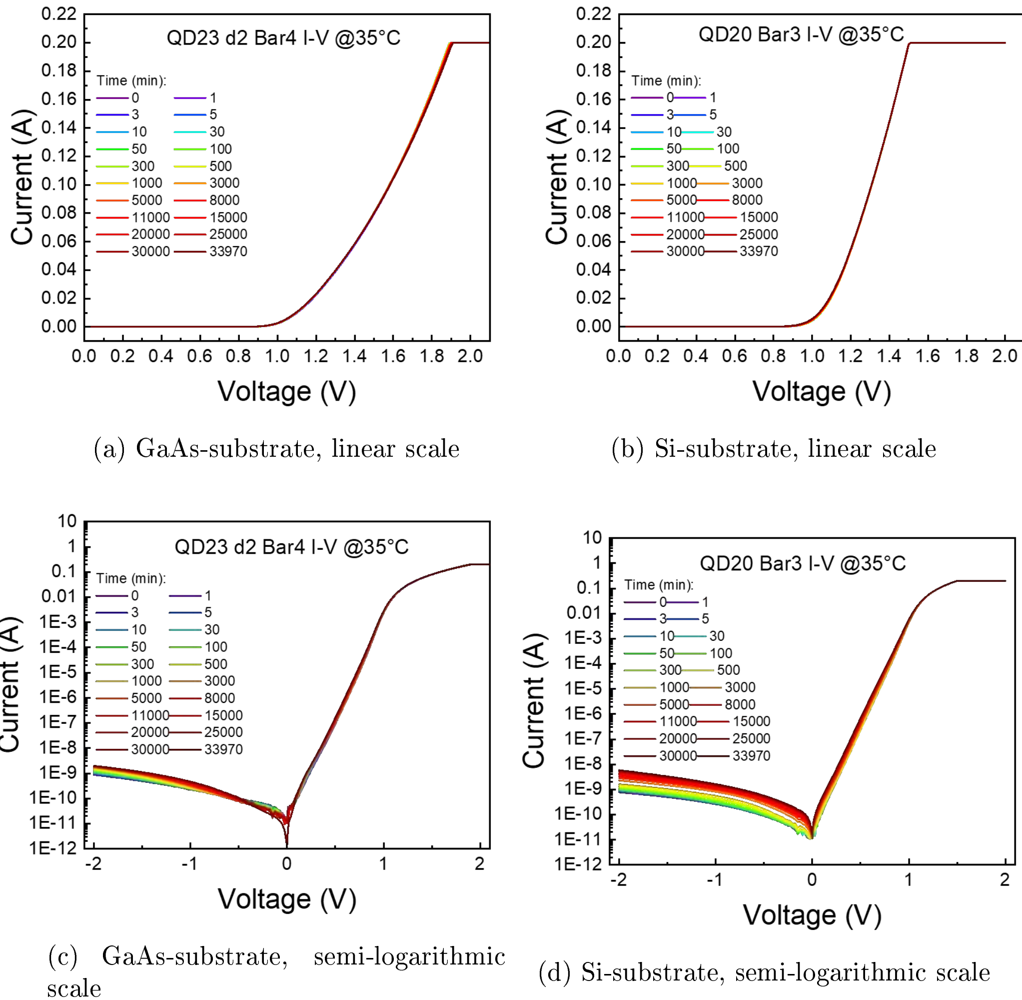

(a) GaAs-substrate, linear scale

(b) Si-substrate, linear scale

(c) GaAs-substrate, semi-logarithmic scale

(d) Si-substrate, semi-logarithmic scale

Figure 5.44: I-V characteristics versus stress-time.

Finally, the I-V curve taken at the beginning of each time step (Fig. 5.44) shows a similar variation of the electrical characteristics in reverse leakage and low-forward current. This variation ca be related to carrier transport mediated by defects, whose concentration is increasing near the active region of the devices.

Characterization post-stress

The defects introduced by the degradation mechanisms during the stress have mostly modified the optical characteristics, resulting in a worsening of the optical performances, and increase in the I_{th} as shown in Figure 5.45 and Figure 5.46, where the results before-stress are added to better understanding of the stress effects.

Summary

The constant step-stress comparison has raised the following discussions:

- the native-substrate L-I curves show a minor temperature dependence due to less dislocations density,
- the native-substrate device starts with a faster degradation rate, that changes after 100 minutes,
- both devices are affected by the diffusion of non-radiative recombination centers that are moving towards the active region of the device and cause an increase in SRH recombination rate
- the GaAs-substrate device does not show a big variation in optical power as a function of stress-time; however, the minor thermal conductivity and the thickness of the substrate material cause a major self-heating of the device. This difference can also be seen by the operating voltage trend during the experiment, that exhibit a bigger drop at the device turn-on due to the presence of the two additional SCH layers and the different extension of the DWELL layers,
- the degradation at constant bias seems to have some effects on the recombination dynamics within the active layers the devices: carriers that cannot escape the WL will eventually recombine in the ES level due to its higher degeneracy and to hole sharing.

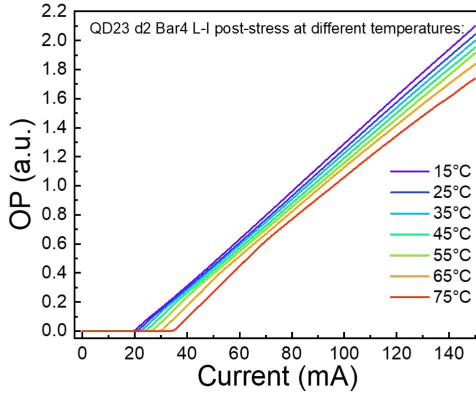

(a) GaAs-substrate, linear scale

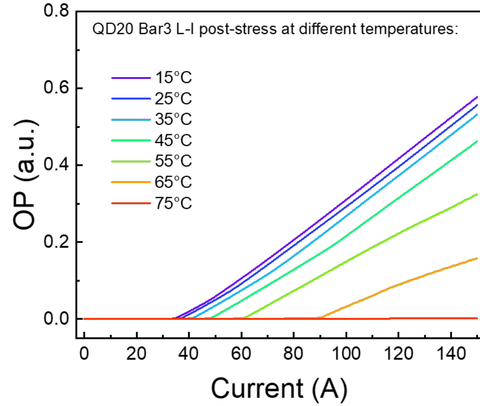

(b) Si-substrate, linear scale

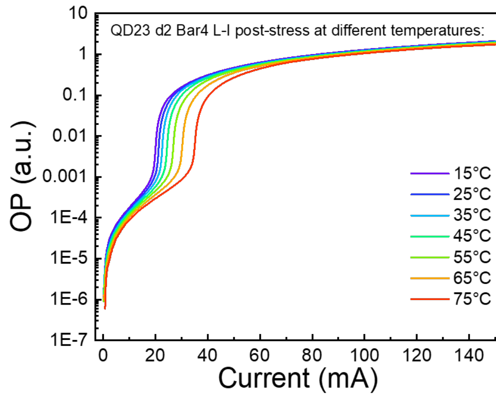

(c) GaAs-substrate, semi-logarithmic scale

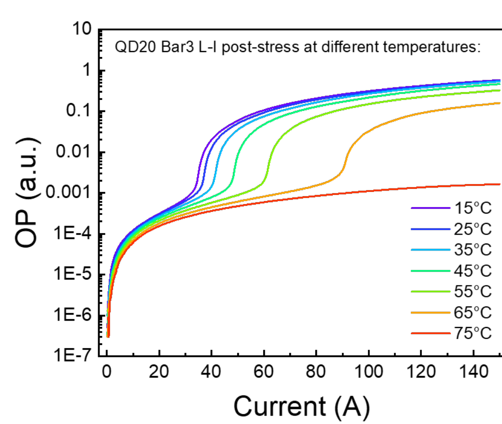

(d) Si-substrate, semi-logarithmic scale

Figure 5.45: L-I characteristics as a function of temperature.

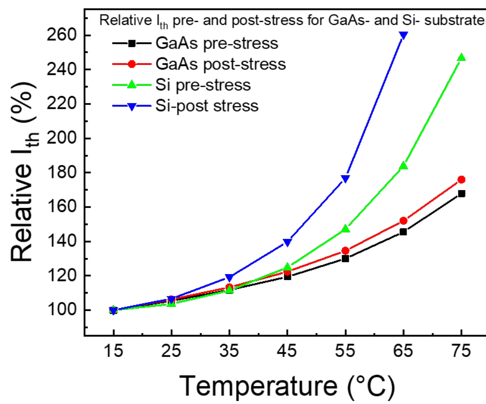

(a) GaAs-substrate

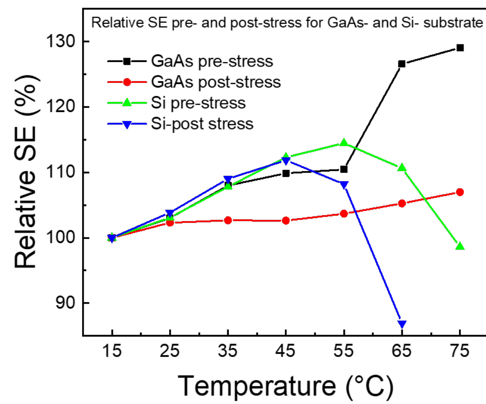

(b) Si-substrate

Figure 5.46: I_{th} and SE variation with temperature, pre- ad post-stress.

5.4 Characterization at cryogenic temperatures

In this section, I-V and L-I measurements were performed on a silicon-substrate device in order to observe the effect of self-heating at cryogenic temperatures and the evolution of the threshold current and the slope efficiency.
The measurements were performed at longer and shorter integration time, from 180 K to 340 K, with 10 K step. A third characterization was done by means of voltage pulses: the pulse duration was 50 μm with a period of 9 ms, resulting in 0.56% of duty cycle; the pulse amplitude was increasing with a step of 50 mV, from 1 V to 10 V. An external resistance of 98.55 Ω was added to deliver precise current pulses.

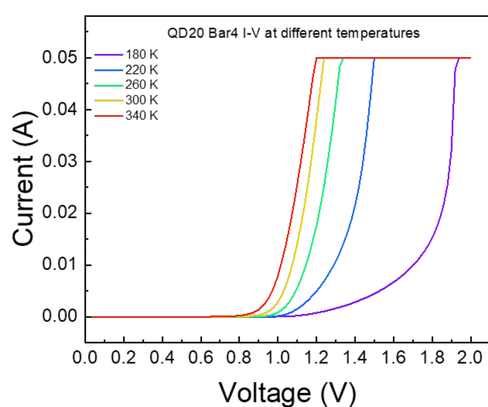

(a) Long integration time, linear scale

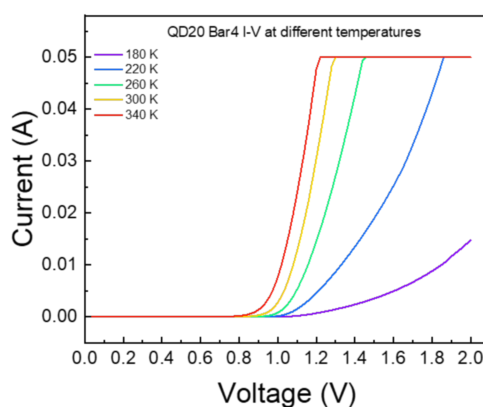

(b) Short integration time, linear scale

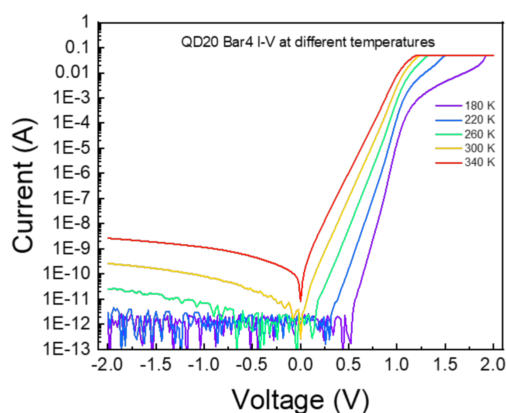

(c) Long integration time, semi-logarithmic scale

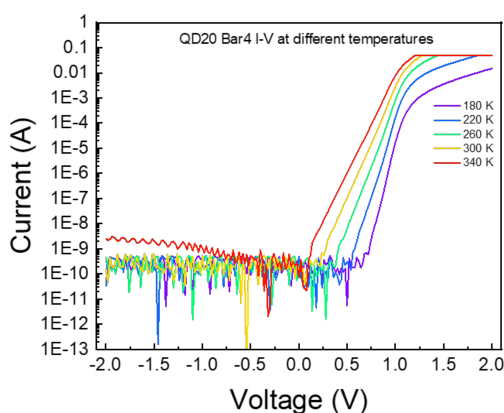

(d) Short integration time, semi-logarithmic scale

Figure 5.47: I-V characteristics as a function of temperature.

The I-V plot for long and short integration time are shown in Figure 5.47, not all the curves are plotted for clarity. It can be noted how the reduced carrier mobility at lower temperatures can impact on the current diode, drastically lowering it.

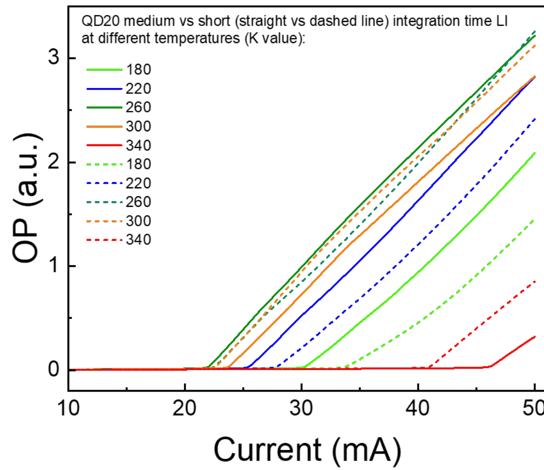

Figure 5.48: Comparison between long and short integration time that highlight the role of self-heating of the device.

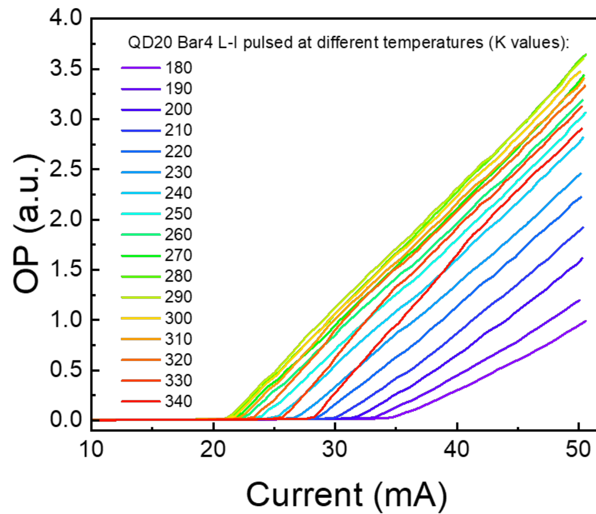

Figure 5.49: L-I curves by means of pulsed measurements.

To better understand the device behavior as a function of the integration time, I_{th} and SE vs T plots are extrapolated from the respective L-I curves

and the results are shown in Figure 5.50.

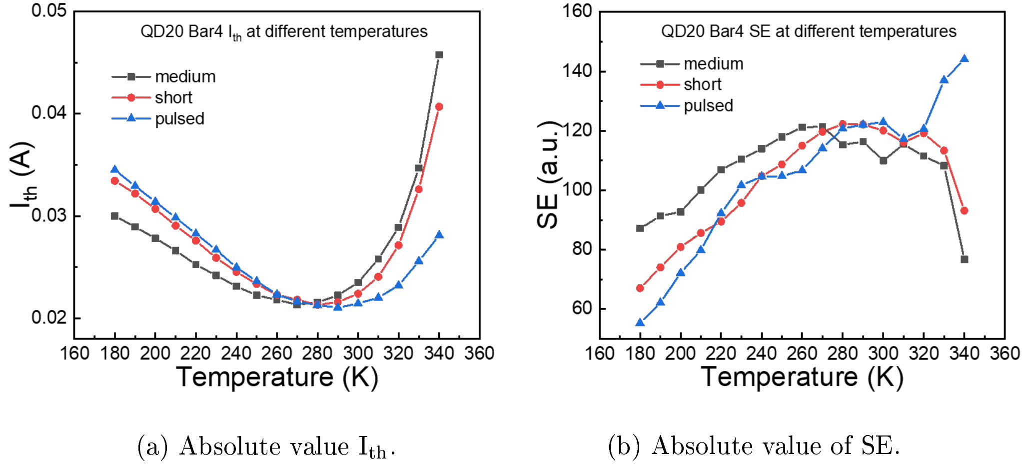

(a) Absolute value I_{th}.

(b) Absolute value of SE.

Figure 5.50: I_{th} and SE for different integration time values.

A comparison of the L-I curve is shown in Figure 5.48, in which the difference between two curves at the same temperature is massive, exhibiting the high impact of self-heating. A low injection efficiency might be the cause of the higher I_{th} for 180 K respect to, for instance, 220 K.
The L-I curves at pulsed currents are presented in Figure 5.49: again, it is possible to observe how the curves shift depending on the temperature and how the optical efficiency changes increasing with increasing temperature.
For low temperatures the device is affected by a low injection efficiency, which results in a unexpected high threshold current. For higher temperatures the I_{th} increase because of carrier escape. Interestingly, Figure 5.50 shows a localized minimum around 280/290 K, from which the threshold current increases. The slope efficiency shows a general improvement of the optical efficiency, that exhibits a drop after a plateau from 270 K to 320 K for the long and short integration time, probably due to excessive carrier escape influenced by self-heating.

5.5 DLTS results

Before proceeding with the effective DLTS measurements, a C-V characterization was performed at three different temperatures, as Figure 5.51 shows. From here, using Equations **??** and **??**, it was possible to obtain the apparent charge profile as a function of voltage (Fig. 5.52(a)) and apparent depth (Fig. 5.52(b)).

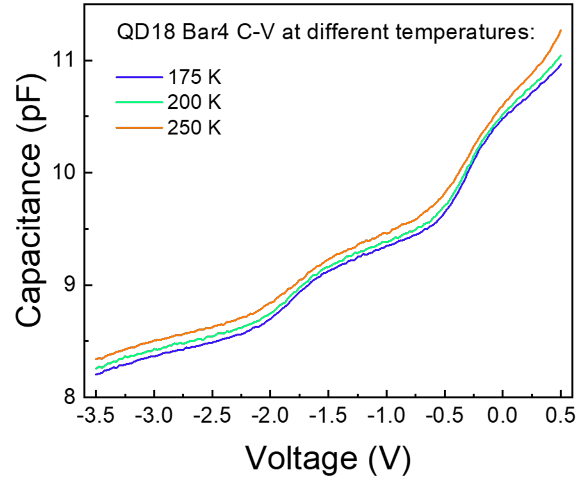

Figure 5.51: Capacitance-voltage characteristics for three different temperatures.

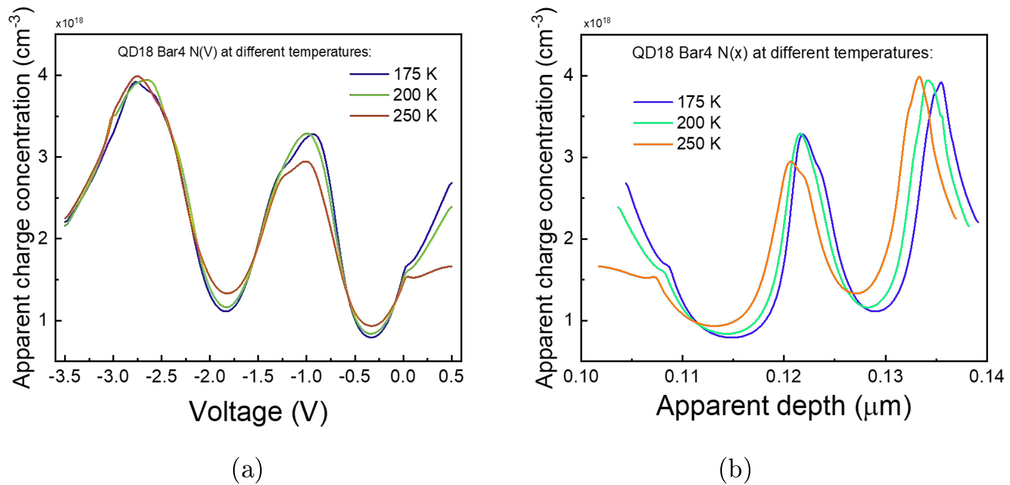

Figure 5.52: Apparent charge profile as a function of (a) voltage and (b) apparent depth.

Not being able to interpret the apparent charge profile trend, DLTS was used to scan the device with different voltage ranges at lower and high apparent charge profile regions, biasing the device at V_{bias} and varying the voltage till V_{fill}.

The voltage ranges are the following:

- V_{bias} = -2.25 V, V_{fill} = -1.45 V,
- V_{bias} = -1.45 V, V_{fill} = -0.6 V,
- V_{bias} = -0.6 V, V_{fill} = 0.0 V,
- V_{bias} = 0.0 V, V_{fill} = +0.4 V,

and two significant results are reported in Figure 5.53. There are three negative peaks, that for a p-doped material means the presence of three majority-trap type, from now on called H1, H2 and H3. Following the DLTS theory explained in Chapter 4, in order to extract the trap activation energy and the trap cross section we need to individuate the $\Delta C/C$ peak for every time correlator and then plot the results as a function of q/k_BT. The procedure was done by means of bigaussian deconvoltion for the first two peaks, since they are very close to each other. The Arrhenius plot is shown in Figure 5.54, where (a) and (b) are the plots corresponding to Fig. 5.53(a) and (b), while Fig. 5.54(c) summarizes all the four scanning-region results.

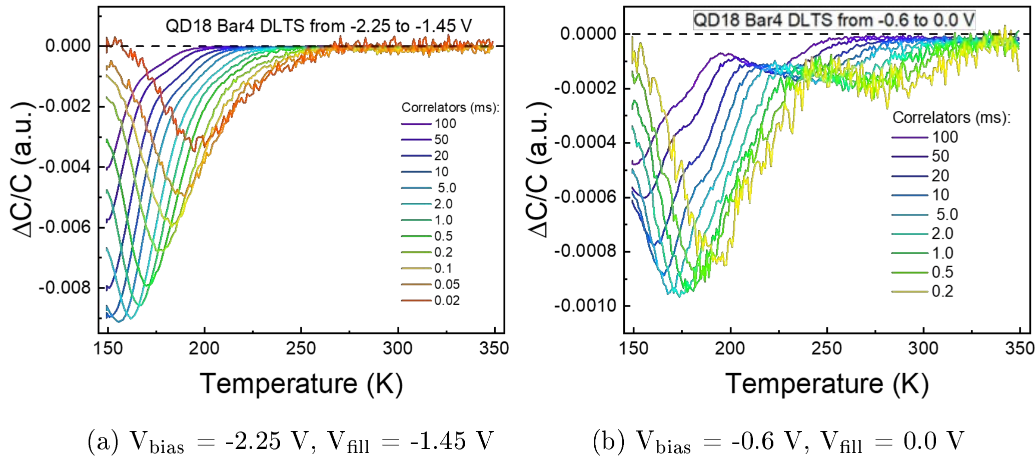

(a) V_{bias} = -2.25 V, V_{fill} = -1.45 V (b) V_{bias} = -0.6 V, V_{fill} = 0.0 V

Figure 5.53: DLTS results.

The linear fit was useful to extract the slope and the intercept of the curves of every trap, in order to determine the activetion energy E_a and the cross section σ_n, whose results are summarized in Figure 5.55. Additionally, the trap concentration N_T is calculated starting from the $\Delta C/C_{max}$ of every Arrhenius plot and using the Equation 4.8.

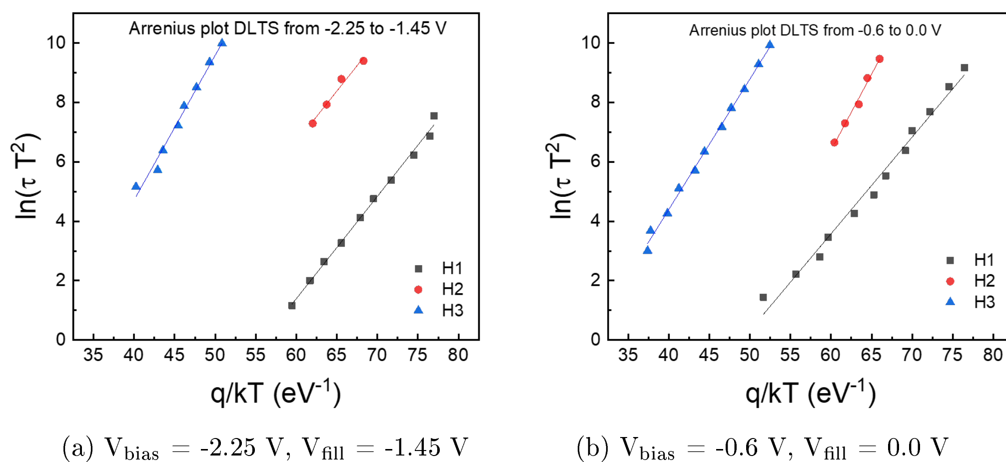

(a) V_{bias} = -2.25 V, V_{fill} = -1.45 V

(b) V_{bias} = -0.6 V, V_{fill} = 0.0 V

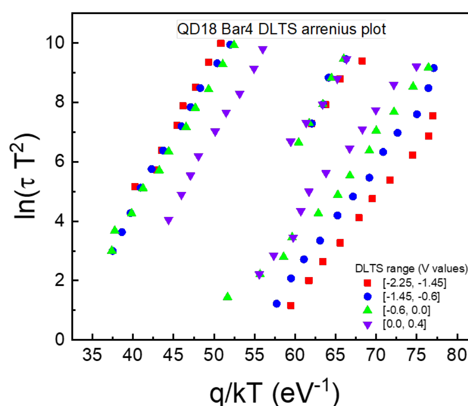

(c) Total

Figure 5.54: Arrhenius plot of the energy levels detected.

	DLTS 0.0 V 0.4 V			DLTS -0.6 V 0.0 V			DLTS -1.45 V -0.6 V			DLTS -2.25 V -1.45 V		
Trap	E_a (eV)	σ_n (cm^2)	N_T (cm^{-3})	E_a (eV)	σ_n (cm^2)	N_T (cm^{-3})	E_a (eV)	σ_n (cm^2)	N_T (cm^{-3})	E_a (eV)	σ_n (cm^2)	N_T (cm^{-3})
H1	0.373	4.81×10^{-17}	1.81×10^{15}	0.322	3.24×10^{-18}	4.46×10^{15}	0.384	5.64×10^{-16}	2.04×10^{16}	0.345	1.18×10^{-16}	4.16×10^{16}
H2	0.396	1.14×10^{-17}	-	0.512	1.84×10^{-14}	-	0.531	6.23×10^{-16}	-	0.343	5.50×10^{-19}	-
H3	0.479	1.25×10^{-17}	7.00×10^{14}	0.439	2.56×10^{-19}	7.10×10^{14}	0.474	9.93×10^{-19}	7.47×10^{14}	0.487	1.28×10^{-18}	2.81×10^{14}

Figure 5.55: Summary of the characteristics of traps H1, H2, H3 obtained by means of Arrhenius plots.

Chapter 6

Conclusions

With this work we have presented a detailed analysis of the reliability of QD Laser Diodes growth on different substrate materials. The analysis has been aimed at identifying the physical degradation mechanisms of QD lasers grown on silicon and studying the impact of extended dislocations, comparing devices grown on GaAs and Si substrate. For this purpose, several current step-stress and constant-current stress have been carried out, at constant temperature of 35°C. Before starting with the stress experiments, a preliminar current step-stress has been performed on the silicon-substrate device in order to evaluate the short-term impact of DC stress at different bias currents on the electro-optical characteristics of the device. We found that, depending on the current injection level, there are three operating regimes, associated to different spectral features. In particular, the laser spectrum can consist of only ground-state emission, only excited-state emission, or both types simultaneously. The ground-state is the lowest, or fundamental, energy level inside the quantum-dot, and constitutes the normal operating regime for commercial lasers.
The devices under investigation were InAs quantum dot lasers within an InGaAs quantum-well, tuned for an emission at 1.3 μm and epitaxially grown on GaAs or Silicon substrate. The two types of lasers had some differences in their epitaxial structure, in particular:

- the GaAs substrate was thicker than the Si-substrate,
- the active region of the GaAs-substrate device consisted of 5 layers of InAs quantum dots embedded in 7 nm of $In_{0.15}Ga_{0.85}As$ quantum wells, while the silicon-substrate device) had 3 layers in ∼9 nm of $In_{0.15}Ga_{0.85}As$ quantum wells,
- high-reflection **facet coating** was applied on one side of the bar to reduce optical carrier loss and improve light amplification,

- an additional separate confined heterostructure made of $Al_{0.2}Ga_{0.8}As$ was grown outside the active region of the GaAs-substrate device to further improve carrier confinement.

Some common degradation processes have been found to affect all the tested devices. In particular, with regards to the electrical properties, we observed a slight reduction in the diode turn-on voltage and the series resistance, which can be ascribed to the annealing of the ohmic contacts or of part of the dopant present in the quasi-neutral regions. A change in the carrier injection and escape mechanisms as a consequence of both thermal and electrical stress can also be considered. Furthermore, an increase in the reverse leakage current was detected, indicating a possible stress-induced increase of defect density within the material. The optical characteristics of the various devices behaved in a similar way, showing a significant increase in the threshold current and a decrease in the slope efficiency. The correlation between these two parameters suggested a progressive reduction in the injection efficiency, indicating a decrease in the fraction of terminal current that generates carriers in the active region. This could be due to higher potential barriers or electrostatic repulsion that occur around the active region. A higher escape rate of the carriers could also be considered. In either case, an increase in the non-radiative recombination processes occurs, thus leading to a reduced efficiency and output power. Moreover, regarding the constant-step stress experiments, the square-root dependence of the threshold current with respect to the stress-time also suggests the presence of an ongoing diffusion process, possibly related to the relocation of impurities toward the active region. The behavior of the threshold current in the very first moments of the stress, in which it takes some time for the square-root dependence to show up, seems to confirm this mechanism. However, this phenomenon is clearly seen for the GaAs-substrate device, while it seems to be very rapid for the silicon-substrate device. The spectral measurements have been a useful tool to study the impact of the degradation processes on the energy of the emitted photons. More in details, the devices show the so-called two state lasing, in which both ground-state and excited-state are emitting. Afterwards, the ES starts dominating and will eventually quench the GS emission. This has been explained in different ways: (a) at high current levels, the difference in carrier occupation probability disappears and, since ES has a higher degeneracy than GS, ES will be the only one lasing; (b) self-assembled quantum dots show homogeneous broadening of the optical gain as well as retarded carrier relaxation into the quantum-dot discrete energy states; (c) hole injection is low at higher currents: in this bias regime, the carrier population of in the GS is clamped and, since the GS and ES levels for holes are very close, holes are shared between the electrons of the GS and ES, thus leading to their consumption only by ES due to its higher degeneracy (that can be seen as the reduction of the radiative lifetime associated to it). The EL

spectra also showed the presence of three bumps. Calculation relating the wavelength with the energy emission brought out the existence of a higher energy state over the ES, called excited-state 2.
The current-step stress performed both on a GaAs- and Si-substrate devices highlighted important features and differences:

- the GaAs-substrate device is less sensitive to temperature variation: in fact in the pre- and post-stress characterization, it shows good stability and a less pronounced increase in threshold current,
- at high currents, the GaAs-substrate laser exhibits a non-negligible self-heating, that has direct consequences on the degradation rate of the device. In particular, the I_{th} shows a massive increase after the GS-quenching,
- a faster degradation rate for the silicon-substrate device, related to the existence of defects related to the substrate mismatch,
- an unexpected shift towards shorter-wavelength for the GaAs-substrate device at higher currents, possibly die to a progressive reduction on the QD dimensions as a consequence of damages in the edges of the material.

The constant-current stress comparison, on the other hand, has raised the following discussions:

- the presence of bumps and of the ES peak were observed even at constant current, suggesting that the fraction of the population of injected carriers undergoing recombination through the ES increases, whereas the GS emission decreases. An increase in the temperature, to some extent, can favor the quenching of the ground-state and the consequent onset of the excited-state,
- the native-substrate device shows a faster degradation at the beginning of the stress experiment with respect to the silicon-substrate device. However, after 1000 minutes, the silicon-substrate laser exhibit a rapid increase in threshold current.
- the decrease in injection efficiency during the stress experiment, i.e. the linear correlation between I_{th} and 1/SE, is not very clear for the GaAs-substrate due to a different effect of the degradation mechanism on the device,
- the GaAs-substrate shows a robust behavior in optical power during stress, that does not vary over the 0.3%, while the silicon-substrate optical power decrease variation reaches the 15% from its initial value. However, the GaAs-substrate device shows a massive decrease of

operating voltage during stress at the device turn-on, caused by the self-heating due to minor thermal conductivity and thicker substrate. The difference in absolute forward voltage can be ascribed to the different doping values or the annealing of the ohmic contacts.

Furthermore, a characterization at cryogenic temperatures provided information about the impact of the self-heating on a silicon-substrate device, showing that for low temperatures the device shows poor injection efficiency, thus having high threshold current values. DLTS measurements were useful to identify the deep levels inside the active region of the device. The Arrhenius plot provided data regarding the trap energy activation, cross section and concentration. In future experiments, further investigation will be needed in order to better explain some unexpecteed behavior of the lasers: the spectra during the stress showed a overall jump in optical power; one hypothesis might be related to carrier spreading into other semiconductor layers, that could justify the overall high-energy emission increase and be related to the excited state 2 emission. The low-energy portion of the spectra should always be linked to the emission from QDs. Another phenomenon regards the characterization spectra of the GaAs-substrate device, as well as its spectra taken during the constant-current stress: the device shows an peak emission that shift toward higher energies; this could be seen as a rigid shift of the emission shape or as the emission of a different subset of QDs that prevails and suppresses the other emissions.

In addition, the lasers will be stressed at higher temperatures, in order to accelerate the degradation mechanisms and to better evaluate their dependence on temperature. Finally, characterization measurements will be carried out by varying the junction temperature, which will hopefully enable a comprehensive understanding of the physical processes regulating the emission properties of such novel devices.

References

[1] R. Soref and J. Lorenzo, "All-silicon active and passive guided-wave components for $\lambda = 1.3$ and 1.6 μm," IEEE J. Quantum Electron., vol. QE-22, no. 6, pp. 873-879, Jun. 1986.

[2] B. Schuppert, J. Schmidtchen, and K. Petermann, "Optical channel waveguides in silicon diffused from GeSi alloy," Electron. Lett., vol. 25, no. 22, pp. 1500-1502, Oct. 1989.

[3] R. A. Soref, J. Schmidtchen, and K. Petermann, "Large single-mode rib waveguides in GeSi and Si-on-SiO2," IEEE J. Quantum Electron, vol. 27, no. 8, pp. 1971-1974, Aug. 1991.

[4] M. Gioannini and M. Rossetti, "Time-domain traveling wave model of quantum dot DFB lasers", IEEE J. Sel. Top. Quantum Electron. 17, 1318-1326 (2011).

[5] F. Gerschutz, M. Fischer, J. Koeth, M. Chacinski, R. Schatz, O. Kjebon, A. Kovsh, I. Krestnikov, and A. Forchel, "Temperature insensitive 1.3 μm InGaAs/GaAs quantum dot distributed feedback lasers for 10 Gbit/s transmission over 21 km," Electron. Lett., vol. 42, no. 25, pp. 1457-1458, Dec. 2006.

[6] L. Zhang, R. Wang, Z. Zou, A. Gray, L. Olona, T. Newell, D. Webb, P. Varangis, and L. Lester, "InAs quantum dot DFB lasers on GaAs for uncooled 1310 nm fiber communication," in Proc. Opt. Fiber Commun. Conf., Mar. 23-28, 2003, vol. 2, pp. 678-679.

[7] D. Bimberg, D. Arsenijevic, and M. Kleinert. "Jitter reduction by optical feedback of passively mode-locked quantum-dot lasers." 2013 IEEE Photonics Conference. IEEE, 2013.

[8] http://www.petra-jp.org/pj_pecjs/en/index.html

[9] D. Bimberg: Quantum dot based nanophotonics and nanoelectronics, Electron. Lett. 44, 168 (2008).

[10] D. Jung, P. G. Callahan, B. Shin, K. Mukherjee, A. C. Gossard, J. E. Bowers, "Low threading dislocation density GaAs growth on on-axis GaP/Si (001)," J. Appl. Phys. 122, 225703 (2017).

[11] I. George, F. Becagli, H. Y. Liu, J. Wu, M. Tang, R. Beanland, "Dislocation filters in GaAs on Si," Semicond. Sci. Technol. 30, 114004 (2015).

[12] T. Wang, et al. "1.3-μm InAs/GaAs quantum-dot lasers monolithically grown on Si substrates." Optics express 19.12 (2011): 11381-11386.

[13] H. Liu et al. "Long-wavelength InAs/GaAs quantum-dot laser diode monolithically grown on Ge substrate." Nature Photonics 5.7 (2011): 416.

[14] A. D. Lee, Q. Jiang, M. Tang, Y. Zhang, A. J. Seeds & H. Liu, "InAs/GaAs quantum-dot lasers monolithically grown on Si, Ge, and Ge-on-Si substrates." IEEE Journal of Selected Topics in Quantum Electronics, 19(4), 1901107-1901107, (2013).

[15] X. Wu et al., "Terabit Interconnects with a 20-GHz O-Band Passively Mode Locked Quantum Dot Laser Grown Directly on Silicon," 2019 Optical Fiber Communications Conference and Exhibition (OFC), San Diego, CA, USA, 2019, pp. 1-3.

[16] L. A. Coldren, S. W. Corzine, and M. L. Mashanovitch. "Diode lasers and photonic integrated circuits." Vol. 218. John Wiley & Sons, 2012.

[17] R. S.Muller, T. I.Kamins, M. Chan (1986). "Device electronics for integrated circuits."

[18] S. O. Kasap, R. K. Sinha (2001). "Optoelectronics and photonics: principles and practices" (Vol. 340). New Jersey: Prentice Hall.

[19] H. Haken: "Laser Light Dynamics, vol. II" (North Holland, 1st edition edition, 1986).

[20] S. Sze and K. K. Ng, "Physics of Semiconductor Devices." Hoboken, NJ, USA: John Wiley & Sons, Inc., oct 2006.

[21] E. F. Schubert, "Light Emitting Diodes, 2nd Edition," 2nd ed. Springer Verlag Berlin Heidelberg New York: Cambridge University Press, 2006.

[22] D. Bimberg, M. Grundmann, and N. N. Ledentsov. "Quantum dot heterostructures." John Wiley & Sons, 1999.

[23] E. Borovitskaya and M. Shur. "Quantum dots." World Scientific Pub Co Inc, 2002.

[24] L. E. Brus, "Electron-electron and electron-hole interactions in small semiconductor crystallites: the size dependence of the lowest excited electronic state", J. Chem. Phys. 80 (1984) 4403

[25] A. J. Nozik, F. Williams, M.T. Nenadovic, T. Rajh, O.I. Micic, Size quantization in small semiconductor particles, J. Phys. Chem. 89 (1985) 397-399

[26] A. D. Yoffe. "Low-dimensional systems: quantum size effects and electronic properties of semiconductor microcrystallites (zero-dimensional systems) and some quasi-two-dimensional systems." Advances in Physics 42.2 (1993): 173-262.

[27] E. F . Schubert. "Physical foundations of solid-state devices." E. Fred Schubert, 2015.

[28] G. Timp et al. "Quantum transport in an electron-wave guide." Physical review letters 59.6 (1987): 732.

[29] S. J. Tans et al. "Individual single-wall carbon nanotubes as quantum wires." Nature 386.6624 (1997): 474.

[30] J. Appenzeller, J. Knoch, M. T. Bjork, H. Riel, H. Schmid, and W. Riess, "Toward nanowire electronics," IEEE Transactions on Electron Devices, vol. 55, pp. 2827-2845, nov 2008.

[31] D. Kim and Y. Jeong, "Nanowire Field Effect Transistors: Principles and Applications." 2014.

[32] A. J. Nozik, "Quantum dot solar cells." Physica E: Low-dimensional Systems and Nanostructures 14.1-2 (2002): 115-120.

[33] Q. Sun et al. "Bright, multicoloured light-emitting diodes based on quantum dots." Nature photonics 1.12 (2007): 717.

[34] L. Zhuang, G. Lingjie, and Y. C. Stephen "Silicon single-electron quantum-dot transistor switch operating at room temperature." Applied Physics Letters 72.10 (1998): 1205-1207.

[35] D. L. Huffaker et al. "1.3 μm room-temperature GaAs-based quantum-dot laser." Applied Physics Letters 73.18 (1998): 2564-2566.

[36] D. Loss, and P. D. David "Quantum computation with quantum dots." Physical Review A 57.1 (1998): 120.

[37] I. L Medintz, et al. "Quantum dot bioconjugates for imaging, labelling and sensing." Nature materials 4.6 (2005): 435.

[38] L. Brus, "Electronic wave functions in semiconductor clusters: Experiment and theory," Journal of Physical Chemistry, vol. 90, no. 12, pp. 2555-2560, 1986.

[39] D. Klotzkin, K. Kamath, and P. Bhattacharya, "Quantum capture times at room temperature in high-speed In0.4Ga0.6As-GaAs self-organized quantum-dot lasers," IEEE Photonics Technology Letters, vol. 9, no. 10, pp. 1301-1303, 1997.

[40] A. Markus, J. X. Chen, O. Gauthier-Lafaye, J. G. Provost, C. Paranthoen, and A. Fiore: "Impact of intraband relaxation on the performance of a quantum-dot laser", IEEE J. Sel. Top. Quantum Electron. 9, 1308 (2003).

[41] M. Sugawara, N. Hatori, M. Ishida, H. Ebe, Y. Arakawa, T. Akiyama, K. Otsubo, T. Yamamoto, and Y. Nakata: "Recent progress in self-assembled quantum-dot optical devices for optical telecommunication: temperatureinsensitive 10 Gbs directly modulated lasers and 40 Gbs signal-regenerative amplifiers", J. Phys. D 38, 2126-2134 (2005).

[42] A. Markus, J. X. Chen, C. Paranthoen, A. Fiore, C. Platz, and O. Gauthier-Lafaye: "Simultaneous two-state lasing in quantum-dot lasers", Appl. Phys. Lett. 82, 1818 (2003).

[43] M. V. Maximov, Y. M. Shernyakov, F. I. Zubov, A. E. Zhukov, N. Y. Gordeev, V. V. Korenev, A. V. Savelyev, and D. A. Livshits: "The influence of p-doping on two-state lasing in InAs/InGaAs quantum dot lasers", Semicond. Sci. Technol. 28, 105016 (2013).

[44] V. V. Korenev, A. V. Savelyev, A. E. Zhukov, A. V. Omelchenko, and M. V. Maximov: "Analytical approach to the multi-state lasing phenomenon in quantum dot lasers", Appl. Phys. Lett. 102, 112101 (2013).

[45] M. Gioannini: "Ground-state quenching in two-state lasing quantum dot lasers", J. Appl. Phys. 111, 043108 (2012).

[46] K. Ludge and E. Scholl: "Temperature dependent two-state lasing in quantum dot lasers", IEEE Publishing Services, New York, 2012, IEEE Conf. Proc., pp. 1-6.

[47] A. E. Zhukov, M. V. Maximov, Y. M. Shernyakov, D. A. Livshits, A. V. Savelyev, F. I. Zubov, and V. V. Klimenko: Features of simultaneous groundand excited-state lasing in quantum dot lasers, Semiconductors 46, 231-235 (2012).

[48] H. M. Ji, T. Yang, Y. L. Cao, P. F. Xu, and Y. X. Gu: "Self-heating effect on the two-state lasing behaviors in 1.3-μm InAs-GaAs quantum-dot lasers, Jpn. J. Appl. Phys. 49, 072103 (2010).

[49] M. Sugawara et al. "Modeling room-temperature lasing spectra of 1.3-μm self-assembled InAs GaAs quantum-dot lasers: Homogeneous broadening of optical gain under current injection." Journal of Applied Physics 97.4 (2005): 043523.

[50] E. A. Viktorov, P. Mandel, J. Houlihan, G. Huyet, and Y. Tanguy: Electron-hole asymmetry and two-state lasing in quantum dot lasers, Appl. Phys. Lett. 87, 053113 (2005).

[51] H. Eisele, A. Lenz, R. Heitz, R. Timm, M. Dahne, Y. Temko, T. Suzuki, and K. Jacobi, "Change of InAs/GaAs quantum dot shape and composition during capping," Journal of Applied Physics, vol. 104, p. 124301, dec 2008.

[52] V. Lozovski and V. Piatnytsia. "The analytical study of electronic and optical properties of pyramid-like and cone-like quantum dots." Journal of Computational and Theoretical Nanoscience 8.11 (2011): 2335-2343.

[53] L. W. Wang, J. Kim, and A. Zunger. "Electronic structures of [110]-faceted self-assembled pyramidal InAs/GaAs quantum dots." Physical Review B 59.8 (1999): 5678.

[54] A. J. Williamson, L. W. Wang, and A. Zunger. "Theoretical interpretation of the experimental electronic structure of lens-shaped self-assembled InAs/GaAs quantum dots." Physical Review B 62.19 (2000): 12963.

[55] S. Amelinckx, W. Dekeyser, The structure and properties of grain boundaries, Solid State Phys. 8, 325 (1959)

[56] C.R.M. Grovenor, J. Phys. C: Solid State Phys. 18, 4079-4119 (1985)

[57] P.M. Petroff, in: Semiconductors and Semimetals, Vol. 22, 1985

[58] R.G. Waters, Diode laser degradation mechanisms: a review, Prog. Quant. Electr. 15 (1992

[59] M. Fukuda, Reliability and Degradation of Semiconductors Lasers and LEDs, Artech House, Boston, 1991.

[60] P. W.Epperlein "Semiconductor laser engineering, reliability and diagnostics: a practical approach to high power and single mode devices". John Wiley & Sons, 2013.

[61] P.G. Eliseev, Optical strength of semiconductor laser materials, Prog. Quant. Electr. 20 (1) (1996) 1.

[62] S. O'Hara, P.W. Hutchinson, P.S. Dobson, The origin of dislocation climb during laser operation, Appl. Phys. Lett. 30 (1977) 368.

[63] P.M. Petroff, L.C. Kimerling, Dislocation climb model in compound semiconductors with zinc-blende structure, Appl. Phys. Lett. 29 (1976) 461.

[64] L.C. Kimerling, Recombination enhanced defect reactions, Sol. St. Electron. 21 (1978) 1391.

[65] J. S. Roberts "The influence of trimethylindium impurities on the performance of InAlGaAs single quantum well lasers." Journal of crystal growth 195.1-4 (1998): 668-675.

[66] A.A. Hopgood, Vacancy controlled model of degradation in InGaAs/AlGaAs/GaAs heterostructure lasers, J. Appl. Phys. 76 (1994) 4068.

[67] K. Maeda and S. Takeuchi. "Recombination enhanced dislocation glide in InP single crystals." Applied Physics Letters 42.8 (1983): 664-666.

[68] K. Maeda, M. Sato, A. Kubo & Takeuchi, S. (1983). "Quantitative measurements of recombination enhanced dislocation glide in gallium arsenide." Journal of Applied Physics, 54(1), 161-168.

[69] T. Kamejima, K. Ishida & J. Matsui, (1977). "Injection-enhanced dislocation glide under uniaxial stress in GaAs-(GaAl) As double heterostructure laser." Japanese Journal of Applied Physics, 16(2), 233.

[70] K. Maeda, and S. Takeuchi. "Recombination enhanced dislocation glide in InP single crystals." Applied Physics Letters 42.8 (1983): 664-666.

[71] M. Fukuda, K. Wakita, G. Iwane, Dark defects in InGaAsP/InP double heterostructure lasers under accelerated aging, J. Appl. Phys. 54 (1983) 1246.

[72] J. W. Tomm, A. Barwolff, A. Jaegger, T. Elsaesser, J. Bollmann, W. T. Masselink, A. Gerhardt, J. Donecker, "Deep level spectroscopy of high-power laser diode arrays," J. Appl. Phys. 84 (1998) 1325.

[73] O. Ueda "Reliability and degradation of III-V optical devices focusing on gradual degradation." Materials and Reliability Handbook for Semiconductor Optical and Electron Devices. Springer, New York, NY, 2013. 87-122.

[74] Y. L. Khait, J. Salzman, R. Beserman, "Kinetic model for gradual degradation in semiconductor lasers and light emitting diodes, Appl. Phys. Lett. 53 (1988) 2135."

[75] M. Vanzi, A. Bonfiglio, F. Magistrali, G. Salmini, "Electron microscopy of life tested semiconductor laser diodes", Micron. 31 (2000) 259

[76] W. D. Laidig, N. Holonyak, M. D. Camras, K. Hess, J. J. Coleman, P. D. Dapkus, J. Bardeen, "Disorder of an AlAs-GaAs superlattice by impurity diffusion", Appl. Phys. Lett. 38 (1981) 776.

[77] A. Jakubowicz, A. Oosenbrug, T. Forster, "Laser operation induced migration of beryllium at mirrors of GaAs/AlGaAs laser diodes", Appl. Phys. Lett. 63 (9) (1993) 1185.

[78] G. Chen, C.L. Tien, Facet heating of quantum well lasers, J. Appl. Phys. 74 (1993) 2167.

[79] U. Menzel, R. Puchert, A. Barwolff, A. Lau, "Facet heating and axial temperature profiles in high power GaAlAs/GaAs laser diodes", Microelectron. Reliability 38 (1998) 821.

[80] Y. Sin et al. "Root causes investigation of catastrophic optical bulk damage in high-power InGaAs-AlGaAs strained QW lasers." Novel In-Plane Semiconductor Lasers XVII. Vol. 10553. International Society for Optics and Photonics, 2018.

[81] D. Inoue, D. Jung, J. Norman, Y. Wan, N. Nishiyama, S. Arai, A. C. Gossard, and J. E. Bowers, "Directly modulated 1.3 μm quantum dot lasers epitaxially grown on silicon," Optics Express, vol. 26, no. 6, p. 7022, 2018.

[82] Jung, Daehwan, et al. "High efficiency low threshold current 1.3 Î$\frac{1}{4}$ m InAs quantum dot lasers on on-axis (001) GaP/Si." Applied Physics Letters 111.12 (2017): 122107.

[83] P. M. Mooney "Defect identification using capacitance spectroscopy." Semiconductors and Semimetals. Vol. 51. Elsevier, 1999. 93-152.

[84] G. L. Miller, D. V. Lang, and L. C. Kimerling. "Capacitance transient spectroscopy." Annual Review of Materials Science 7.1 (1977): 377-448.

[85] D. V.Lang "Space-charge spectroscopy in semiconductors." Thermally Stimulated Relaxation in Solids. Springer, Berlin, Heidelberg, 1979. 93-133.

[86] D. K. Schroder, Semiconductor Material and Device Characterization, 3rd ed. (John Wiley & Sons, NY, 2005).

[87] P. M. Smowton & P. Blood(1997). "The differential efficiency of quantum-well lasers." IEEE Journal of Selected Topics in Quantum Electronics, 3(2), 491-498.

[88] M. Sugawara et al. "Effect of homogeneous broadening of optical gain on lasing spectra in self-assembled InGaAs/GaAs quantum dot lasers." Physical Review B 61.11 (2000): 7595.